Development of an Integrated Microfluidic Platform to Evaluate Radiotherapy Response of tumour cells

by

América Palacios Sánchez
B.Sc., Veracruz Institute of Technology, 2016

A Thesis Submitted in Partial Fulfillment of the
Requirements for the Degree of

MASTER OF SCIENCE

in the Department of Chemistry

Supervisory Committee

Development of an Integrated Microfluidic Platform to Evaluate Radiotherapy Response of tumour cells

by

América Palacios Sánchez
B.Sc., Veracruz Institute of Technology, 2016

Supervisory Committee

Dr. Alexandre G. Brolo, (Department of Chemistry)
Supervisor

Dr. Matthew Moffitt, (Department of Chemistry)
Departmental Member

Abstract

Supervisory Committee
Dr. Alexandre G. Brolo, (Department of Chemistry)
Supervisor
Dr. Matthew Moffitt, (Department of Chemistry)
Departmental Member

This thesis details the design, fabrication, and testing of two optofluidic platforms, a square fused silica capillary and a MgF_2-PDMS microfluidic chip to detect radiation-induced biochemical changes in cells during radiation treatment (radiotherapy).

The platforms integrate a near-infrared Raman system of 785 nm excitation and a fiber-based optical trap at 1064 nm in a dual-beam configuration for the manipulation and subsequent examination of single polystyrene beads (5μm) and two breast carcinoma cell lines, MCF-7, and MDA-MB-23 (20-30 μm).

Particular attention was paid to the role of MgF_2 as a novel substrate for microfluidic fabrication and the device background contributions that could hinder spectral contributions from the samples.

Successful optical trapping within the platforms was performed, which allowed the sample immobilization for the entire Raman acquisition time (10-30 s) via an orthogonally positioned objective for the excitation and collection of Raman signal.

Data collected in the MgF_2-PDMS microchip yielded high-quality spectra with no presence of PDMS characteristic Raman peaks in the spectral region of 450-1800 cm^{-1}.

Table of Contents

List of Tables

List of Figures

Acknowledgement

I want to thank everyone that contributed to a greater or lesser extent to the development of this thesis.

I am very grateful to my supervisor Dr. Alexandre Brolo and his endless patience, supportive words, and guidance. Thank you for the opportunity to be part of your research group and allow me to further my studies.

Thank you to all the members of Brolo's group. You all made my time at grad school an unforgettable experience full of fun moments and personal growth.

Thank you to the University of Victoria, CAMTEC, and all their staff for allowing me to use their installations, training me to use the equipment, and sharing their resources.

Thank you to the Department of Chemistry and its members for sharing valuable knowledge that helped me carry out my research.

A special shout out to Dr. Karolina Papera for helping me with microfluidics and cell culture; I learned a lot from you. Thank you to Dr. Stanislav Konorov for transmitting your knowledge about lasers and helping me whenever my setup misbehaved. To Dr. Samantha Van nest and Dr. Phiranuphon Meksiarun for sharing your Raman knowledge and insights on the project. To Monica Reimer for all the emotional support, and I cannot forget to thank Chris Secord, Machine Shop Supervisor.

Lastly, this would not have been possible without the unlimited support of my family through the years and the selfless support of my dear friends.

Dedication

I dedicate this thesis to myself. Thank you for don’t giving up!

1. Introduction

1.1. Current Radiotherapy approach and evolution

A critical challenge in radiation oncology is the administration of effective and significant doses of ionization radiation to cancer patients while minimizing toxicity effects and damage on healthy tissue. Although important successes have been achieved in radiotherapy (RT) development, this particular aspect is not yet solved in its entirety.[1]

Radiotherapy refers to the use of radiation as a therapeutic approach for cancer treatment.[2] This approach can be applied as a primary treatment or combined with other methods such as chemotherapy or surgery, either before (neoadjuvant) or after (adjuvant) the primary treatment.[3] About half of all cancer patients worldwide currently undergo radiotherapy as part of their treatment.[4,5] The magnitude of this number should be proportional to the efforts to develop methods that allow us to understand the effects and the mechanisms with which radiation acts in the control of cancer and should become a priority for the successful recovery of patients.

RT follows the discovery of X-rays by Wilhelm Röntgen in 1895.[6,7] Several novel medical and non medical applications for X-rays emerged and anything that could be photographed suddenly became subject to the "new ray".[8,9] Although the mechanism by which X-rays seemed to affect tumours was not understood, the immediate remission in symptoms and even the temporal or permanent improvement of patients with cancer, lupus, or tuberculosis proved the therapeutic properties of X-rays.[10]

Notorious side effects from the use of excessive radiation became apparent soon after, including post-diagnostic redness, weakness, hair loss, reproductive problems, leukemia,

erythemas that evolve into severe radiation burns leading to amputations and the death of several patients.[11]

The enigmatic response of non-cancerous tissue to radiation became of high interest for the scientific guild, which promoted early studies regarding the influence of dose rate and treatment length.[8,12] However, even fractionating the radiation dose over a number of days failed to eliminate the risk of normal tissue toxicity. The term therapeutic ratio is used to this day, to imply the acceptance of a certain degree of toxicity and damage to healthy tissue, representing the balance between tumour control and healthy tissue injury considered during treatment design.

Throughout the first four decades of the 20th century, several machines for diagnostic imaging and radiation therapy using X-rays were steadily improved in Europe and later in North America. The radiation that was initially produced through Crooke tubes, adapted on static generators and equipment used by the electrotherapists of the time evolved to be able to control the quality and quantity (dose) of radiation independently, obtaining significant improvements in ray stability and performance.[13]

Although methods were developed to keep the skin dose under tolerance limits, such as using multiple beams, the high dose problem remained an overriding concern in this period due to the beam producing a significant amount of scattered radiation derived from Compton scattering. A high proportion of the dose was still absorbed in the surface layer of healthy tissue, rather than being delivered to the tumour, causing both severe acute reactions and late skin damage as well as dose attenuation in bone, resulting in inhomogeneous dose distribution in soft tissue and significant bone-fracture risk.[14]

Finally, in 1948 the electron linear accelerator (LINAC) was developed by D.W. Fry.[15]

A LINAC is a machine that accelerates charged particles in a straight line down an evacuated tube of 1–2 meters in length, by a steady electric field or through a radio-frequency electric field. The first LINAC operated at 8 MV, achieved by decreasing X-ray leakage using collimators to shape irradiation beams for accurate delivery and lead shields for the protection of adjacent organs. Today, LINAC is the most widely used treatment device in cancer therapy and offers a reduced dose at the skin surface, a maximal dose to a relatively broad tissue thickness, and a rapid fall of dose at a depth corresponding to the electron energy.[16]

More recent advances in RT occurred hand-in-hand with computer technology development by incorporating imaging tools for treatment guidance, which improved the screening and detection of previously overlooked tumours; notable examples are the development of 3D conformal radiation therapy (3D-CRT), intensity-modulated radiation therapy (IMRT), Volumetric Modulated Arc Therapy (VMAT). Advances in 3-dimensional imaging enabled the delivery of therapy shaped to the contours of the tumour by the use of multiple radiation beams delivered from different directions, increasing the conformity of the high dose region to the target volume even in the case of complex geometry or invagination[17], to obtain even higher control of dose distribution by adjusting the delivery and decreasing the radiation reaching normal tissue while overcoming errors resulting from daily organ movement.[18]

Advances in the imaging field have allowed a higher degree of complexity into RT systems that influence the outcome of the treatment. The integration of optical elements provide the ability to control elements such as beam modifiers, nominal energy, field size, physical dose, dose rate, and more detailed physical measurements, including

comprehensive characterization of beam quality by microdosimetric spectrum and fragmentation spectra.[19]

The advances mentioned above in RT, although significant, have been mainly achieved thanks to improvements related to dose management technology and imaging tools. However, even with these developments, RT is still limited in efficacy due to toxicity factors to healthy tissue.[20] These factors span in levels of detriment from non-lethal endpoints, such as skin erythema and cognitive dysfunction, to potentially morbidity.

In consequence, new approaches to cancer treatment have emerged, including chemical modifiers or radiosensitizers, which are substances able to increase the tumour sensitivity without affecting normal tissue;[21,22] target agents, focusing on the molecules or antibodies that inhibit cellular pathways;[23–25] hormone therapies, to immunotherapies that promote the body's immune cells to fight cancer through our knowledge in cellular checkpoints.[26,27]

Our knowledge about the cellular mechanism of cancer and the individual molecule signaling that operates within the cell expanded in the last decades, but biomedical research is still in active development; enriching our understanding of the role that radiation plays in leading cancer cells towards death paths.[28]

1.2. Radiosensitivity

In RT, radiosensitivity is the relative susceptibility of a cell, tissue, or organ to suffer damage due to exposure to ionization radiation.[29] Identifying this property has helped to characterize the different degrees of damage that a cancer cell can undergo compared to a healthy cell and provides important insights in the prediction of treatment outcomes.

The notion of radiosensitivity originated as early as 1906 with the studies of two French scientists, Jean Alban Bergonié and Louis Tribondeau, which led to the development of an

important law in medical physics known as the "law of Bergonié and Tribondeau".[30–32] Their studies showed that different degrees of sensitivity were manifested depending on the extent of proliferation in the same biological system. Therefore, they concluded that cells were more affected by X-ray radiation if they possessed three properties: a high division rate, an extended karyokinetic fate, and an undifferentiated phenotype.[33] Although now obsolete, this law is considered a founding law in radiation oncology and paved the way for several radiobiology rules discovered years later.

Furthermore, Bergonié summarized the state of radiation oncology at the time, "they [*sic*] are two error types that may affect the medical application of X-rays: (1) the uncertainties in the assessment of radiation dose, and (2) the differences in the sensitivity of the patients".[33]

Rod Withers, in 1975 described factors that can contribute to the likelihood of local tumour control after fractionated radiotherapy, the so-called four Rs of radiotherapy.[34] These factors are the recovery from damage, cell-cycle redistribution, cellular repopulation, and tumour re-oxygenation, with a later addition of intrinsic cellular radiosensitivity as a fifth 'R' to account for the radiation tolerance of different tissues.[35]

Identification of prognostic (a “clinical or biologic characteristic that is objectively measurable and that provides information on the likely outcome of the cancer disease in an untreated individual” [36]) and predictive (a “clinical or biologic characteristic that provides information on the likely benefit from treatment (either in terms of tumor shrinkage or survival” [36]) factors remain an important aspect in the treatment decision-making process in breast cancer. Besides the five Rs, factors such as age, tumour size, lymph node status, histology, grade, margin status, and integration with clinical records are considered for

dose management. Imaging techniques such as magnetic resonance imaging (MRI) are used as a prognostic tool for determining the tumour stage and have been shown useful to alter the surgical options in up to one-third of breast cancer patients who undergo it.[37] However, there is no evidence that the use of MRI over conventional mammography produces a difference in clinical outcomes regarding any local failure, overall survival, freedom from distant metastases, or contralateral breast cancer.[38]

Pathological factors as predictive tools include, for instance, estrogen and progesterone receptor status and quantification, HER2 protein overexpression, and axillary nodal status, which remain the top pathologic factor that drives adjuvant treatment choices to accompany breast surgery and radiotherapy.[39]

Clinical intuition of a multidisciplinary team is another factor of current importance that still plays a fundamental role in treatment outcomes, especially for types of cancer that do not present biological markers to assess radiosensitivity, as in the case of head and neck cancer. Nonetheless, considering these factors, identically staged tumours under the same prescribed treatment can still show different outcomes.[40]

Identifying relevant molecular probes is another approach that attained further advances in the development to predict methods for the response mechanism of tumours and healthy tissues to radiation. Early assays for the radiation response of tumours are fundamental for the therapy's success as there is significant variation among patients in the levels of toxicity following radiation, limiting the maximum doses that can be safely delivered.[41] In addition, there is no recognized marker for assessing radio-response during the course of therapy. Therefore, there is a high interest in developing a test to measure the individual radiosensitivity of the patient before and during irradiation to increase the effectiveness of

the treatment, which needs to consider that radiosensitivity not only varies among cell origin but also varies among patients.

Radiosensitivity is an inherited genetic trait, and recent progress in genotyping raises the possibility of genome studies to characterize genetic profiles that predict patient response to radiotherapy.[29] The overwhelming cases of overtreatment and the current inability to address this particular problem are the motivation behind the search for personalized radiation treatment.

1.3. Previous Research on the Application of Raman Spectroscopy to Follow Radiotherapy

During the last decade, studies on the application of Raman spectroscopy for the understanding of radiation-induced tumour responses have been demonstrated by our group.[42–47] The study corresponds to the identification and analysis of signaling pathways in cancer cells originating from radiation exposure and their correlation to radiation sensitivity and the manipulation of these pathways to alter the tumour response to radiation.

The radiation work conducted at the University of Victoria represents the first application of RS to study the radiation response signatures of tumours irradiated *in-vivo* that may serve as potential biomarkers for radioresistance in human tumour cells.[44] The experiments consisted of the exposure of cell populations to radiation followed by Raman scattering examination and the statistical spectral analysis to identify intrinsic spectral variations. Among the research highlights was the use of MgF_2 as a clear window for Raman examination and the detection of intracellular glycogen accumulation by RS.[43,46]

In the study three different cell lines, MCF-7 (breast), H460 (lung), and LNCaP (prostate)s were exposed to typical clinical radiation doses (2-10 Gy). Cell monolayers were exposed to single doses of X-ray radiation using a linear accelerator at a dose rate of 6 Gy/min at isocenter and the colony of cells derived from the irradiated cells was analyzed by Raman scattering at a 785 nm excitation light on the days following irradiation (days 1 to 3). The cells were harvested, washed with phosphate buffer saline to remove any media, and then re-suspended in phosphate buffer saline (PBS) plus 10% fetal bovine serum (FBS). The suspension was centrifuged to form a pellet to be spread onto a MgF_2 disk. After waiting approximately 5 minutes to allow the sample to air dry, Raman data collection was performed.

Lastly, a principal component analysis (PCA) was implemented to evaluate the obtained Raman spectra. PCA is a statistical technique that uses multivariant analysis to discriminate between data sets, allowing independent sources of variability to be identified. The variations between the spectra are known as principal components. The differences in these spectra were statistically quantified by examining the spectral components with maximum variation compared to the original spectra and separating them in data sets. This technique helped to elucidate the components related to specific radiation-induced biochemical changes from inherent variability between cell cycle progression and incubation times.[47]

The glycogen increase represents a radiation-induced biochemical response with potential use as a therapeutic target. The cell lines MCF-7 and H460 are inherently more sensitive to radiation, corresponding to the highest glycogen accumulation. The likely explanation behind the triggering of glycogen accumulation was related to the expression of different kinases; the inactivation of glycogen synthase kinase 3 beta (GSK-3β) and the

activation of AMP-protein kinase (AMPKα). Both of them are in charge of regulating glycogen production, which is sensitive to ionization radiation effects[48]. Glycogen plays a role in the cytoplasm as energy reserve, reflecting the efforts of the cell to survive and repair itself after radiation damage. In addition to glycogen accumulation, the results showed variations in spectral features related to the expression of proteins, lipids and nucleic acids.[44,45,47]

The studies were conducted on the combined administration of molecular target drugs such as metformin, a commonly used medication for the treatment of diabetes and known radiosensitizer, and the delivery of radiation.[46,48] The Raman data obtained following the irradiation of cancer cells while in the presence of metformin showed a significant reduction in glycogen accumulation in the two radioresistant cell lines (MCF-7 and H460), showing no changes in the analyzed prostatic cells (LNCaP). The reduced presence of glycogen can be partly explained by the phosphorylation GSK-3β following radiation which interferes with the capacity of glycogen synthase to accumulate and the activation of AMPKα intracellular glycogen previously associated with radiosensitivity.[49,50] These results demonstrate that this RS approach can detect the response to radiation inherent to specific cells and tissues. However, it can also be used to determine the effects on radiosensitivity produced by external factors. In this case, the administration of Metformin simultaneously with radiotherapy

Another novel approach was the use the RS protocol and partial least squares discriminant analysis (PLSDA) to detect subtle differences in the relative intensity of spectral features among breast cell lines.[47,51,52] The approach revealed inherent differences in biomolecular compositions between tumour cell lines and discriminated them from the

healthy surrounding tissue.[51] The PCA components suggested that glycogen is the main contribution of MCF-7 cell response to radiation as the 69.1% of variance and showed a time-dependent positive median score shift towards higher glycogen content post-irradiation. In addition, other less prominent features were observed from DNA and amide I.

Although in early stages, these studies support the possibility of using a spectroscopy approach as a predictive tool for radiation sensitivity. A tool for both, the planning of a radiation treatment protocol, based on the radiosensitivity of the patient's specific tumour; and the monitoring of treatment response during early stages of radio treatment, which in turn would allow to assess and adjust radiation doses according to the observed tumour reaction to the treatment.

1.4. Thesis Scope

The results described in Section 1.3 represent the breakthroughs obtained by our group in detecting biochemical induced radiation effects on different cell lines using Raman spectroscopy to correlate specific Raman signatures with individual radiosensitivity.

The most promising application of this RS approach is a tool for assessing biochemical signatures from a patient's sample, allowing treatment modification as required based on the patient's specific response to radiation.

Although the method seems promising, the Raman approach mentioned above cannot be employed for real-time monitoring of tumour response due to extensive *and lengthy* data acquisition relative to the treatment timeline. The focus must be placed on automating the spectral acquisition protocols for the potential application in the clinical environment. Also, steps to alleviate drawbacks in the data acquisition process must be taken, such as the

placement of living cancer cells on a MgF_2 disk which does not represent an actual cell monolayer and which handling could potentially change the chemical microenvironment of the living cell from the bulk solution and may yield unknown effects on the cells.

Benchtop equipment for real-time quantitative monitoring of cellular samples has been commercialized for high-throughput screening applications.[53] Nevertheless, most research results will never be applied in clinical practice, due to a lack of translational research.[54] In order to narrow the ¨Bench – Bedside¨ gap,[55] it is necessary to look for promising technologies that allow the integration of screening and bio-sensing techniques that provide accessible and easy operation. To move forward with this technology to monitor radiation effects, high-quality translational research needs to be implemented.

This thesis proposes the fabrication and implementation of a Raman-microfluidic device suitable for radiation oncology combined with optical trapping (OT). The development of a microfluidic platform with an integrated system-level design would address critical issues in the Raman spectra methodology. A system capable of performing rapid measurements of a cell sample while achieving experimental results similar to those presented by Harder and Matthews[43,46] could help to observe radiation responses produced in the early stages of the treatment.

A Raman-microfluidic system for assessing the response to RT with these characteristics has not yet been implemented. However, integrated optofluidic platforms combining Raman and laser tweezers have already been proposed.[56–58] The following literature review shows the mature development of microfluidic technology in research laboratories and provides examples of integrated microchip platforms that support this work's suggested approach as an excellent candidate for future clinical implementation.

The manipulation of individual cells is a widely pursued subject in microfluidics research. In the last decade, the push for thorough single-cell analysis has resulted in the development of new highly parallel fluidic devices and integrated detectors with the ability to overcome many of the problems from traditional data acquisition techniques.[59] Therefore, roughly 1000 papers are published regarding cells in microfluidic devices every year.[60]

The potential to develop and implement a Lab-on-chip (LOC) platform as a decision tool comes from the inherent advantages of microfluidic technologies (Section 2.1.1). Microfluidics allows the production of highly reproducible devices suitable for high throughput applications. Thus, reducing data variability associated with laboratory conditions, instruments used to conduct the experiment, or personnel differences, simplifying sample preparation, and increasing the automation of systems.

Some microfluidic systems implemented Raman spectroscopy as a tool for spectra acquisition and single or double beam optical tweezers as part of interrogation points. There are reports on integrated optofluidic Raman-activated cell sorting (RACS) platforms that require no prior sample manipulation or staining with fluorescent markers for cell classification by vibrational spectroscopic analysis, as well as laser tweezers Raman spectroscopy (LTRS) systems that combine multichannel microfluidic devices and laser tweezers for delivery, label-free identification, and sorting of individual cells.[61] These configurations are a powerful tool for identifying micrometer-sized particles in an aqueous environment.[62]

Optical traps enable the capture of small particles in solution using a laser beam. OT combined with microfluidic environments enable biomechanical and morphological

research of single living cells and provide a high degree of automation for cell classification. The utilization of optical traps may ease those obstacles for single cell research during high sensitivity studies. Therefore, several examples of microfluidic-based flow cytometers exist in the literature.

Xie et al.[63] reported in 2002, the first study of Raman tweezers to examine living cells. The system was used to study red blood cells (RBCs) in solution and differentiate between living and dead yeast cells. A low-power Ti:Sapphire diode laser operating at 785 nm was used to reduce photochemical and thermal cell degradation and reduce fluorescence spectra interference.

Living RBCs diluted to 1:10000 with 0.9% saline solution were placed on a cover plate and held trapped ~15 μm above the bottom plate. The system implemented a power-switching technique for which the diode laser was programmed to operate at low power 2.0 mW during trapping and switch to high-power 20 mW when a Raman measurement was taken. After background subtraction, several bands were observed and compared against assigned and published characteristic bands.

Another valid configuration for the entrapment of larger cells is the use of separate beams for Raman interrogation and trapping. An example of this is the work of Jess et al. 2016,[64] where they used a dual-beam fiber trap to hold and maneuver human keratinocyte (PHK) skin cells (30 μm in diameter) combined with an orthogonally placed objective to record localized Raman spectra. Due to its divergent light fields, the dual-beam trap offers the ability to hold and move large cellular objects with reduced possibilities of photodamage.

In order to trap the cells, a 1070 nm fiber laser coupled to two single-mode fibers via a half wave plate and a polarizing beam splitter cube with a power of 40 mW coming from

each fiber (irradiance of $4.6x10^9$ W/m^2) with a fiber face separation of 85 μm was used. At the same time, a 785 nm, 20 mW laser beam for Raman excitation (irradiance of $2.5x10^{10}$) passed through an 100x NA=1.25 oil immersion objective to the sample in an inverted configuration.

The trap successfully permitted the spatial manipulation of the cell by adjusting the laser power or adjusting the position of the fibers relative to the Raman excitation laser beam via mechanical movement of the sample stage. A high-power objective was selected to achieve a tightly focused beam coupled to a 100-micron diameter pinhole in the image plane, corresponding to a 1-micron aperture in the sample plane. Spectra from membrane, cytoplasm, and the nucleus within the PHK cell was integrated for two minutes, summed together, and smoothed using the adjacent averaging method.

Previous experiments to demonstrate the system's ability to measure the depth of the particle at each point were performed using polystyrene beads. The traps consisted of multimode fibers, used to trap a 100-micron bead requiring 800 mW (output irradiance of 5.2x108 W/m^2) from each fiber with a fiber face separation of 240 μm; and single-mode fibers, with a fiber face separation of 175 μm, used to trap a 50-micron bead requiring 40 mW (output irradiance of $4.6x10^9$ W/m^2) from each fiber. The Raman excitation laser was set to 30 mW (irradiance of $4x10^{10}$ W/m^2) and focused onto the sample with a Nikon x50 N.A.=0.9 oil immersion objective, and the Raman signal was then integrated for two seconds. The intensity of the 1000 cm^{-1} benzene ring breathing mode present in the polymer was monitored during scanning.

Finally, a rudimentary microfluidic system based on a glass capillary was developed to combine the dual-beam trap with a flow system. The setup was used to hold and acquire

Raman spectra from individual polystyrene beads and cells from a sample of HL60 human promyelocytic leukemia cells. The system consisted of two single-mode fibers placed opposing each other, against the outside wall of the 80 μm inner diameter capillary tube, resulting in a fiber face separation of 160 μm with an orthogonally placed objective to excite and then record Raman spectra. The capillary ends were placed in two reservoirs resulting in a flow driven by capillary action.

The use of a square glass capillary offers optical properties, such as good transparency, precise calculation of the propagation of the laser beam from the fiber ends to the location of the particles in the center of the capillary. Polystyrene beads (10 **μ**m) at a volume flow rate of 1.2μL/s were analyzed with a fiber power of 80 mW (irradiance of 4.6×10^9 W/m^2). A 50 mW Raman examination beam (irradiance of 6.3×10^{10} W/m^2) was then introduced from below using a Nikon 50x NA=0.9 oil immersion with an excitation time of 5 seconds.

Additionally, HL60 cells, a human promyelocytic leukemia cell line at a volume flow rate of 40 pl/s and a fiber power of 80 mW (irradiance of 4.6×10^9 W/m^2) was also analyzed. Despite the higher laser power from the fiber trap, and an acquisition time of 60 seconds the cells did not get damaged during the trapping.

The dual-beam fiber laser trap combined with a capillary-based microfluidic system configuration presented by Jess et al. has been used by other researchers, such as Lincoln et al.[65], to serially trap and deform MCF-10 mammary epithelial cells and compare the distribution of deformability found within a normal cell line to that of a cancerous one by the measurement of their time-dependent response to constant stress. This setup explores the possibility of diagnosing cancer and of characterizing the differentiation of cells by using optical deformability as an inherent cell marker.

The microfluidic optical stretcher (MOS) based structure is a cross-section pattern that quarters a SU-8 photoresist rectangle (35 μm thickness) built onto a glass microscope slide. The gaps formed from the cross-sectional cuts served as guides to align opposing optical fibers and position them perpendicular relative to the capillary. The square capillary (160 μm OD; 80 μm ID) sits inside a 180 μm gap and extends well off the glass slide on both sides connecting to a flow tubing. The optical fibers (125 μm diameter) are aligned by being placed on the 110 μm gap on either side of the capillary and connected to an Ytterbium fiber laser (λ=1,064 nm) that splits evenly into two single-mode optical fibers (HI 1060, Corning) via a 1x2 fiber coupler (Gould Fiber Optics) with divergent Gaussian beam. A thin piece of Poly (dimethyl siloxane) or PDMS with a 1.5 mm hole in the middle is placed over the setup for holding the capillary and the fibers in place. The hole that encompasses the trap region is filled with index matching gel to reduce reflection and distortion of the laser beams. Finally, a coverslip is placed and gently pressed over the PDMS piece to seal de system.

Cells were introduced into the capillary, trapped (80 mW per fiber), and subsequently deformed for 5s (800 mW per fiber) at a measuring rate of 50–100 cells/h. Due to the flat glass walls, the capillary avoids optical distortion, and the ability to analyze the deformation of cells within 5 nm resolution.

A capillary setup provides flexibility to an optofluidic system. This type of design allows control over the size and position of the trap relative to the flow channel. It accommodates many sizes and combinations of cells, capillary material, and optical fiber mode-field diameter, which is a desirable feature for manufacturing specialized microfluidic prototypes.

Another optically transparent material have been used in similar configurations by Dochow et al.[66], whose research likewise combines Raman spectroscopy to acquire spectra of single cells in microfluidic channels. The study described two devices, a quartz capillary setup and a borofloat 33 glass microchip coupled to optical fibers to collect Raman spectra of single cells.

The capillary setup was made up of quartz with dimensions of 330x330 μm OD and 50x50 ID placed on a metal block that doubles as a capillary holder and fiber guide. Raman spectra of five cell types were recorded: erythrocytes, leukocytes, acute myeloid leukemia cells (OCI-AML3), and breast tumour cells (BT-20 and MCF-7). LDA classification models were used to identify the cell and differentiate healthy and cancer cells with accuracies comparable to Raman spectra from fixed cells in a Petri dish.

Although the capillary setup was combined with two 1070 nm single-mode fiber lasers, the collected spectra result from studying individual cells trapped by the Raman excitation laser operating at 785 nm, which was enough to trap them with a tweezing power of 100 mW for 10s acquisition time. The setup provides valuable engineering recommendations for the implementation of optical traps for identifying and classifying single cells from body fluids such as saliva, urine, and blood.

The second setup introduced a microfluidic glass chip that accommodates different functionalities. A flow-focusing unit for thinning out the cell suspension before the trapping area formed by four single-mode optical fibers with facilities for single-cell Raman spectroscopy, and a Y junction for flow switching and cell sorting between two outlets depending on the Raman-based classification. Functions that are not possible to incorporate in a capillary configuration.

The microfluidic device, with dimensions of 16 x 25 mm, consisted of nine fluid ports and four fiber ports. The glass substrate allowed the channel formation by isotropic wet etching. The trapping structure forms a circular cavity with a height of 60 µm and a diameter of 190 µm, centered between two fiber channels. The distance between the fibers is 210 µm, while the capillary setup was of 330 µm distance between fibers.

On the other hand, the Raman spectra could only be obtained at 514 nm excitation (Argon-ion laser for excitation and a 60x, NA=1.0, water immersion objective) to decrease glass background signals. However, this excitation wavelength induces degradation of living cells at the required high intensities, even at short exposure times.

These two devices led to the development of a microfluidic chip using quartz wafers as a substrate. The use of quartz allowed the implementation of a laser operating at 785 nm for Raman excitation, similarly to the experiment used for the quartz capillary from the previous manuscript. The quartz chip included all the same functionalities as the glass chip and was used for Raman-activated cell sorting studies of tumour cells (BT-20, MCF-7, and leukemia cells OCI-AML3) and leucocytes. The space between the objective and the chip was filled with water to reduce the refractive index gradient, combined with an 60x, NA 1.0 water immersion objective. Single cells in suspension were injected at a flow rate of 1 nL/s altogether, 405 cells were manually trapped by the 1,070 nm trapping lasers, and their spectra were collected at an exposure time of 10 s each.

Compared to the Raman results obtained from the glass microfluidic chip at 514 nm excitation, the overall cell identification accuracy improved from 94.9 to 98% due to the higher signal-to-noise ratio of the acquired spectra. In addition, a new spectral data processing approach involved the additional acquisition of spectra without cells as

background spectra. These spectra improved background correction offering the advantage of assigning spectra with low signal to the background group instead of an incorrect cell group like in the previous models.

A prior attempt to solve the implementation problems of the RS approach produced by our research group and create a microfluidic device to identify radiation-induced responses in single cells was performed by Samantha Van Nest in 2018, performing cell spectra characterization within different microfluidic systems with simple microchannels fabricated in either MgF_2 or Parafilm®.[67]

Cell spectra were obtained within a laser-cut channel produced in a 170 µm thick MgF_2 window, an optical window manufactured from crystalline Magnesium Fluoride. A Ti:Sapphire specialized laser was used to create the 15 mm long channel with dimensions 207 µm wide and 75 µm deep. The data obtained from this microchannel contained all the spectral features relevant for our cell studies with no impeding substrate-based contamination. However, there are critical issues with the manufacturing of this system; in particular, creating a 15 mm long channel required a lengthy process of 10 hours that yielded an irregular channel geometry. Furthermore, sealing procedures were not implemented in this design as there is currently no effective way to fuse two pieces of MgF_2 directly. More properties of MgF_2 can be found in Table 3-1. Therefore, despite the appealing spectral features of the MgF_2 system, the manufacturing of a chip with these properties represents extensive challenges regarding chip production.

In the same work, a Parafilm®-MgF_2 microfluidic system found to produce promising cell Raman spectra. It did not suffer from important levels of background contamination levels and presented key cell spectral features. This system consists of a Parafilm piece

with a channel-shape cut of 79 µm wide and 200 µm deep, placed between two 170 µm thick optical grade MgF_2 windows sealed using heat. The channel dimensions were limited by the width of the knife blade used and the thickness of the Parafilm. The sealing between the MgF_2 window and the surface of the Parafilm showed unclear results on whether it would be strong enough to resist high pressures derived from the liquid sample flow. In addition, parafilm is a single-use material, which is impossible to clean thoroughly without affecting the material's structural integrity.

Even though the parafilm-MgF_2 microfluidic chip represents an unsuitable choice for radiobiological applications, the studies revealed that using Parafilm as the substrate for the microchip walls and not as the chip "window" diminishes the contribution of the polymer.

The substitution of Parafilm by PDMS is a fabrication choice explored in this thesis. Most microfluidic systems use PDMS as a substrate; unfortunately, PDMS yields strong Raman peaks that contaminate critical regions of interest for single-cell studies and particularly for this radiobiological work.[68] The use of PDMS as the middle layer of the microchip offers the possibility to create channels using traditional microfluidic fabrication techniques while avoiding contribution from the substrate.

A microfluidic chip pairing PDMS and MgF_2 follows compatibility requirements.[69,70] Ideally, the proposed microfluidic device should serve as a tool for scanning cancer cells grown *in vitro, and* the materials must promote a controlled microenvironment to analyze biological samples. Toxicity or stress produced on the cells can give rise to unwanted spectral Raman contributions that are hard to distinguish from the ones produced by ionizing radiation.

MgF_2 possesses superior optical properties for Raman spectroscopy (Section 3.2). The benefit of MgF_2 as a substrate follows the established protocols of our group's RS approach that uses a MgF_2 disk for spreading the biological samples before Raman data collection. Using this substrate to create a transparent base and top device provides a clear optical window for RS examination and facilitates data comparison with previous research to validate the chip's capacity to obtain information-rich spectra. However, the use of MgF_2 represents an engineering challenge.

The use of MgF_2 as a microfluidics substrate is not a standard. The material is highly resistant to chemical etching and thermal shock and possesses a high laser damage threshold, making it resistant to the most common methods of microchannel fabrication (Figure 2.2). Also, its fragility stops it from being drilled for inlet/outlet creation, and its molecular structure makes it unable to become bonded by using Plasma treatment. Therefore, this research requires modifying traditional microfluidic fabrication methods to accommodate a polymer body and MgF_2 as the device window for our specific research purposes.

The decision to integrate optical traps comes from the spectra collected from the 2018 parafilm microfluidic device.[67] The spectra collected presented a degree of noise and variation throughout the channel and from one acquisition to the next that could be explained by the inconsistency of the channel dimensions, increasing the contribution of background spectra. Fixing the position within the channel in which cell spectra are collected could help to improve these inconsistencies. Therefore, the emphasis on integrating an entrapment system where a single cell is completely isolated from other cells and substrate surfaces; eliminating any unwanted background signals and ensuring that

information is collected only from the selected individual cell and maximizing signal collection.

1.5. Objectives

The general aim of this research project is to design and fabricate an optofluidic device for the radiobiological study of single cells by Raman spectroscopy. This system will integrate Raman spectroscopy equipment operating at 785 nm connected to an upright optical microscope and a compact laser diode at 1060nm to produce contra propagating optical traps inside a microfluidic platform. Optical traps are intended to immobilize a cell within the Raman laser focus to maximize the signal collection for the interrogation of Polystyrene beads (PS beads) and MCF-7 and MDA-MB-231 human breast cancer cell lines.

Many considerations underlie the construct of the microfluidic system. This thesis presents the design of two distinct microfluidic platforms: A fused silica capillary-based microfluidic device and a MgF_2 microfluidic device. To this end, this thesis investigates the spectral characteristics that each system can yield.

The first objective is to design and fabricate a capillary microfluidic system that integrates injection of single cells, trapping by laser fibers, and Raman spectroscopy examination.

The following can be defined as the specific objectives for this microfluidic design.

1. To design a microfluidic platform with a fused silica capillary as the central fluidic component.
2. To achieve biocompatibility with cancer cells through material selection

3. To design a holder that provides accurate and stable adjustment of the capillary, microfluidic connections, and the trapping laser fibers.
4. To design and test an optical trapping setup, including the search for adequate conditions of laser power for the trapping of PS beads and cancer cells inside the capillary system.

The second objective is to design and fabricate a microfluidic chip-based device.

The following can be defined as the specific objectives for this microfluidic design.

1. To design a microfluidic chip that incorporates a dual beam trapping region and facilitates Raman spectroscopy examination.
2. To employ MgF_2 as a novel substrate for the fabrication of the microfluidic device.
3. To achieve biocompatibility with cancer cells through material selection.
4. To modify the capillary holder for the integration of the microfluidic chip, microfluidic connections, and the trapping laser fibers.
5. To demonstrate the optical trapping withing the microchip
6. To obtain Raman spectra of PS beads and cancer cells inside the microchip

1.6. Thesis outline

The thesis contains the following chapters:

Chapter 1 provides a general introduction regarding the evolution of radiotherapy as cancer treatment, introduces the term radiosensitivity, and showcases our group's previous research milestones on a RS approach to study the effects of radiation on cancer cells to contextualize the motivation behind the current work. The chapter also reviews relevant

literature regarding the development of contemporary microfluidic systems, emphasizing technologies that comprise optical traps and Raman spectroscopy for cell analysis with application in the biomedical and chemical fields.

Chapter 2 delves into the fundamental concepts in microfabrication, emerging technological applications, as well as the benefits of the microfluidic environment compared to conventional models; also addresses the issues of Raman scattering, optofluidics platforms, and optical trapping, with important considerations and relevant examples from the literature of their application in cell studies.

Chapter 3 introduces the physical and chemical properties of the desired platforms. Addresses the engineering challenges and describes in detail the fabrication of a fused silica capillary platform and a new fabrication technique for a PDMS–MgF_2 microchip system and the material selection process for generating ultra-high SU-8 master molds using photolithography and PDMS replicas by soft lithography.

Chapter 4 introduces the materials and specific experimental methodologies used for the testing and characterization of the fabricated microfluidic devices in combination with optical traps for the manipulation of polystyrene beads and single cells.

Chapter 5 shows the results obtained after the procedures introduced in chapter 4 for the testing of the microfluidic platforms. The chapter also includes a discussion about the findings of the investigation.

Chapter 6 Concludes this thesis work with the final remarks regarding the overall performance of the microfluidic platforms and provides recommendations for future projects regarding the further development of a microfluidic platform for oncological research.

2. Background

2.1. Microfluidics

Microfluidics is the study of fluid mechanics at the microscale (10^{-6} to 10^{-15} L) and the technology that encompasses the manufacturing of microfluidic systems[71].

A microfluidic device is created by stacking independent layers comprised of etched or molded channels into a material. Subsequently, the channels are sealed by the layers above and below, bonding the chip together. This action allows the creation of inlets and outlets to inject a fluid sample that will flow in a constrained manner. The pathway geometry of the channels provides specific functionalities to the system enabling the controlled manipulation of the fluids.

Microfluidic manufacturing originates from the technological adaptation of processes introduced by the microelectronics industry and, since its origin, has developed ever-more-complicated configurations in continuously smaller devices. The original manufacturing method for microelectromechanical systems (MEMS) or semiconductors is photolithography on a silicon substrate. However, silicon and not optically transparent and the technique requires expensive specialized facilities;[72] therefore, a variety of new materials have replaced it to increase chemical compatibility, reduce costs, facilitate structural reconfiguration, and incorporate external elements, such as active (e.g., sensors, heaters) and passive (e.g., filters, physical traps) components that add new functionalities to the system.

There are many methods to fabricate the necessary channels and features that meet the required dimensions to work at the microscale, including photolithography, chemical or

dry etching, and laser cutting.[73] Current microfluidic devices are commonly fabricated from polydimethylsiloxane (PDMS) using multilayer soft lithography, a well-documented technique introduced in 2000 by Whitesides.[74] In the simplest sense, soft lithography refers to replica molding using silicon-photoresist molds created using standard photolithography techniques. In order to form a closed channel, the polymer is poured into a mold, cured, and peeled, resulting in a polymeric casted stamp that can be bonded with a glass slide. SU-8 is a common negative photoresist used in mold fabrication due to its high resolution, mold durability, and capacity for high aspect ratios. A schematic of the lithography process is shown in Figure 2.1

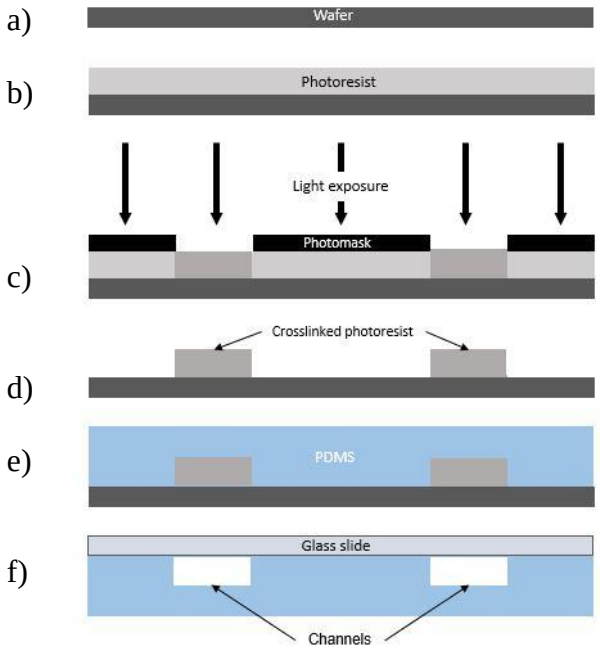

Figure 2.1 Typical Photolithographic Process: (a) Silicon wafer, (b) Spin coating allows photoresist (e.g., SU-8) deposition on Silicon wafer, (c) a photomask blocks UV Exposure in some areas of the photoresist; the exposed areas become crosslinked. (d) The photoresist undergoes baking and developing; non exposed areas get removed (e) PDMS is pour onto the master mold and baked (f) Plasma bonding between PDMS cast and glass slide.

Polymer bonding refers to the encapsulation of the open channels and cavities on the polymer substrate using another polymer layer or film. The bonding method selection is inherently tied to the materials employed in the fabrication method and has a significant impact on the pressure that the device can withstand, which can significantly affect the performance. Poor bonding is also the source of many problems present in microfluidic devices, including air bubbles between layers that lead to leakage and the deformation of features in the microfluidic device, which can seriously degrade the device performance.

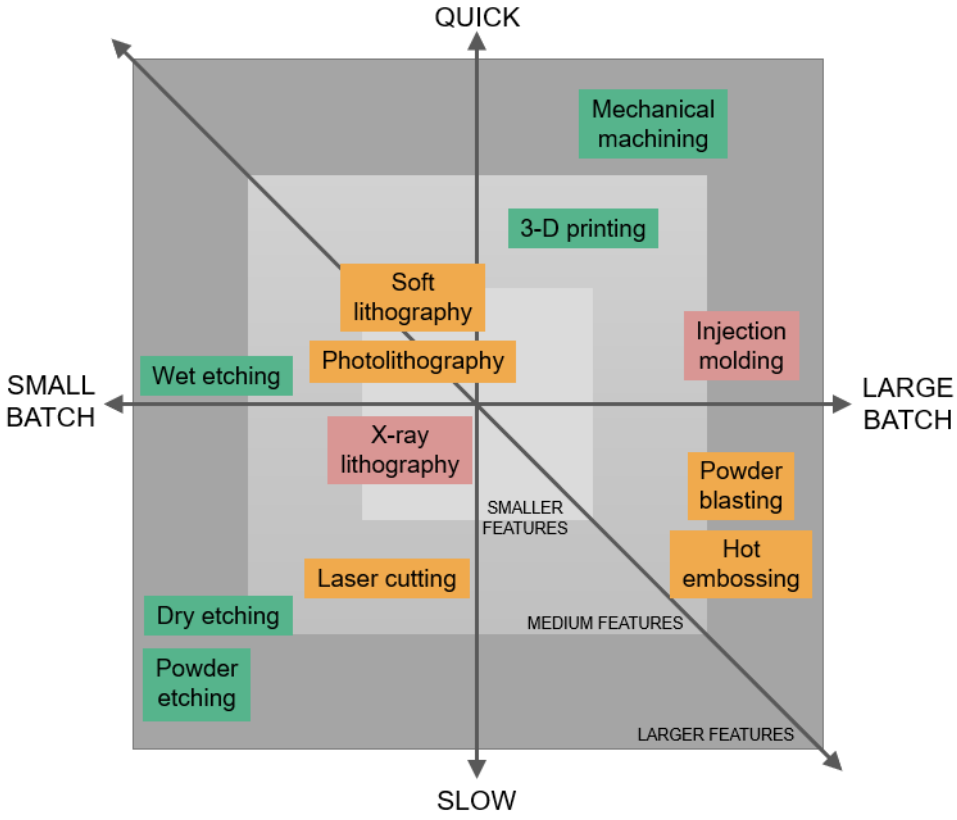

Figure 2.2 Overview and comparison of key fabrication techniques used in microfluidics. The Illustration showcases the relative merits of each technique regarding speed of fabrication of a single device (vertical scale), Adaptability for batch fabrication (horizontal scale), achievable feature dimensions (radial scale), and total production costs (Color scale). Color scale: green (low cost), orange (medium cost), red (high cost).[73,75–77]

Therefore, adequate optical transparency and strong bonding strength under elevated flow pressure are generally the requirements for window selection. The use of polymers (including acrylic and polycarbonate) and glass layers are common for many of the same reasons: optical clarity, low cost, and sample compatibility. While these are the three most common materials, an immense number of other substrates can be employed. Indeed, due to its compatibility with so many different forms of bonding (including simple adhesives), glass is the most compatible with the widest variety of materials, making the Glass-PDMS combination a standard in the fabrication of microfluidic devices.

Microfluidic devices can be made using a wide range of materials and fabrication methods. The chart in Figure 2.2 compares the general aspects to be considered before the development of a microfluidic platform.

2.1.1. Benefits and applications

Microfluidics allows the automation of labor-intensive experimental processes by performing many operations simultaneously, shortening experiment reaction times.

Table 2-1 displays several advantages and benefits of microsystem platforms, including less sample/reagent consumption, reduced contamination risk, less cost per analysis, reduction of repetitive operations, and elimination of the need for expensive laboratory equipment.[78]

Additionally, as we scale down, the behavior of physical laws changes. Properties such as inertia and gravity become irrelevant compared to surface tension and hydraulic resistance, which become more significant. The surface to volume ratio also increases during miniaturization; thus, the chemical interactions between the surface and solution phase are much faster because the diffusional distances decrease, which is of high

relevance to the study of reaction kinetics,[79] evaporation effects,[80] enzyme catalysis, and on-chip cell culture.[81]

Table 2-1 Summary of advantages of implementing microfluidic systems.[82]

Microfluidics Advantage	Description
Less sample and reagent consumption	Microfluidic devices typically require $10^2 – 10^3$ less sample volume than conventional assays.
Enhanced heat transfer	Higher surface area-to-volume ratio of microfluidic channels increases effective thermal dissipation.
Laminar flow	Low Reynolds number flows reduce sample dispersion.
Lower power consumption	Fewer components and enhanced thermal dissipation require less power input.
Parallelization	Several assays can be multiplexed or run in parallel on a single chip.
Portability	System integration and reduced power allows for assays to be conducted using portable, hand-held device.
Global cost reduction	Automation of labor-intensive experiments may reduce reagents and energy consumption, instruments, and labour
High surface area to volume ratio	Faster analyses and shorter reactions times

In microfluidics the Reynolds number in most devices is well below the turbulent limit. Reynolds number, Re, is a dimensionless quantity that describes the ratio of inertial to viscous forces in a fluid.

$$Re = \frac{\rho v L}{\mu} \quad 2.1$$

Where, Re is proportional to the characteristic velocity (v) and density (ρ) of the fluid and the length scale of the system (L), and it is inversely proportional to the fluid viscosity (μ), which means that viscous forces play a significant role dictating fluid flow characteristics and that inertial force effects dominate the flow behavior.

Reynolds help to predict flow patterns and understand the transition from a turbulent flow (high Re number) to a laminar flow (low Re number) in geometrically similar objects.

Due to the dependence on length scale, Reynolds number in microscale systems tends to be small and flows laminar.

A laminar flow regime allows for highly predictable fluid dynamics applied for diffusion,[83] gradient formation,[83,84] and focusing studies.[85]

Microfluidic devices are widely used in many scientific and industrial fields.[86] Some practical applications are the development of lab-on-a-chip (LOC) technology that enables the integration of a variety of processes and functionalities on a single microfluidic platform or the development of point-of-care (POC) technology, a sub-branch of LOC that focuses on the creation of miniaturized instruments that deal with the ever-increasing need for biomedical testing at or near the patient bed in a hospital.[87]

Microfluidic systems are beneficial for research topics such as diagnostics, high throughput screening, and sensing, sample preparation, genomics, polymerase chain reaction PCR, regenerative medicine, and flow cytometry.[88–90] Microfluidic technologies can serve as predictive models to understand biological behaviors further. Miniaturization allows working in conditions similar to real-life; adjusting parameters to mimic the physiological environment closely creates optimal conditions for local processes to take place. [91] It can be implemented to automate immunoassay operations, a bioanalytical technique widely used in clinical and pharmaceutical research to measure the presence and concentration of antigens in biological samples for disease detection, which conventionally involve time-consuming and labor-intensive steps such as incubation and washing. Micropumps can be integrated into a microfluidic device to sequentially pump samples and reagents to reaction chambers within the chip to precisely control the flow rate by addressing the reaction times of the different assay steps. Likewise, droplet-based

microfluidic devices have shown amplification efficiencies with no evaporation loss, reaching a total reaction time of half of the required for benchtop PCR, which shows potential for POC applications.[92]

2.1.2. Microfluidics and single cell studies

Single-cell analysis has gained considerable attention for biological assays and system biology in the past decade due to the increasing importance of studying highly heterogeneous cell populations, as well as a sampling of complex biofluids such as blood. The reductionist approach provided by integrated microfluidic systems allows the spatiotemporal analysis of single cells under well-defined environmental conditions.

Single-cell analysis is the measurement of signaling events within individual cells at the molecular level. The goal is to analyze and synthesize this information to better understand the cell population, which links to the behavior of tissues, organs, and eventually whole organisms. Bulk measurement can only reflect the average value, leading to a loss of valuable information about rare sub-populations (diseased cells or abnormal cells) present in the sample.

Furthermore, microfluidic systems offer several key advantages for studying single cells, including facile automation, parallelization, and reagent reduction with minimal dilution, resulting in high sensitivity assays.

In cancer research, microfluidics technology holds great promise for diagnosis, cell counting, and sorting[93] as a classification tool[94] and for the understanding of cancer biology.[95]

Microfluidic technology has emerged as a potential tool to create and manipulate the cellular microenvironment, leading to a greater insight into cellular physiology.

The technology has been applied for gaining knowledge about circulating tumour cells (CTCs) and the development of anti-metastatic drug therapies. Some examples are the development of fluidic platforms for the identification, capture, and screening of CTCs. Fan, X.[96] developed PDMS-based filters integrated into a microfiltration chip for CTCs isolating from whole blood samples, achieving >90% recovery of isolating lung cancer cells. Another device by Shaner, S.[97] isolates the CTCs using a specific antibody binding approach by the modification of the microchannels with an alginate hydrogel coating. Furthermore, label-free approaches that do not rely on antibodies or biological markers can also be incorporated into the system (Section 2.3.3). Both pieces of technology exemplify how engineering and material science can facilitate a better understanding of circulating cancer cells by introducing micro-features to produce specific functionalities.

Microfluidics can be used in combination with other complementary analysis methods to enable further characterization of a sample.

2.1.3. Combination with other techniques

The reductionist approach that prevails in various biomedical and chemical applications has promoted an accelerated rise in the manufacture of integrated microfluidic systems that use optical elements for studies at the single-cell level, which allows for the understanding of highly heterogeneous cell populations.

To meet the key requirements that bioanalysis instruments and point-of-care devices demand, the field of optofluidics was created which is the symbiotic integration of the

microfluidic environment with the photonics technology for the creation of highly sensible bioanalytical devices.[98]

Optofluidic devices can present a higher amount of capabilities, increased flexibility, and decreased space requirements than traditional flow cytometers that also integrate laser light sources and electronics for the analysis of cells, DNA, and other particles, in studies related to cell cycle, cell viability, immunophenotyping or sorting.[99] Nonetheless, relevant single cellular information can get lost in its conventional average-based process analysis.[100]

Cell handling has been integrated into microfluidic and LOC devices to manipulate and immobilize cells and various biological materials. On-Chip manipulation of micro-objects involves trapping, sorting, and separation, finding their applications in chemistry, biology, and colloidal science.

Many recent technological advancements rely on a force to manipulate trap, sort, isolate, and measure single cells from suspension. The forces that can be externally applied range from acoustics,[101] mechanical;[97,102] magnetic;[103] electric,[104] and optical forces.[105,106]

Optical trapping is a proven reliable tool for manipulating single cells with the ability to preserve cell integrity after performing detailed biomechanical characterizations. It is possible to hold and interrogate a cell away from any surface without damage reducing extraneous signals from the local environment.[107]

Different technologies can be coupled to microfluidics to aid with the characterization of species in the fluid, including optical microscopes, excitation lasers, optical filtering, manipulation devices, and spectrometers.[108] Some examples of systems and spectroscopic techniques used in microfluidic systems include atomic force microscopy (AFM), which uses scanning probes for nanometre-scale chemical resolution analysis to reveal

complementary mechanical information,[109] ultraviolet-visible absorption (UV-Vis),[110,111] Fourier-transform infrared spectroscopy (FTIR),[112–114] fluorescence spectroscopy,[115] and Raman spectroscopy.[116] RS, showing highly relevant results for the study of cancer cells in suspension, including stationary cell measurements, trapping, and sorting.[108,117]

2.2. Optical trapping

Optical trapping (OT) is a technique that exploits the physical properties of light, utilizing the momentum of the photons from a highly focused laser beam to exert forces on microscopic objects. Over the last few decades, this technique has become widely used as a non-contact manipulation tool in diverse fields, such as biology, material science, and physics, for the mechanical characterization of particles. These traps can capture and manipulate dielectric particles, cells, bacteria, and viruses. The distinctive characteristics a particle must present are having a high refractive index compared to the medium and being small; a typical length corresponds to 0.1-1000 nm.

2.2.1. The discovery of optical tweezers

In 1970, the physicist Arthur Ashkin published “Acceleration and trapping of particles by radiation pressure”,[118] where he described the first report of the acceleration of suspended particles in water and air through the use of a continuous laser. This work led to an understanding of the gradient force and the discovery of the first stable optical trap. Two configurations were showcase: for a single trap (single beam) the beads tended to be pushed along the direction of propagation of light, while for a dual trap (double beam), the propagation of light in opposite directions contributed to obtain stable spot for trapping the beads in the centre between the two beams.

That work laid the groundwork for many other papers studying radiation pressure, being recognized by many as the father of laser trapping and winning the 2018 Physics Nobel Prize whose prize motivation is “for the optical tweezers and their application to biological systems”.[119]

Subsequent discoveries includes the levitation of small glass spheres,[120] the demonstration of a single-beam gradient trap,[121] the first atom trap,[122] the trapping of living organisms, such as bacteria and viruses, without optical damage adopting the term optical tweezers,[123] and the trapping of cells using infrared laser beams.[124]

Constable et al. revisited the double beam trap in 1993. They created the first dual-beam trap using optical fibers to guide the beams to trap polystyrene spheres and yeast cells and provided an equation to calculate the scattering force for these two beams.[125] This led to related developments involving fiber-based traps, including lensed fibers for trapping beads,[126] a four-fiber divergent optical trap,[127] the optical stretcher as a means of deforming cells[128] and cell manipulation and characterization using a dual-beam laser trap.[129]

2.2.2. Optical trapping instrumentation

Optical tweezers can be incorporated into a microscope system or as an external trapping source. One of the strengths of optical tweezers is that they can be integrated and combined with different imaging systems such as bright field, differential interference contrast, phase contrast, and fluorescence microscopy for extended spatial range of applicability as well as with spectroscopic techniques.

In a typical set-up for cell biology applications a single-mode near infrared laser beam goes through a beam expander filling the back of a high numerical aperture (NA) microscope objective and then focused through a diffraction-limited beam waist, creating

a three- dimensional light gradient. The numerical aperture (NA) equals the index of refraction of the immersion fluid.

For external optical trapping system, the trapping laser can be coupled to a single mode optical fiber which produces a clean, Gaussian TEM_{00}-mode beam profile and it is relatively simple to implement a second optical trapping beam by splitting the trapping light based on polarization.

Optical fiber-based setups can be done in a variety of ways, involving either solid-core or liquid-core waveguides. In the former approach, light is guided by total internal reflection in a high index core.

Near-infrared wavelengths are the most common lasers used for entrapment. Typically, an Nd:YAG laser at a wavelength of 1064 nm is used due to its biological amiability as it produces significantly less photodamage by minimizing the absorption of light by water and biological specimens.

In conventional OT, the laser intensity profile shows a Gaussian radial distribution, a single central maximum with a bell-shaped beam. It is possible to trap and manipulate a single particle at a time using such a beam.

The stiffness and force of an optical trap depend on the intensity of laser power, the shape of laser focus, the size and shape of the trapped particles, polarization, and the index of refraction of the trapped particles relative to the surrounding medium.

Typical trapping forces range from sub-picoNewton to hundreds of picoNewtons. This range is sufficient to characterize the mechanism of individual biological systems.

2.2.3. Optical trapping theory

The fundamental physical principle behind OT is that light can exert pressure and forces on matter. As illustrated in Figure 2.3, the trapped objects experience two main forces: the scattering force (F_{scat}) produced by the photons striking the object along their propagation direction and the gradient force (F_{grad}) produced by a gradient of field intensity that pulls an object transversely inwards into a strong region of optical intensity. The magnitude of the F_{scat} and F_{grad} components exerted on the particles depend on the wavelength of the laser beam (λ) and the particle size (d). The direction of the force is independent of the particle shape, and its magnitude varies with the particle orientation.

In order to understand how an optical trap works, the trapping is described in two different regimes: Rayleigh regime, where d<< λ; and Mie regime, where d>> λ.[123]

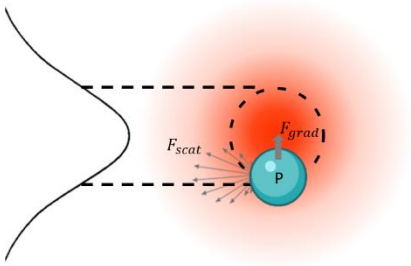

Figure 2.3 Schematic of the forces involved in optical trapping (Rayleight regime) optical tweezers. Particle (P) experiences two types of forces generated by a Gaussian beam. A force F_{rad} pulls P toward the high-intensity region of the beam, and a force F_{grad} pushes P along the direction of light propagation.

If the particle size is substantially less than the wavelength, then the particle is in the Rayleigh regime. The electric field of electromagnetic radiation (polarized light) induces an electric dipole moment μ in the object. The intensity of the dipole moment can be determined by:

$$\mu = \alpha E \tag{2.2}$$

Where α is the polarizability of the particle and E is the electric field. The induced dipole moment will be attracted towards the most intense part of that beam (I) with force, F_{grad}, where the induced dipole may minimize its energy. The gradient force can be calculated as:

$$F_{grad} = -\frac{1}{2}\alpha\nabla E^2 \tag{2.3}$$

Equation 2.3 shows that F_{grad} acts in the direction of the high-intensity regions of the beam proportional to the gradient intensity ∇.

Besides the gradient force, Rayleigh particles experience a force due to the scattering of light. When the photons hit the particle, some photons scatter away. Moreover, because each photon of the light carries an amount of momentum equal to the plank constant divided by the wavelength of light ($p = \frac{h}{\lambda}$), the particle experiences a recoil force proportional to the amount of power (intensity) that hits the particle.

The scattering force is proportional to the optical intensity and acts along the laser light propagation, drawing the particle into an equilibrium position slightly downstream of the maximum intensity. The competition between the two forces can result in stable trapping.[121]

In the Mie regime, where the particle size is larger than the wavelength, it is no longer possible to describe the interaction solely in terms of gradient force or scattering force, but trapping can be understood using conservation of linear momentum or ray optics.[130] According to Newton's second law, force can be described as the rate of change of momentum p of a system. As describe in Eq. 2.4:

$$F \equiv \frac{dp}{dt} \tag{2.4}$$

Figure 2.4 illustrates how any momentum changes from individual rays of light, when striking the particle, result in an equal opposite momentum change on the particle. Thus, stable trapping requires the balancing of the forces arising from reflection and refraction.

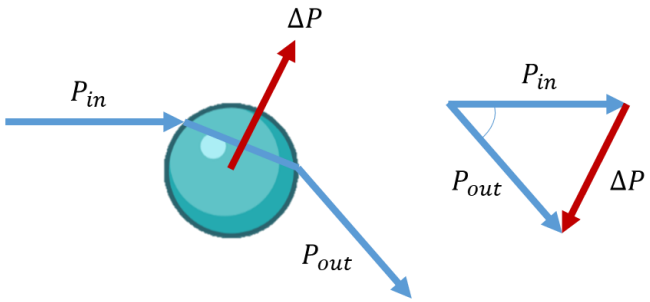

Figure 2.4 Conservation of momentum model. When the light reaches the particle, part of the light gets refracted on its way in (P_{in}) and again as it comes out (P_{out}) in a different direction. The light loses momentum proportional to delta P, which is the force that acts on the object with an opposite sign. In this case, upwards and forward.

Any momentum changes from individual rays of light, when striking the particle, result in an equal opposite momentum change on the particle. Thus, stable trapping requires the balancing of the forces arising from reflection and refraction.

A more intensive beam imparts a larger momentum change towards the center of the trap than the less intensive beam. When the particle is out of trapping focus, the net momentum change, or net force, can draw the particle back to the center of the trap. When the particle locates in the center of the trap, individual rays of light are refracting through the particle symmetrically, resulting in zero net lateral force and canceling out the scattering force of the laser light.[123]

The Mie regime includes biological particles such as cells, viruses, and bacteria. In this regime, both the magnitude and the direction of the forces depend on the particle shape.

Working with living organisms is limited by the trapping efficiency and the available laser power. These are deformable particles; therefore, stresses and consequent particle deformation result in a change in optical forces.

When a single cell is trapped, light hitting the cell surface changes the intensity and direction of the bouncing photons. Increasing the laser power to increase trapping forces leads to heating and potentially photodamage. In addition, the index of refraction of the cytoplasm varies among cell types and may depend on the local environment in different regions of a cell.

The arrangement of opposing optical beams produced from a beam splitter has been widely used to create dual optical traps. In this configuration, a cell becomes trapped at the point of symmetry by identical, divergent beams with any displacement from this center, leading to a restoring force. The trap placement can be either parallel or counter-propagating and controlled by a single laser source or by different x–y deflector systems.[131]

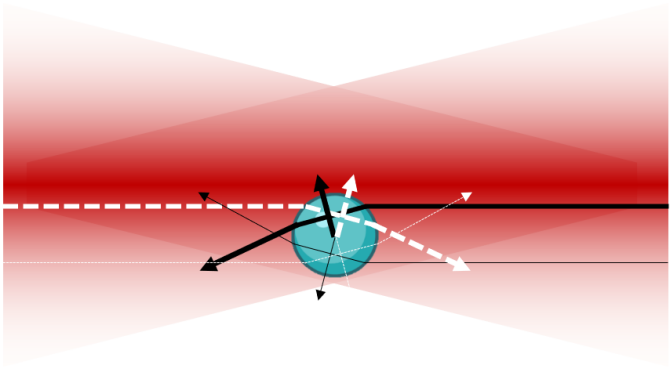

Figure 2.5 Schematic of two divergent counter-propagating beams (red cones) exerting a gradient force on an off-centre particle. The laser produces a force on the particle due to refraction and momentum change (black and white arrows). The larger momentum change of the more intense rays (thicker arrows) causes a net force to be applied towards the center of the laser or laser focus, while the outer rays (thinner arrows) cause a force pointing away from the laser.

Two divergent optical beams, Figure 2.5, rather than a single highly focused beam have several advantages. Homogeneous illumination is more easily obtained since the traps can be positioned horizontally relative to the imaging plane, making it possible to perform particle characterization experiments using a confocal microscope. The traps can be positioned independently; therefore, the user has three-dimensional control over the trap. Measurements can be performed far from possibly interfering surfaces while reducing photodamage or any two-photon-induced damage caused by a tightly focused light beam.[64]

Laser selection is a crucial parameter for the trapping of biological samples. The effects of illumination from OT using different laser powers, irradiation time, and wavelength on sample damage have been systematically investigated.[134] The photodamage throughout the near-infrared region favors optical trapping between 790–1064 nm. Shorter wavelengths below 760 nm can produce significant cell damage mainly due to photochemical effects, while at 800 nm and over, the cell damage is mainly due to photothermal effects.[132,133]

The integration of optical traps into microfluidic devices has shown to be a powerful combination for actively manipulating and positioning biological objects at the nano and microscale and several applications were conceived or became benefited by the incorporation of OT.

2.2.3.1. Optical Trapping for Cell isolation and manipulation

One of the most popular applications is to apply OT to confine or constrain cells at a predetermined position in a static or fluid flow environment. Single-cell isolation before molecular analysis allows spatial fixation without surface interactions.

The addition of microscopy techniques creates a powerful single-molecule manipulation and visualization tool with widespread application in biology enabling continuous

observation using advanced imaging techniques.[64] This method holds potential for *in vitro* monitoring of cellular drug response by feeding the pharmaceutical solution to the fixed cells and measuring physical and chemical changes in cellular components. Such is the case of combining Raman spectroscopy with OT and a microfluidic system. The oxygenation cycle of a single RBC selectively trapped by OT can be monitored in real-time while different buffers are transported through a microfluidic channel using electro-osmotic flow.[134]

2.2.3.2. Cell sorting

Another application in which OT can be applied is the contactless organization, assembling, relocation, and classification of individual cells in a liquid medium.

A popular function in microfluidic platforms is the sorting of cells either actively or passively, where the optical force from the light trap serves as a tool for cell deflection.[135] In the case of active sorting, cells require the addition of fluorescence markers that help them to be detected and separated from the sample bulk in a detection region within a microchip.[136] In an experiment by Tung in 2004,[137] two independent laser sources were used for cell sorting: a visible wavelength laser for fluorescence detection and measurement and a near-infrared laser for optical manipulation of the cells of interest. This microchip counted with different system stages; cells were hydrodynamically focused into an analytical region (IR light) and then through the optical switch region (Visible light). Once there, an acoustic-optical modulator is triggered to switch the cell based on the fluorescence signal when a cell is detected and determined to be a target cell. A focused laser spot deflects the cells into the output target channel, while the cells that do not show the signal flow to a waste channel without being subjected to a laser beam.

Unlike active sorting, passive sorting is an approach without markers, which has the advantage of keeping cell integrity since it is not necessary to develop an appropriate marker for cell identification nor to remove the markers after separation. In contrast, cells are sorted by a gradient force within a microfluidic channel depending on the size, shape, and refractive index of the cells, in competition with the viscous drag force of the medium.[138]

2.3. Raman Spectroscopy

Raman spectroscopy (RS) is a vibrational spectroscopic method that provides useful information about the chemical composition of a sample. This information is obtained by analyzing a Raman spectrum, the graphic representation of scattered light collected from a sample that exhibits a frequency shift with respect to the incident light. The energy shift reflects the energy of specific molecular vibrations within the sample of interest, but due to sample complexity, a substantial overlap of spectral contributions from all molecules in the spectra can occur; making it challenging to assign individual bands to single biomolecules and requiring the use of chemometric tools for data analysis, extracting information, and obtaining a specific spectral fingerprint. In other words, the chemical composition of a cell organism is associated with specific spectral patterns.

Raman scattering arises when monochromatic incident light on a sample is inelastically scattered, inducing transitions to vibrationally excited normal modes in molecules present in the interacting sample. Raman signal is relatively weak as the scattered light at a slightly different frequency represents close to 0.0001% of the collected light, only one scattered photon out of one million incident ones. The evolution of Raman as an analytical technique has led to the development of modern Raman spectrometers that overcome the low signal

challenge, filtering out the light that maintains the same energy as the incident laser (Rayleigh light) and conserves the Raman scattered photons.

Named after its discoverer, the Nobel Prize laureate, Sir Chandrasekhara Venkata Raman Singh Rajinder[139], Raman radiation has become fundamental in molecular spectroscopy techniques used in different fields of research such as semiconductors,[140,141] thin film technology,[142,143] polymer studies,[144,145] pharmaceutical chemistry,[146,147] process lines,[148] and biomedicine for the study of biological materials in particular biomolecules, individual live cells, and tissues.[149]

Raman is a non-destructive qualitative and quantitative characterization technique that can measure the molecular content of a sample. Raman analysis possesses several advantages, especially for *in-vitro* experimentation. As it is a label-free technique, sample manipulation can be limited to placing it on a transparent window under the microscope offering chemical selectivity using the intrinsic properties of the molecules.[150] Due to this attribute, no prior knowledge of the sample composition is needed in order to perform a Raman experiment. Therefore, it has the potential to measure previously unknown components in a sample. Besides, under the proper optical conditions, Raman allows performing multiple interrogations without damaging the sample, considering that all materials possess a laser power density threshold beyond which structural or chemical modification may occur.[151]

Raman allows for the interrogation and identification of materials as it is capable of differentiating chemical structures, even if they contain the same atoms in different arrangements, allowing its implementation in phase, polymorphy, and crystallinity research.[152] Raman provides molecular fingerprints that originate due to vibrations of the

molecule as a whole, rather than localized functional groups that are highly characteristic features of a specific molecule. These valuable spectral patterns allow monitoring changes in molecular structure during product formation and other more subtle effects of significant interest like stresses & strains.[153]

2.3.1. Raman principle

In the case of scattering, when monochromatic light illuminates a sample almost entirely of the scattered light will consist of photons of the same energy than the incident beam, but a small portion will consist of discrete frequencies higher and lower than the original beam.

These quantized frequency changes are known as Raman scattering and are the result of a polarization process consequence of the incident photons generating vibrational energy level transitions and promoting molecular vibrations within the material.

The scattered photons can be observed by collecting light at an angle relative to the incident light beam. Differently to what happens in absorption spectroscopy (i.e., infrared spectroscopy, IR), the energy of an incident photon does not correspond to the energy gap between the ground state of a molecule and an excited state, which is measured as the loss of energy from the incident light. Instead, there is no promotion to a higher energy excited state, what occurs is the formation of short-lived "virtual state". This virtual state is of little stability, turning in the quick transfer of energy released in the form of scattered radiation.

The Jablonski diagram shown in Figure 2.6 is typically used to describe the Raman effect and to illustrate the different forms in which photons are released depending on the original electronic state of the molecule and the interaction with light.

In Raman spectroscopy, when a laser of energy $E=h\nu_{ex}$ strikes a sample, the molecules get promoted to a higher “virtual state” (upward arrow), which generates vibrational and

rotational motions that result in a shift of energy after molecular relaxation (downward arrow).

In Figure 2.6b, when a molecule in the ground state is promoted to a virtual state that corresponds to the energy from the incident light, the molecule releases the excess of energy relaxing back to its original state by scattering a photon of the same energy than the original incident radiation. This phenomenon is called Rayleigh scattering, and it represents the "elastic" properties of the light in which case, the molecule relaxes to their original state ground or excited.

However, when a nuclear motion was induced during the scattering process, then the scattered energy will be different than the incident light, as some of the energy will be transferred either from the incident photon to the molecule or from the molecule to the scattered photon. These processes are both referred to as inelastic Raman scattering, regardless of the direction of the transfer.

The inelastic process can be either Stoke Raman scattering (lower energy photons) or Anti-stoke Raman scattering (higher energy photons). In Figure 2.6a the molecule is promoted from a ground vibrational state (v=0) and posteriorly emits a photon of reduced energy; this process is called Stokes's scattering, and the energy of this photon is equal to the difference between the incident light and the energy retained by the molecule, $E= h\nu_{ex}-\Delta E$; where ΔE is the energy of the vibrational transition.

In contrast, the process in Figure 2.6c is called Anti-Stokes scattering and occurs when a molecule in an excited vibrational state is promoted to a virtual state and decays back to a lower energy state or ground state, emitting a higher energy photon than the incident radiation ($E= h\nu_{ex}+\Delta E$).

The probability of finding the molecules in an excited vibrational state other than the ground state at room temperature is very low. Therefore, although both types of Raman signal represent equivalent vibrational information,[154] anti-Stokes scattering is an even weaker signal and will reduce the intensity as the frequency of the vibration energy increases, making Stokes scattering the predominant measurement of shifted light.

In order for a molecule to exhibit Raman signal (Raman active) the molecule has to undergo a change in polarization during the interrogation with laser light. The laser induces an electric field that in turn perturbs the electron cloud of the molecule causing the positively charged nuclei to be attracted towards the negative pole of the field, and the electrons to the positive pole. The separation of charges results in an induced dipole moment that disappears during the relaxation and reemission.

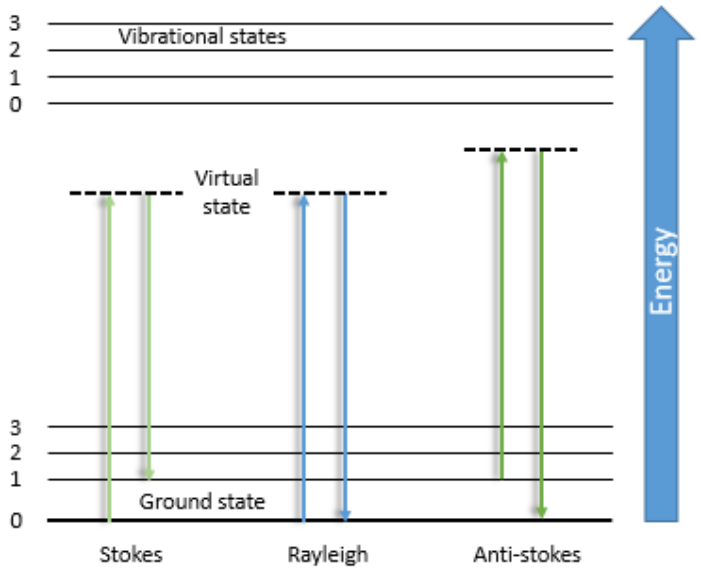

Figure 2.6 Jablonski Diagram of Energy Transitions for Rayleigh and Raman Scattering.

The polarizability of a molecule is directly proportional to the intensity of the Raman scatter produced, if there is no change in the polarisation during a molecular vibration then

no Raman scatter is observed. Therefore, only those vibrations that induce a change in bond length, e.g., symmetric stretches will normally be Raman active. The intensity of the Raman signal is also dependant on the intensity of the light source and other instrumentation factors.

2.3.2. Raman Instrumentation

A Raman instrument consists of four essential components: a light source needed to excite the target species (laser), a sample illumination and scatter collection system, a spectrograph to collect Raman scattering, filter out Rayleigh light and diffract the Raman shifted light into its wavelength components, and a detection system to record the signal. Figure 2.7 shows a simplified diagram of a typical spectrograph configuration. In this diagram, the light enters from the left side (in red) and passes through a dichroic beam splitter whose function is to transmit a wavelength to the sample. Subsequently, the light scattered off the sample (in blue) is collected back through the objective, filtered by the dichroic element where the Rayleigh light is reflected, and the Raman light is transmitted and focused through a pinhole onto the detector.

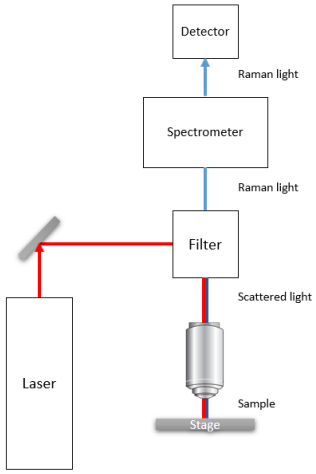

Figure 2.7 Schematic of a basic Raman spectrometer.

The choice of experimental parameters largely depends on the type of analysis to be performed and the materials to be examined and a proper configuration is fundamental for the collection of high-quality spectra.

2.3.2.1. Raman Microscope

In Raman microscopy, a confocal microscope is coupled to the spectrometer to visualize and magnify a sample while performing Raman analysis with a microscopic laser spot. The coupling makes it possible to control the collection volumes, allowing to analyze structures that are less than 1 μm while maintaining high sensitivity. The basic principle of a confocal system is the use of a pinhole to reject the out-of-focus light. In this method, only a small volume of the sample is imaged onto a detector.

Light exiting the laser source needs to pass through a series of filters and mirrors before reaching the sample. This is the function of the microscope which additionally upon laser interaction with the sample, collects the light scattering from the sample trough the objective to be then focused, and collimated into the spectrometer.

The spectral resolution is the smallest spectral feature that a sensor can resolve into separate components and is limited by diffraction.[155] The resolution is defined by the frequency and quality of the wavelength and the type of microscope objective selected. The following equation, deducted from diffraction theory, yields the minimum achievable spot size while using an optical microscope:

$$\text{Theoretical Spatial Resolution} = 0.61\frac{\lambda}{\text{NA}} \qquad (2.4)$$

Where, λ is the laser wavelength and NA is the numerical aperture of the selected microscope objective (optical system). The numerical aperture is a measure for angular

acceptance for incoming light or light-collecting ability of any lens. It is defined by NA= n sin α, where n is the refractive index of the medium between the objective and the sample (e.g., air, oil, water) and α is one-half of the opening angle of the objective (the half-angle of the light cone entering the lens) Figure 2.8.

This equation is for diffraction-limited spatial resolution, meaning that for a higher spatial resolution, a high magnification objective (higher NA) and UV laser excitation (shorter wavelength) will often produce better results. Nevertheless, this combination increases sample damage due to photobleaching or thermal decomposition. The higher the numerical aperture of a lens the greater the light-collecting ability and the finer are the details that can be imaged.

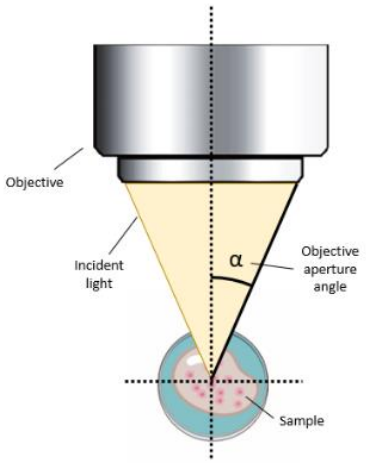

Figure 2.8 Incident light from an objective striking a sample.

The automated microscope stage and the positioning of the objectives facilitates the analysis of the sample volume in all three planes (X, Y, and Z) for lateral and depth observation. For a confocal microscope, depth resolution can be in the order of 1-2 µm, allowing the analysis of multilayered samples with features beneath transparent surfaces.[156]

2.3.2.2. Raman spectrometer

A spectrometer is composed of a series of filters and mirrors that serve two general functions: direct and condition the light exiting a laser source before its passage through a microscope system and process the scattered light upon interaction before reaching charge-coupled device (CCD camera).

A standard Raman spectrometer is depicted in Figure 2.9 showing the path of the laser from source to detector.

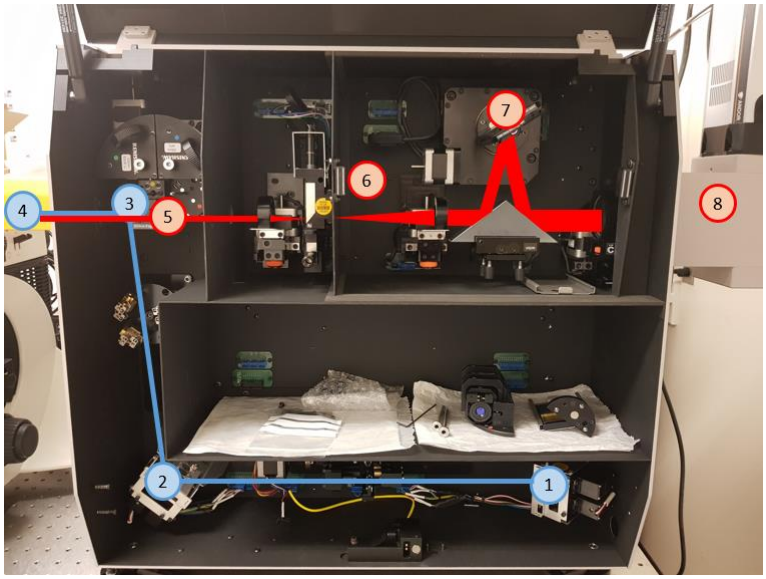

Figure 2.9 The internal configuration of a Renishaw Raman spectrometer. Showing the pathway of the excitation light between the light source (1) and the microscope objective (4). Passing through optical elements (2,3) to the sample and back from the optical microscope to the spectrometer to be detected by a CCD camera (7) after undergoing optical conditioning (5-7).

When the light coming from a laser enters the spectrometer, the first optical element encountered is a beam expander and a pinhole setup, which produces the laser beam to adopt a more circular shape. Once expanded, a mirror reflects the light upwards onto a long

pass edge filter or notch filter, reflecting the light at a working wavelength and transmitting any wavelengths greater than that.

The difference between these two commonly used filters is that a notch filter blocks a range of wavelengths around the central absorption of the frequency corresponding to the laser radiation (typically a few nanometers wide), absorbing the laser line and transmitting the Raman scatter. This type of filter allows for the collection of both Stokes and anti-Stokes's scattering. In contrast, an edge filter is a long-pass optical filter that reflects a wavelength range and transmits all wavelengths above this point with high efficiency. It possesses a lower cut-off, blocking everything below a specific value, usually a couple of nanometres above the laser wavelength. The edge filters have an ultra-steep edge between the absorbing and transmitting spectral region and offer excellent blocking of the laser line. This type of filter only permits the collection of Stokes scattering.

The filters are laser wavelength-specific and thus are interchangeable depending on which laser source is in use.

Once split, the beam is reflected into the back aperture of the microscope and focused onto the sample by the objective. After the interaction, the scattered light is collected with the same objective lens and focused on the spectrometer to be further processed.

Light collected is directed back to the filter that acts as a dichroic beam splitter that selectively blocks the Rayleigh scattered light while allowing the comparatively weak Raman scattered light through to the spectrometer.

The beam is then focused onto the entrance slit of the spectrometer. Light entering through the slit is collimated by a mirror and directed to a diffraction grating that disperses the light separating it into its different components. The grating determines the spectral

resolution obtainable and thus directly correlates to the amount and quality of information obtained from the spectrum. A lens focuses the light on the detector (CCD) to count the number of photons at a given wavenumber, producing the Raman spectrum.

Details specific to the spectroscopy system used in this work are discussed in Section 3.3.2.

2.3.2.3. Excitation sources

The wavelength selection and the laser power are fundamental factors in obtaining an adequate signal and working under experimentally compatible conditions. The wavelength dramatically impacts the scattering intensity, spatial resolution and maximizes the probability of producing superior quality spectra with Raman features not buried by fluorescence contributions. The presence of fluorophores in samples also contributes a broad background signal to the collected Raman spectrum.

Due to the weak nature of Raman scattering, it is imperative to deliver sufficient power to the sample in order to generate Raman scattered photons for detection in a reasonable integration time relevant to the clinical setting under consideration.

The scattering efficiency is directly proportional to the wavelength of the laser used. When no absorption from any electronic transitions of similar energies to that of the incident light occur, the efficiency increases as the fourth power of the frequency of the incident light. Hence, for improving Raman sensitivity, it is required to use the highest frequency possible; the shorter the wavelength, the more intense the Raman scatter produced. However, shorter wavelengths also mean a higher energy on the sample, leading to photochemistry and photodecomposition. In addition, when spatial resolution is

important, for example, for the collection of imaging data instead of single-point spectra, a shorter wavelength can produce much lower spatial resolution when compared to longer wavelengths.

Therefore, longer visible and NIR sources at wavelengths such as 633, 785, and 830 nm are preferred over those in the UV/VIS to reduce the amount of fluorescence interfering with the detectable Raman signal. Nevertheless, this choice is not straightforward, as competing factors often govern selecting appropriate NIR wavelengths for excitation. The longer the wavelength, the lower is the fluorescence and scattering background to be rejected; however, the Raman scattering also decreases.

Furthermore, the properties of the target tissue or sample are one of the major criteria for choosing a laser excitation source for a clinical Raman instrument. Many compounds absorb UV radiation, meaning that the spectra may differ from standard Raman spectra due to resonance with any electronic transition, which may cause absorption, changing the relative intensities of the bands. Strong absorbing molecules in a sample can also lead to the generation of excess heat deposition, which can cause damage with high irradiance.

Likewise, the presence of strong fluorophores can generate signals that overwhelm the modest Raman peaks that are concurrently detected.

Tissues such as the breast that do not have strong autofluorescence signals relative to the Raman features can be collected with several different wavelengths; however, highly auto fluorescent tissues like the kidney require the use of longer excitation wavelengths to obtain useful Raman spectra.

2.3.3. Raman and microfluidics

The combination of microfluidic technology with RS has shown to be particularly useful at solving problems in biological studies. Raman microfluidic systems capitalize on the exceptional spatial control of the Raman excitation laser achieved with Raman microscopy. Its practical integration with a confocal microscope allows the manipulation and study of low concentration analytes with a high degree of selectivity and high collection efficiency of the objective lens while allowing real-time monitoring processes.

Together this is an ideal combination for studying micron-sized particles such as single cells, as microfluidics provides controlled manipulation of small fluid volumes. At the same time, Raman offers the advantages of obtaining a full vibrational spectral profile[157] in an environment that is amenable to cell viability due to its compatibility with the study of samples in aqueous media.

3. Optofluidics Device: Design, Fabrication, and components

An optofluidics system, as described in section 2.1.3., is a device in which optics and fluidics operate in conjunction to create novel functionalities. The microfluidic platforms presented in this work have as a basic structure a fluidic element, a central channel to facilitate the flow of suspended particles, and an optical element, a fiber-based optical trap for their positional manipulation.

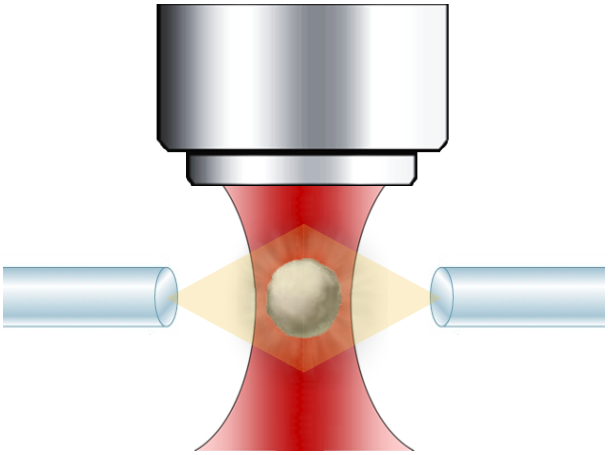

Figure 3.1 Cross-section configuration, consisting of a primary channel for the flow of suspended particles to an examination area, located at the interception of two optical fibers orthogonal to a microscope objective.

The general configuration of the microfluidic devices is shown in Figure 3.1, with the addition of a microscope objective that acts as a tool for visualization and as an interrogation device for Raman spectroscopy.

This section describes the optical elements used to develop two cytometry platforms for the acquisition of Raman spectra, together with the rationale behind the selection of those elements and the steps followed for the development of our platforms.

The first configuration consists of a system based on a microcapillary to facilitate the flow of mammary cells for preliminary studies and proof of concept of optical entrapment.

The second is a device based on a microfluidic chip with a design that evolved from the investigation results of the microcapillary system.

Additionally, a reconfigurable microscope platform was developed to adapt both devices into a microscope stage and the connections used in microfluidics and the optical fibers for trapping.

3.1. Microfluidic platform 1: Capillary-Based system

The first microfluidic platform fabricated was capillary-based. The design follows the cross-section configuration presented in Figure 3.1, with the use of a fused silica capillary to simulate a microchannel in a microfluidic device. This setup is a modified version of experiments performed by Dochow (2010) and Jess (2006), described in section 1.4.

3.1.1. System design

The main fluidic element of the system consists of a fused silica capillary column (Polymicro Technologies, Phoenix, AZ USA) with a square cross-section. The capillary has an external dimension of 300 x 300 µm and an internal of 50 x 50 µm (Figure 3.2)

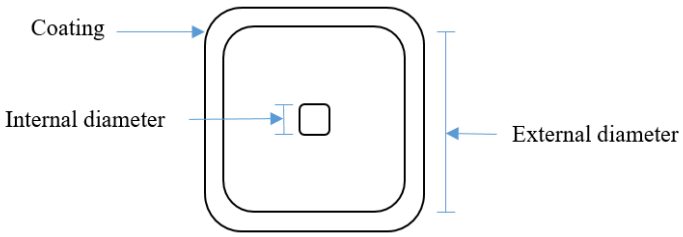

Figure 3.2 Crossection view of a 350 µm x 350 µm fused silica capillary, including a 50 µm coating and an internal dimension of 50 µm x 50 µm.

Using a fused silica capillary for suspended particle flow provides several advantages. Fused silica poses a high damage threshold for the passage of high-power laser light, it

shows a relatively flat Raman spectrum with less intense bands in the biological window of interest than glass, resists chemical cleaning required for multiple uses of the flow channel and is less expensive than other materials such as quartz.

In addition, the planar walls of the capillary reduce optical distortion of the lasers used for trapping and examination, minimize shear stress produced from the optical fibers placed against the material, and allow the precise calculation of the laser beam propagation from the fiber ends to the location of the cells in the center of the capillary.

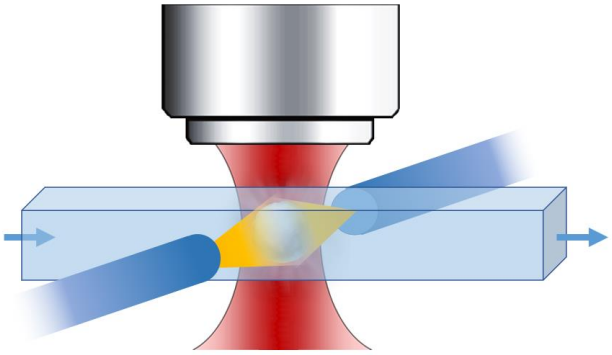

Figure 3.3 Diagram of capillary setup.

The capillary exists between two optical fibers facing each other in the same plane, orthogonally to a Raman laser beam, as shown in Figure 3.3. The interception of these three system elements creates an examination area for the optical manipulation of the sample during the acquisition of Raman spectra.

PEEK (Polyetheretherketone) tubing (IDEX Health & Science LLC, Harbor, WA USA) was selected to load the sample into the capillary, due to biologically compatibility and resistance to high internal pressure. The capillary was connected to internal reducing unions and graphite ferrules (VICI Valco Instruments, Brockville CA), indicated in Figure

3.4, to match the internal diameter of the capillary and avoid the vortex effect at the capillary inlet while coupling the capillary with the syringe pump system.

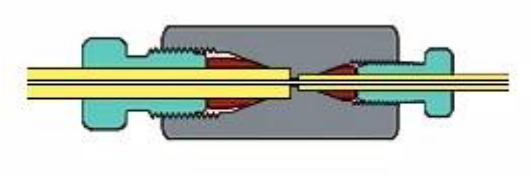

Figure 3.4 Zero dead volume reducing union.

To guarantee stable trapping of cells, the fiber cores require to be aligned with each other. The proper alignment minimizes possible fiber power loss and produces a proper signal transmission and a proper field intensity distribution.

The fiber core of the single-mode optical fibers used in this project is approximately 5 µm; therefore, to obtain proper alignment of the fibers to each other and to the capillary, a translatable microscope stage holder was developed for a precise adjustment of the mechanical settings.

3.1.2. Aligner stage

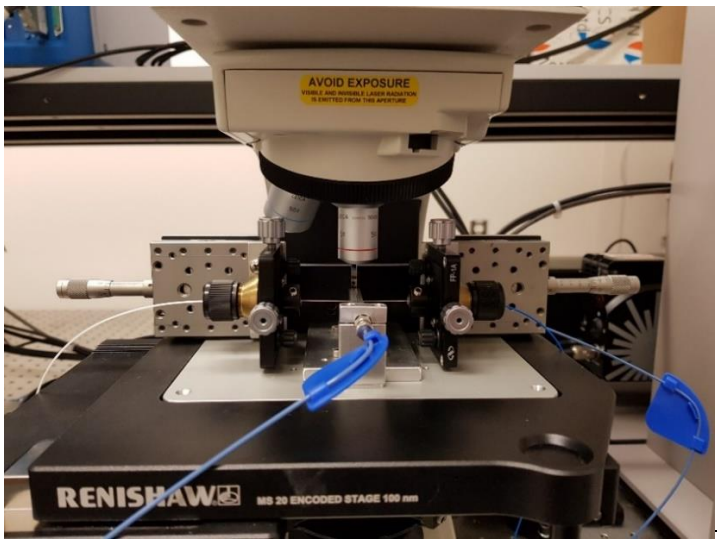

Figure 3.5 Optofluidic platform on a Raman microscope stage.

The aligner, shown in Figure 3.5, was fabricated in the University of Victoria Machine shop. The stage showcased in Figure 3.6 consists of a shared metal plate that holds a series of stages and holders (Newport Corporation, Irvine, CA USA). Two Linear Stages (UMR5.16) coupled to Micrometer Heads (BM11.16) were attached to the shared plate and two Fiber Optic Positioners (FP-1A) to support brass fiber holders (FPH-S-2.5) were installed parallel to each other onto the linear stages.

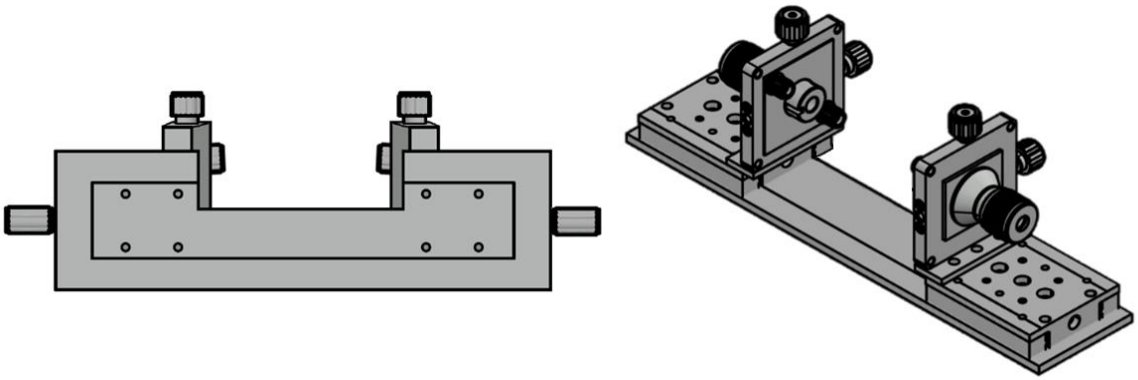

Figure 3.6 3D view of optical fiber alignment stage.

This configuration permits the adjustment of the fibers in the X and Y plane with a sensitivity of 0.75 µm, while the Linear stages allow the *Z* plane adjustment with a sensitivity of 1.00 µm.

The holder was designed to fit our InVia Renishaw microscope (Prior Scientific Inc., Rockland, MA USA); however, it can be modified to be incorporated onto any other commercial microscope and avoid modifications of the microscope stage.

The motorized sample stage from the microscope provides additional translational control within 0.1 µm steps along the x, y, and z directions.

The capillary lies on a metal block attached perpendicular to the shared metal plate by holders positioned at both ends of the capillary (Figure 3.7). These secondary holders allow

modifying the height of the block to adjust the capillary relative to the trapping fibres (*y* plane).

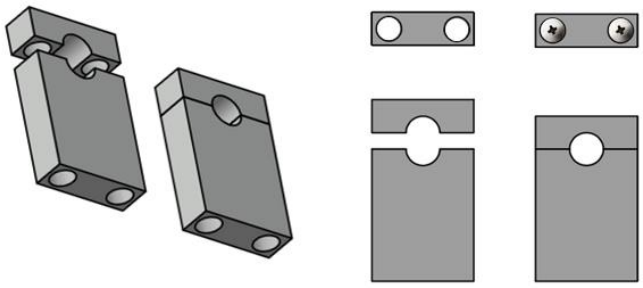

Figure 3.7 Metal holders that clamp capillary unions in place. Perspective view.

The stage (Figure 3.8) allows for the simultaneous use of optical fibers and microscope objectives for simultaneous illumination from both sources.

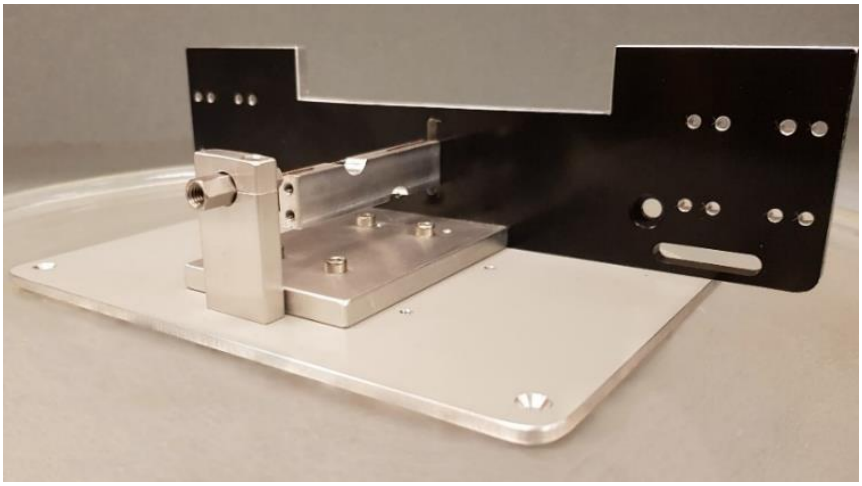

Figure 3.8 Aligner stage front view with capillary union holder and capillary holder.

3.2. Microfluidics platform 2: Microchip system

The primary goal of this microfluidic chip is to allow the detection of the changes that a cancer cell undergoes after radiation exposure. The microchip must meet specific

requirements to successfully integrate our Raman spectroscopy approach into the microfluidic environment to obtain reliable results.

3.2.1. Transparency requirements for optical measurements

As Raman scattering provides a relatively low signal, background noise can easily overpower the information pertaining to the analytes. The transparency of the microchip's substrate is crucial to avoid interactions with the incident laser, reducing contributions from outside the focal volume.

MgF_2 is a transparent optical material that exhibits excellent broadband transmission from 120 nm to 8 μm, from the deep UV to the mid infrared. Table 3-1 shows material specification for MgF_2, relevant during the process of optical window selection.

Table 3-1 Magnesium fluoride (MgF_2) properties.[158]

Property	Value
Transmission Range	0.12 to 7 μm
Refractive Index	1.413 at 0.22 μm
Absorption Coefficient	5.5 x 10^{-3} cm^{-1} at 2.8 μm
Density	3.1766g/cm^3 at 25°C
Melting Point	1255°C
Boiling point	2260°C
Thermal Conductivity	28 W/m K
Thermal Expansion	13.7 (para) 8.9 (perp) x 10^{-6} /K
Specific Heat Capacity	1003 J Kg m^{-1} K^{-1}
Dielectric Constant	4.87 (para) 5.45 (perp) at 1MHz
Youngs Modulus (E)	138 GPa
Apparent Elastic Limit	49.6 MPa (7200 psi)
Solubility	0.0002g/100g water
Molecular Weight	62.302 g/mol
Class/Structure	Tetragonal P42/mnm (#136) Rutile Structure. Can cleave on c-axis but not easily.

3.2.2. Biological compatibility

Toxicity or stress produced on the cells can give rise to unwanted spectral Raman contributions that are hard to distinguish from the ones produced by ionizing radiation.

The use of MgF_2 and PDMS follows compatibility requirements,[69,70] including their compatibility to the cellular aqueous medium.

3.2.3. General Layout of the Microchip

The choice of MgF_2 as a substrate poses significant challenges for its manufacture. Although adequate for our optical analysis conditions, it possesses fundamental limitations that make it non-suitable for traditional microfluidic fabrication processes.

The fragility of MgF_2 hinders drilling, one of the most common approaches for producing inlets and outlets to link the device with the macroenvironment; furthermore, as an inert material, it is not affected by techniques such as chemical etching for creating channels nor is suitable for plasma bonding.

Another factor that plays a role in the platform design and dimensions is the addition of external elements. The ideal device should house and accommodate the connections necessary for optical traps (e.g., optical fibers, fiber holders, aligners), related microfluidic elements (e.g., tubing, connectors), and optical elements (i.e., microscope lenses).

3.2.4. System design

Due to the system requirements listed above, the design of the platform consists of a casted polymeric layer stacked between two transparent substrates. The overall layout of the chip is shown in Figure 3.9

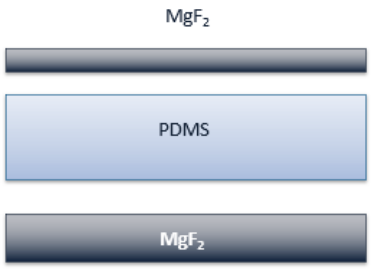

Figure 3.9 The layered device comprises three tiers: (from top to bottom) a MgF_2 top window, a PDMS layer for microchannels formation, and MgF_2 base.

The polymer layer contains the pattern that will eventually form the microchannels once bonded with the top and bottom windows. A finished microchips design consists of a cross-section configuration formed by three straight channels: a central channel for the flow of the sample (flow channel), situated between two non-continuous channels perpendicular to the flow channel, designed to guide optical fibers towards an interrogation point (fiber channel) (Figure 3.10). The gap between the flow and fiber channels avoids the contact of the fiber with the flowing liquid, ensuring sterility and a leak-free flow. Making the fiber ends remain clean of biological debris which could otherwise cause destructive absorptive heating and beam deterioration

The channels in our microfluidic platform are formed once the polymer layer is placed between two layers of transparent material, in this case, MgF_2. The PDMS layer was design to extend beyond the circular MgF_2 window to accommodate additional pieces of PDMS. The smaller and thicker PDMS pieces will cover and seal by plasma bonding the remaining exposed flow channel (the channel ends not covered by MgF_2). The thickness of the added piece will serve to hold the connections of the inlet and outlet that link the microchip to the macroenvironment.

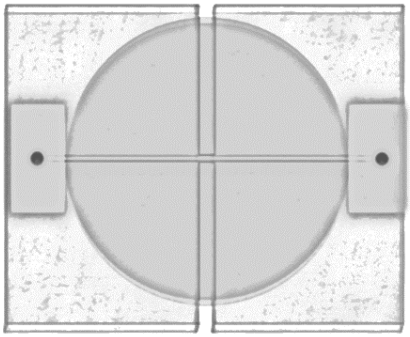

Figure 3.10 Top view of a sealed microfluidics chip. The diagram shows a cross-section configuration of a primary channel for the flow of suspended particles to an examination area, located between two non-continuous channels, perpendicular to the main channel, designed to guide optical fibers towards the interrogation point. In this configuration, the two layers of MgF_2 sandwich the polymer, sealing the microchip and creating the channels.

The suggested design offers a simple solution to overcome the two main limitations associated with MgF_2, its fragility that prevents drilling holes for microfluidic connections and its lack of oxygen in its molecular structure, making it unable to bind to PDMS by plasma bonding. Moreover, the similarity in the chip's design with the configuration of the capillary-based system facilitates the translation of results obtained by the fused silica platform.

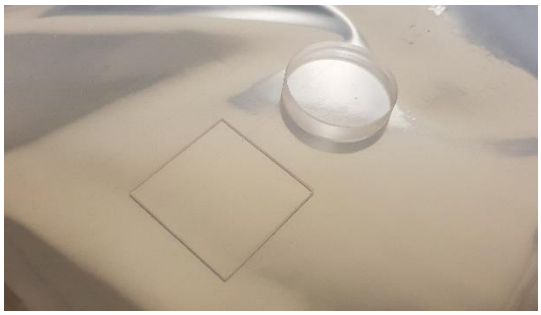

Figure 3.11 Slide vs disk vs window 170 µm thick.

Different varieties of one-channel microchips were implemented. The difference between these designs was the presentation of MgF_2 used for covering the examination area in the PDMS layer (Figure 3.11), including MgF_2 windows (170 µm thick, 25 mm

diameter, Global Optics UK Ltd, Poole, UK), MgF_2 disk (Global Optics), or MgF_2 slides (Crystran Limited, Dorset, UK) for sealing the system. (Figure 3.11).

The different platforms were subjected to experimentation to test their suitability in the manufacture of the chip of interest. The configurations are presented in Figure 3.12.

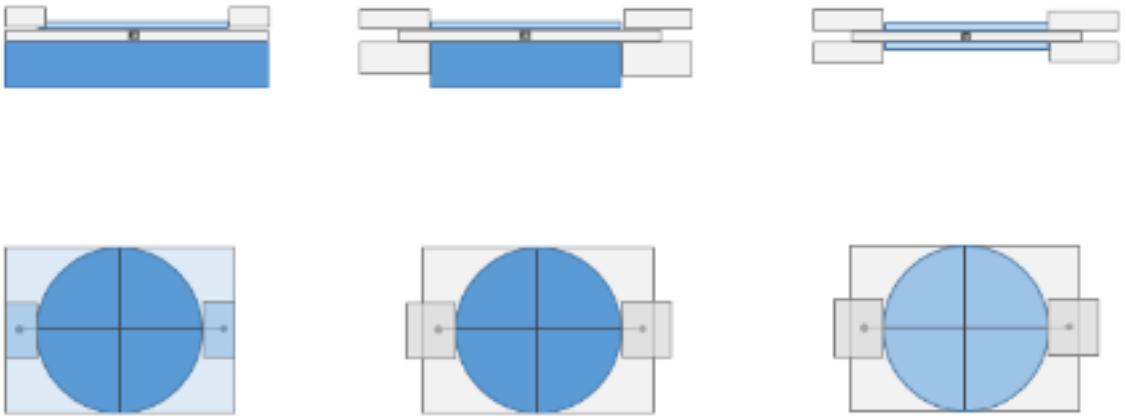

Figure 3.12 The schematic shows the side and top view of the three similar microfluidic prototypes. The horizontal line represents the flow channels, and the vertical one the channel, capable of fitting optical fibers with room for alignment. The small circles are ports to interface the device with a syringe pump. The chip design therefore uses the same basic design as the capillary setup with one inlet and one outlet to pump either in or out the fluid into the flow channel.

3.2.5. Chip Fabrication

The fabrication of the three-layer microfluidic device starts with the creation of the middle PDMS layer by photolithography.

The microfluidic mold was fabricated using a modified version of a MicroChem SU-8 2000 protocol for ultra-thick layers. The photolithographic process was used as a guideline to obtain ultra-thick SU-8 molds. The aspect ratio (height vs. width of a channel) is one of

the fundamental properties that need to be considered while designing a microfluidic device. This property is inherent to the material, therefore procuring a 1:20 or less aspect ratio for SU-8 ensures an optimum design without the risk of walls collapsing during the subsequent steps of the master mold fabrication.[159]

Reusable negative master molds were produced by photolithography using Prime quality silicon wafers (Silicon Materials, Inc., PA, USA) and negative photoresist SU-8 2075 (Microchem Inc.). Before spin coating, which refers to the spinning of a flat substrate with a thin layer of solution that leads to a uniform film, the wafers were placed on a hotplate for moisture removal. This dehydration process helps to increase SU-8 adhesion to the wafer and takes around 20 min to become completely dehydrated.

Subsequently, the microfluidic channels were cast using polydimethylsiloxane (PDMS) by soft lithography.

Multiple layers of SU-8 2075 formulation were deposited and spin-coated onto the wafer to obtain an ultra-thick film of 700 – 1000 μm. Approximately 1 mL of photoresist was dispensed per inch of wafer diameter (3-4 mL for a 3-inch wafer) and spin at 1000 rpm for 30 seconds at an acceleration and deceleration time of 10 s. A Soft bake process followed it on a level hotplate with a uniform temperature set at 65˚C and baked for ~15 minutes with a posterior increase to 100 ℃ for ~2 hours when the evaporation decreases, the thickness too and increases the layer hardness.

After baking, the silicon wafer cooled down to room temperature on a turned-off hotplate. To guarantee the wafer is ready for the subsequent coating, it was recommended to return the hotplate to 60°C and wait for the film to "wrinkle." The presence of wrinkles works as an indicator of the remaining amount of solvent within the SU-8 layer. Therefore,

it is necessary to warm up on the hotplate for 60 to 120 min. The cool-down and heat cycle are repeated until no more wrinkles (no solvent contamination) are present in the film.

The resultant thickness of the first SU-8 layer was ~225 µm approximately. The exact process was performed for the second and third layers with increments of 1 hour per number of layers during the soft bake. Their thicknesses are indicated in table 3.3.

Table 3-2 SU-8 thiskness layering

Layer	Thickness
1	225 µm ±5
2	550 µm ±10
3	700 µm ±20

In order to generate the wells in the SU-8 master mold, a photomask (Figure 3.13) was placed in contact with the SU-8 multi-film using a mask aligner (OAI 800 MDL, Raith 50 and UV 21052C) and exposed to UV light (350 W Hg lamp from a Short ARC lamp) for 25 s. Subsequently, the UV-treated film was immediately hard-baked on a hotplate at 100 °C for 60 min and posteriorly cooled down overnight to avoid thermal shock and cracking.

The wafer was subject to mild agitation in SU-8 Developer (product information) to remove the non-crosslinked SU-8. Lastly, the wafer was rinsed with isopropanol before microscope quality inspection.

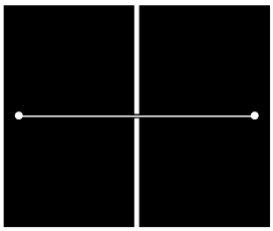

Figure 3.13 AutoCAD design of the microfluidic chip containing a single central channel for the injection and recovery of particles and cells and two optical fiber channels with marks for inlet and outlet holes.

The master was placed under vacuum in the presence of 50 µL of silane (Trichloro (1H,1H,2H,2H-perfluorooctyl, 97%) per wafer for 60 min to increase the hydrophobicity of the negative master and improve the later removal of cured PDMS after soft lithography. Subsequently, the master was placed on a hotplate for 60 min at 100°C.

After the developing process, a microchip's polymer layer was created using the silicon elastomer PDMS (SYLGARD 184 kit, Dow Corning, Midland, MI) at an elastomer-curing agent ratio of 10:1. Uncured PDMS was poured within the pattern created on the master mold, as shown in Figure 3.14b. An essential requirement was to ensure the PDMS level remained below the height of the crosslinked SU-8 walls. Posteriorly, a MgF_2 window was placed on top of the uncured PDMS and the raised features that will form the examination area, Figure 3.14c. After gently and evenly pressing the window, the mold was baked using an oven at 70°C for 6 hours, causing the window to become affixed to the polymer layer. The resultant layer piece was peeled off cautiously of the mold to avoid breaking or separating the MgF_2 coverslip from the cured PDMS.

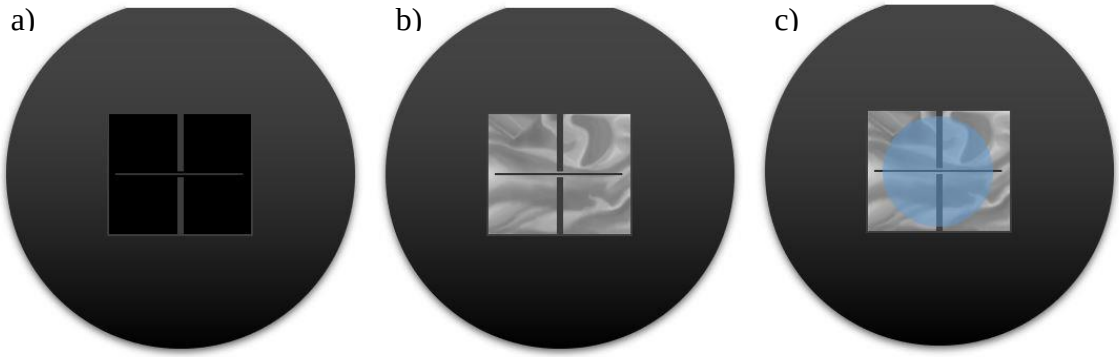

Figure 3.14 Illustration of the soft lithography process for the creation of a PDMS-MgF_2 chip. (a) SU-8 master mold created by a photolithographic process on a Si wafer substrate (dark gray); the black area represents the pattern created in the negative photoresist after developing. (b) PDMS (light gray) poured within the developed SU-8 pattern. (c) A MgF_2 coverslip placed over the PDMS, and crosslinked SU-8 walls photolithographically created.

Once the MgF_2 coverslip was attached to the PDMS layer that contains the mold features, the next step consisted in pressing the PDMS layer against another MgF_2 substrate. Figure 3.15 shows the formation of the microchip. After gently pressing the polymer against the disk, the materials became joined by contact forces. The length of the flowing channel was purposely designed to protrude from opposite sides of the window.

The remaining opened channel ends were covered using two additional PDMS pieces (≈1.5x1.5 cm). and attached by plasma bonding. The first step in plasma bonding is to make any needed holes in the PDMS (i.e., fluid inlets and outlets). Both the PDMS layer and the smaller PDMS pieces were placed into the chamber of the plasma bonder for a brief exposure to plasma treatment. The PDMS pieces were placed in position, brought into immediate contact, and pressed together with the PDMS layer. For this purpose, the PDMS pieces should overlap the edge of the MgF_2 window to hold it against the PDMS layer. The PDMS pieces were now irreversibly bonded via strong Si-O-Si bonds.

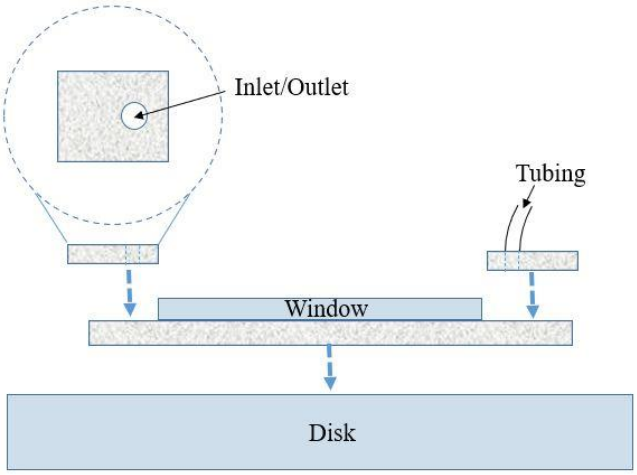

Figure 3.15 Depiction of the sealing steps of a PDMS (gray) - MgF_2 (gray) chip. A PDMS layer with an attached MgF_2 window is pressed against a MgF_2 disk. Additional pieces of PDMS with an inlet and outlet for accommodating a tubing connection are positioned at both ends of the window and plasma bonded to cover the open flow channel ends.

Lastly, uncured PDMS was used as glue for securing the edges of the PDMS pieces and placed in the oven at 70°C for crosslinking. The result, a sealed microchip with side openings for the insertion of an external optical trapping setup.

3.3. Lasers used in this work

3.3.1. Laser diode for optical trapping

Diode lasers utilize electro-optical components (diodes), which emit light as a function of both applied current and operating temperature. Laser diodes characterize by their small size and elliptical beam output (rectangular shape). Diodes themselves are small and require highly accurate controlling electronics to obtain the stable output necessary for optical trapping.

The trapping beam is generated using a compact Laser Diode Driver (cLDD), Figure 3.16, that combines a laser mount with built-in laser current and TEC (thermoelectric cooler) drivers in a single unit (Innolume GmbH, Germany).

Figure 3.16 (Left)Top panel view of cLDD, showing LCD display, two status LEDs, control buttons, and 14-butterfly mount. (Right), Single mode optical fiber with an FC/APC connector.

The cLDD is configured as a 60 mA to 2.0 A laser diode current driver, with a 14-pin butterfly mount for a 1064 nm diode laser. The driver was operated as a stand-alone system

(disconnected from a computer) and parameters such as laser diode current, output power, temperature, mode of operation, were adjusted via local keypad and display.

The laser beam launches into a high index of refraction core and high numerical aperture single-mode optical fiber (Corning HI 1060 Specialty fiber for high photonic applications) (Corning Incorporated, NY, US) with a core of approximately 5.3 µm in diameter.

After light is launched from the cLDD into the single-mode fiber the light is directed into a 50:50 beam splitter (Gould Technology, LLC). The splitter is a wavelength flattened coupler formed by placing two or more independent optical fibers adjacent to each other, fusing, and stretching them to create a central coupling region. The incident light is separated into two individual single mode fibers (arms) with the same optical power as shown in Figure 3.17. Each arm emerges from the coupler with a 900 µm jacketing and FC/APC connectors.

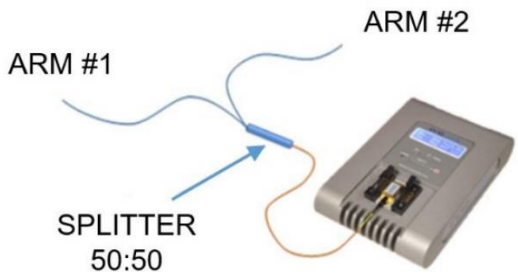

Figure 3.17 Diagram of 50:50 beam splitter used for dividing the diode laser light into equal amplitudes traveling along the two fiber arms.

A laser diode produces a divergent beam with a gaussian intensity profile and plane wavefronts in focus. This beam characteristic reduces biological material damage during double beam trapping and produces a more stable grip. A detailed explanation about double beam OT is presented in Section 2.2.

A parameter for efficient optical trapping is the use of fibers with a clean and smooth end face. If the fiber ends were not cleaved properly and solid contaminants were present, fiber loss would occur, which in turn could affect the transmission of signals, increase back reflectance, and produce non-symmetrical beam face circumference.

A cleaver produces a crack on the fiber that creates a flat end after applying some tension along the fiber to split it. A high-efficiency cleaver provides a suitable surface for optical trapping.

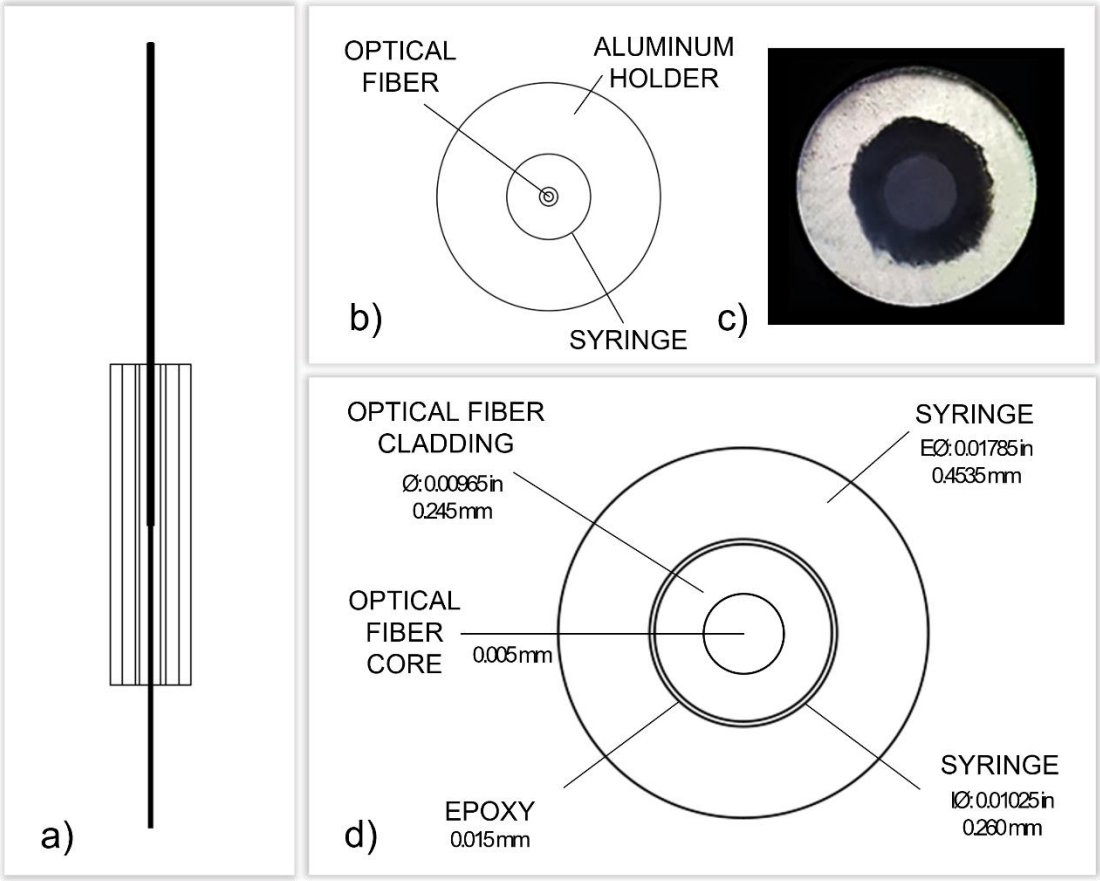

Figure 3.18 Elements of an aluminum holder for optical fibers a) cross sectional side view of fiber holder, b) top view of fiber holder, c) picture of a flat end face optical fiber fixed inside of a syringe needle after a polishing process, d) Diagram of the elements that constitute the optical fiber holder.

Likewise, a polishing process avoids back reflection to which high-power fiber devices such a CLDs are often susceptible. Moreover, as the effective mode area is relatively small, fiber ends are easily destroyed by reflection proportional to the laser power.

For our purpose, the fibers were incorporated in an in-house fiber holder to obtain an equivalent smooth surface that substitutes the use of expensive tools while reducing the loss of limited fiber length during traditional cleaving, Figure 3.18.

The FC/APC connectors were removed to perform the stripping of the jacket and cladding (≈10 cm) of the fiber, followed by the cleaving in the fiber's longitudinal axis. Following the preparation of the fiber, the stripped core was introduced into an aluminum holder to be semi-permanently glued in position by using commercial epoxy glue. Excess glue was removed, and the end face of the fiber exposed at the end of the holder was polished until a flat end termination was obtained using reducing gratings of sandpaper and polishing sheets (Thorlabs, Newton, NJ USA). Separately, both single-mode fibers underwent the same process. The optical arms were mounted on a translational stage (Section 3.1.2) used for aligning the fiber cores relative to the flow channel of the microfluidic devices.

Due to the nature of the single-mode fibers, the beam diverges upon fiber exiting. The beam radius varies along the propagation direction due to diffraction effects. In the case of a beam traveling between two optical fibers separated by a gap, the quality of the propagation depends on laser wavelength, the width of the gap, and the material between the fiber ends. The beam diameters produced in each experimental setup were mathematically calculated, and detailed information can be found in Appendix A.

In the case of the experimental setup presented in Figure 3.3, the two optical fibers ends are placed close together with a gap between them that corresponds to the width of the respective microfluidic channel. The beam thus travels into another medium, passing through a planar interface while keeping its Gaussian profile and divergent properties just with modified parameters.

3.3.2. Laser Excitation from the InVia Renishaw Raman spectrometer.

Optical excitation was produced by continuous wave laser operating at 785 nm coupled to a Renishaw inVia Raman Microscope controlled by WiRE software version 4.4 (Renishaw Inc., Illinois, IL USA). An image of the Raman microscope is shown in Figure 3.19. The WiRE software facilitates sample visualization, control of spectral acquisition parameters, data display, and the control of lasers, grating, detector, and filters.

Figure 3.19 Renishaw Confocal Raman microscope

The microscope coupled to the Raman system is a regular upright microscope equipped with objectives (Leica Microsystems, Wetzlar, Germany) 5 -100x for visualization from which the 50x and 100x 0.75 NA and 0.9 NA, respectively were used for collection of

scattered light. The output power of the laser was measured using a 50x and a 100x objective at different laser power percentages.

Table 3-3 Power output (±5mW) of a 785 nm continuous wave diode

Objective	100%	50%	10%	5%	1%	0.5%
50x	92mW	52 mW	17 mW	8.8 mW	4.5 mW	2.4 mW
100x	54.3mW	29 mW	9 mW	4.0 mW	2.5 mW	1.3 mW

The spectrometer is equipped with a rotating diffraction grating that allows the selection of two groove densities 600 $^{l}/_{\mathrm{mm}}$ or 1200 $^{l}/_{\mathrm{mm}}$ which spatially disperses the scattered light. As well a 1024x127 pixels CCD camera (Andor Technology, Conneticut USA) of 26 x 26 μm^2 pixel size.

4. Experimental details

A series of experiments were carried out for the testing of the microfluidic platforms described in Section 3. These tests consisted of the structural validation of the platforms and their ability to facilitate the sampling of cells for Raman spectra. Both qualities were judged based on their potential suitability to serve as a tool capable of easing the Raman spectroscopic approach for detecting cellular changes developed by our group and automating the sample handling for the spectra collection process currently carried out in the macroscopic environment.

Among the tests includes the structural assessments of the platforms to determine the correct manufacturing of the chip or the correct installation of the microfluidic components in the capillary system (e.g., tubing connectors) to avoid common problems found in microfluidics (Section 2.1.1), followed by their spectroscopic interrogation to determine the spectral contribution of the substrates.

Additionally, this project introduces a novel method to manufacture microfluidic chips constituted by challenging substrates to handle due to fragility and inert nature, as in the case of MgF_2. The following spectroscopic studies assisted to discard possible contamination created during the fabrication process.

The ensuing experiments observed the efforts to confirm the capacity of the systems to accommodate the spectroscopic screening of cancer cells. The validation was carried out by the initial flowing of polystyrene beads with the subsequent study and flowing through the microsystems of two breast cancer cell lines, MFC-7 and MDA-MB-231, for qualitative measurements using Raman spectroscopy.

4.1. Samples

Uniform Polystyrene Latex Microspheres (5 µm) in aqueous suspension with a polymer density of 1.05g/mL were purchased from SPI Supplies Division. The cell lines MCF-7 (HTB-22; 20 - 25 µm) and MDA-MB-231 (HTB-26; 18 - 25 µm) were obtained from the Facility of Biomolecular Sample Preparation at the University of Victoria, which required Phosphate buffered saline (PBS) purchased from Sigma-Aldrich; Dulbecco's Modified Eagle's Medium (DMEM), Dulbecco's Modified Eagle's Medium (DMEM) phenol red free, Eagle's Minimal Essential Medium (EMEM), fetal bovine serum (FBS), penicillin-streptomycin, 10X Presto Blue cell viability reagent, LIVE/DEAD viability/cytotoxicity kit for mammalian cells, and Pierce TM 16% Formaldehyde (w/v) methanol-free purchased from Thermo Fisher Scientific. Millipore Milli-Q water with a resistance value of 18.2 MΩ x cm was used for all aqueous solutions.

4.1.1. Preparation of microspheres solution

Polystyrene (PS) bead solutions of different concentrations were prepared for several assays. The solutions were prepared by diluting aliquots from the original 15 mL vial of Polystyrene Latex Microspheres aqueous suspension with de-ionized water.

In a typical procedure, 1.0 mL of PS bead aqueous solution (1.05g/mL) was transferred to a glass vial to 9 mL of water and mixed by sonication. The 1:10 solution was used to produce PS bead solutions at 1:20 and 1:40 concentrations. Each solution underwent sonication prior to validation experiments to avoid sedimentations of the spheres.

4.1.2. Preparation of Breast Cancer Cells

In this study, the human breast MCF-7 and MDA-MB-231 (1.401 and 1.399 refractive index respectively[160]) cell lines were selected for their identification by Raman spectroscopy. These cell lines have been used in prior in vitro RS experiments from our group,[43,45,46,51] yielding measurable radiation response signatures. In addition, the main biochemical constituents that contribute to their Raman vibrational pattern are well-established in the literature from a variety of studies.[161–164]

MCF-7 cells were grown in Dulbecco's Modified Eagle's Medium (DMEM) and MDA-MB-231 in Eagle's Minimal Essential Medium (EMEM). Both media were supplemented with 10% ($^{v}/_{v}$) fetal bovine serum (FBS) and 1% penicillin-streptomycin and kept at in a humidified atmosphere of 5% CO_2 in an incubator. Media was exchanged every two days, and cells were sub-cultured at 80% confluency. Cells were harvested with trypsin, resuspended in media (PBS buffer, DMEM, or EMEM depending on cell line experiment), then transferred to a 15 mL sterilized centrifuge tube and placed in an ice-filled cooler. Cell culture took place in the Facility of Biomolecular Sample Preparation at the University of Victoria.

After each cell collection, the concentration of cells in solution (stock solution) was around $2.0x10^{-6}$ - 8.0×10^{-6} per 5 mL collected. The stock solution was diluted using PBS buffer, DMEM, or EMEM (cell media) to obtain solutions at different concentrations. In a typical procedure, cells were prepared and used as follows:

Stock solution containing approximately $1.0x10^{-6}$ cells were transferred to a 1.5 mL Eppendorf tube (Stock tube). Dilutions 1:10 were made by collecting and transferring 10 µl of the stock solution into an Eppendorf tube to 900 µL of cell media, followed by gentle

mechanical mixing of 100 rpm, obtaining a sample with a cell count of $10x10^{-3}$ per milliliter. The procedure was repeated until obtaining a final concentration of 100 cells per milliliter.

The diluted samples were immediately placed in the iced cooler and subjected to mechanical mixing at 100 rpm prior to validation experiments. The samples were used within 6 hours of being collected.

4.2. Optical fiber aligner

A proper alignment of the fibers and the center of the flow channel of the microfluidic platforms is necessary to achieve stable optical trapping.

A translatable stage was developed for holding and controlling the different elements of the platform to allow precise adjustment of the fibers. The holder consists of a metal base that accommodates two translational stages with fiber holders attached to them. In-house aluminum fiber holders allocate the fibers in the translational stages. The capillary and microchip were mounted on the central stage support and could be aligned relative to the trapping fibers in the Y plane. Adjustment screws were used for shifting the fibers in the X and Z planes to align the fiber cores against the flat walls of the capillary to ensure proper field intensity distribution. Section 3.1 describes in detailed the fabrication steps and components of the Raman cytometer.

Before each experiment, an alignment protocol was performed involving the use of an IR viewer and the activation of the optical fibers to produce a streamline of PS beads within the capillary.

4.3. Fused Silica Capillary platform

Initial tests were carried out in a flow cytometer prototype with a fused silica capillary as the central component. Efforts focused on demonstrating the disparity in quality of spectra obtained from particles in motion at a constant flow compared to particles trapped with light, highlighting the importance of incorporating traps to keep the particles in position during the analysis. The methodology for obtaining Raman spectra from polystyrene spheres and cancer cells is shown in Section 4.5.

4.3.1. Materials

Square Flexible Fused Silica Capillary Tubing, Inner Diameter 50µm, Outer Diameter 363µm was purchased from Polymicro Technologies. PEEK Tubing 1/16" OD x .010" ID x 5ft was obtained from IDEX Health & Science LLC.

4.3.2. Capillary Setup and Instrumentation

The capillary-based platform described previously in Section 3.1, allows the integration of a microfluidic system to a Raman spectroscopy microscope. A schematic of the arrangement can be seen in Figure 4.1, which illustrates the incorporation of two optical fibers connected to a diode laser for the optical trapping of particles within the capillary to facilitate the analysis by the spectroscopic method. The cytometer was placed on a Raman microscope stage perpendicular to the emitting Raman beam. The size of the base is suitable for the dimensions of a standard microscope stage.

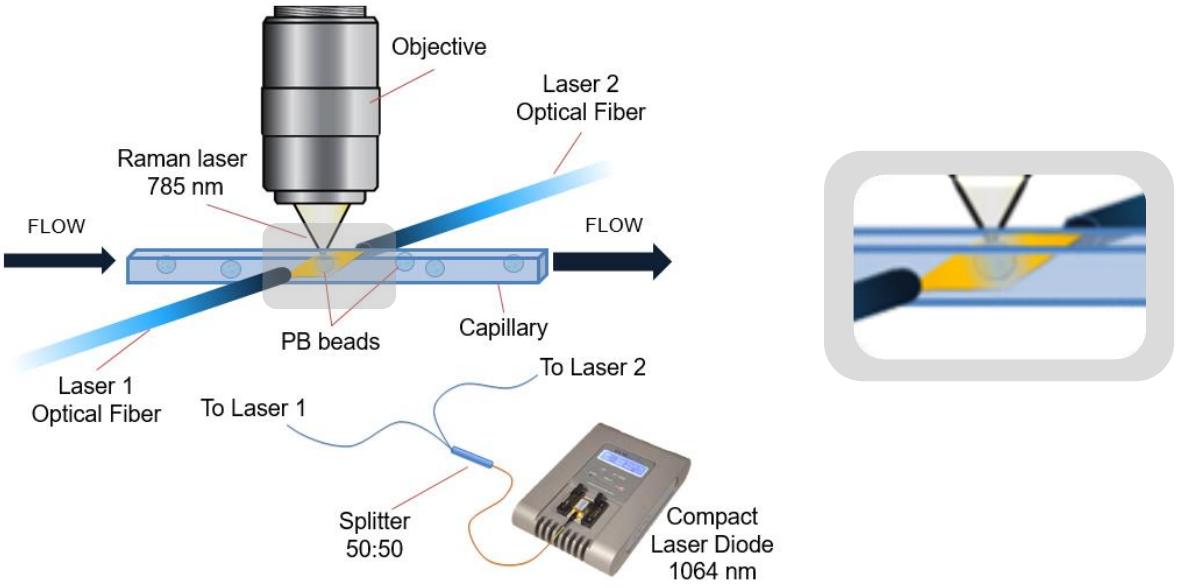

Figure 4.1 a) Schematic of the optical and microfluidic setup based on fused silica capillary; b) examination area.

The laser system consists of a laser diode (CLD) for power generation, operating at 1064 nm, connected to a 50:50 beam splitter to divide the power of the light path equally into two different single-mode fibers (arms). The single-mode fibers were set to face each other, creating a cross-section with the capillary on the same plane. Particles flow unidirectionally along a 330 x 330 µm fused silica capillary with an inner channel of 50 x 50 µm. An objective with a 785 nm Raman laser wavelength is perpendicular to the capillary and optical fibers, integrating the examination area. This configuration was used for all experimental studies Figure 4.2.

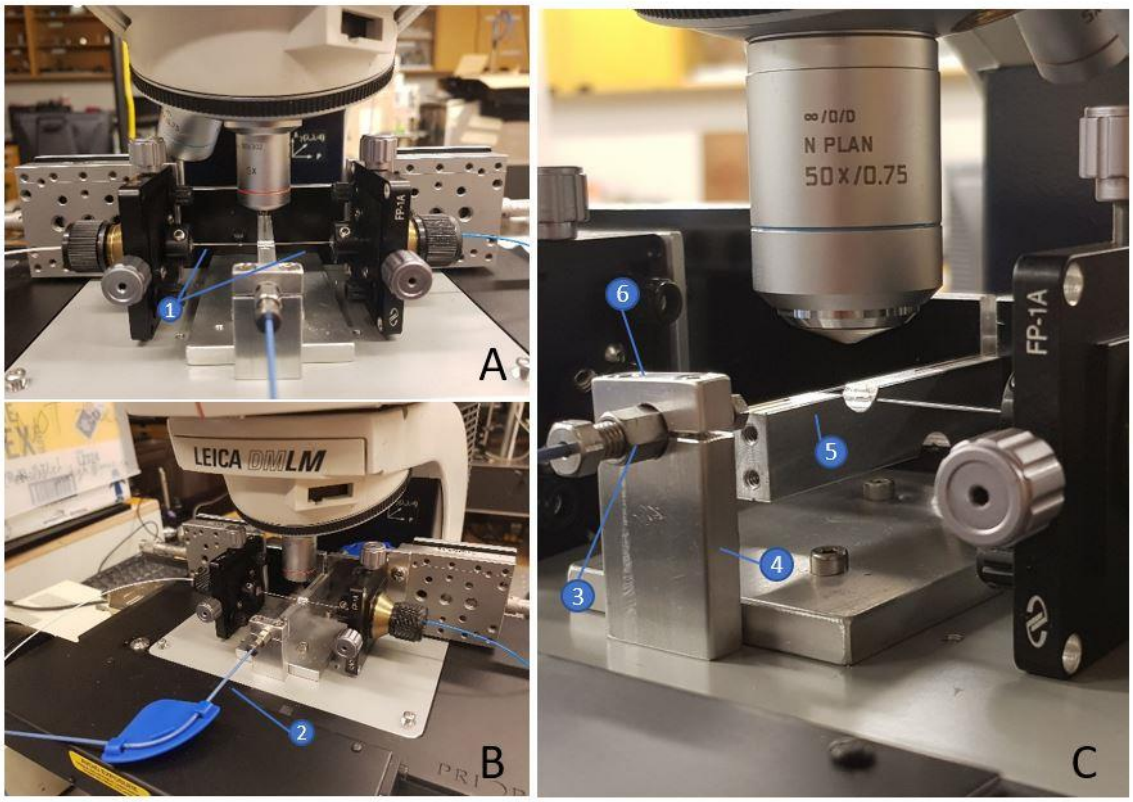

Figure 4.2 Front view of the capillary-based flow cytometer system on a microscope stage that shows two optical fibers (A.1) aligned to each other and perpendicular to the flow capillary. The capillary is connected to Polyetheretherketone (PEEK) (B.2) tubing using a standard reducing union (C.3) with a 0.5 mm ferrule (VICI Valco). The connector holders (C.4), placed at both ends of the capillary platform (C.5), hold the capillary into place and the separate holder top (C.6) serves as strain relief for the connectors while adjusting the capillary.

4.4. MgF_2-PDMS Microfluidic Chip

A MgF_2-PDMS microfluidic chip that integrates optical trapping and confocal Raman spectroscopy was fabricated for spectral analysis that supports oncological studies. An in-depth description of the microchip realization process is provided in Section 3.2.5.

A series of experiments performed using a capillary platform (described in sections 4.5 and 4.5.2), laid the foundation for developing a microchip platform with the potential of

further housing functionalities. Efforts focused on the process of creating a chip suitable for biological tests and determining its ability to identify trapped particles, namely polystyrene microspheres, and breast cancer cell lines in solution.

4.4.1. Materials

Sylgard 184 Silicone Elastomer kit (Polydimethylsiloxane - PDMS) with curing agent was used with a 10:1 ratio and obtained from Krayden Incorporated. Permanent Epoxy Resist SU-8 2075 and SU-8 Developer were purchased from MicroChem Corporation Silicon wafers (76.2 mm, P-type, Boron) were purchased from Silicon Materials Inc.

MgF_2 disk (5 mm thick) was obtained from Janos Technology Inc., and MgF_2 slides MgF_2 coverslip window (170 µm thick, 25 mm diameter) were obtained from Global Optics UK Ltd. PolyGone™ 505, silicon depolymerizer, was ordered from RPM Technology.

4.4.2. Microchip setup and Instrumentation

The microfluidics platform here described has an approximate dimension of 40 x 50 mm with a central flow channel and two fiber ports to incorporate a double-beam optical trap in a similar configuration as described in Figure 3.3. Unlike a capillary, the microfluidic chip is a three-layer device made up of a Raman optical grade MgF_2 base, a PDMS mid-layer (details in Section 5.2.1), and a second Raman optical grade MgF_2 window (Figure 4.3)

Photo- and soft lithography were selected for the creation of microchannels. These fabrication techniques allowed the making of polymer walls structures, open

microchannels without a planar bottom face. Two MgF_2 windows sandwich the polymer and create full channels with clear top and bottom faces and PDMS walls.

The fabrication of the microfluidic chip and the ultra-thick photoresist mold for PDMS molding is described in Section 3.2.5.

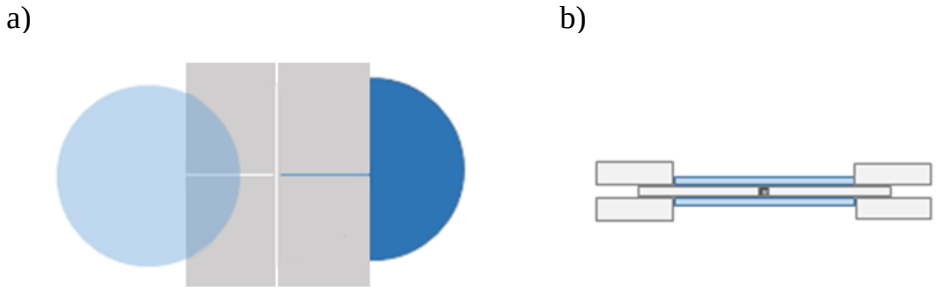

Figure 4.3 (a) Top-view scheme for a PDMS/MgF_2 chip consisting of a PMDS layer confined between 170 µm thick MgF_2 windows; (b) Side-view scheme of the same microchip with the addition of four PDMS blocks to assist the sealing of the fluidic system.

The microchip design is based on a cross-section configuration with a central channel for the flow of particles and lateral channels perpendicular to the flow chamber to position optical fibers, allowing a proper alignment of the fiber cores.

A PDMS separation barrier exists between the flow and fiber channels to protect the fiber ends from the solution and prevent contamination and leakage of hazardous fluids.

A series of chips with different gap-to-flow channel ratios were manufactured to study the influence of the fiber-to-fiber distance for the trapping of biological particles, in combination with different flow channel dimensions to determine the smallest channel width capable of avoiding PDMS contributions during Raman examination.

The chip was placed orthogonal to the Raman microscope objective on a bottomless aluminum platform incorporated into the previously described aligner stage. A confocal

Raman spectrometer (Renishaw InVia Raman Microscope) was used with a 785 nm diode laser. A schematic of the experimental arrangement can be seen in Figure 4.4

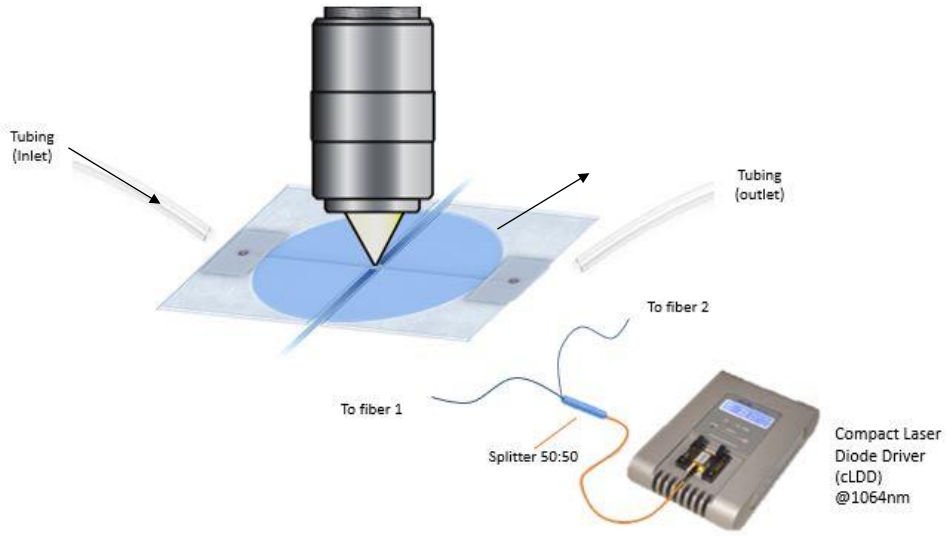

Figure 4.4 Schematic of the optical and microfluidic chip setup. As indicated by the direction of the arrow a sample enters the chip via tubing and flows to the right, exiting to a reservoir.

The fluid interconnection holes of the chip were coupled to tubing using standard connectors to link the platform with a syringe pump system. The system can be cleaned easily between measurements to avoid cross-contamination between samples, while the MgF_2 can be recovered by immersing the chip in a commercial solvent, Polygone 505 (RMP Technology, USA), for 24 hours.

4.5. Raman measurements

All Raman acquisitions were performed using a Renishaw inVia Raman Microscope (Section 3.3.2) coupled to a continues diode laser operating at 785 nm. For all PM studies, either a 50x (NA=0.75) or a 100x (NA=0.9) dry objective were used, as the laser volume in these set-up (~2 × 5 × 10 μm) allows for analysis of the contributions at the single cell

level. A 600 l/mm (lines per millimeter) diffraction grating was used for the study of the spectral window of 380–2589 cm^{-1}, while a 1200 l/mm covered a spectral range of 474–1620 cm^{-1}. All spectrometer components and spectral acquisition parameters were controlled by WiRE version 3.0 software package (Renishaw).

Before an experiment session, silicon wafer spectra with a strong peak at 520.00 ± 0.50 cm^{-1} was used for calibration of the spectrometer. Background spectra of the microfluidic systems were obtained before every set of experiments to detect variations coming from impurities in the capillary substrate or sample media. Additionally, background spectra for PS beads and cancer cells (MCF-7, and MDA-MB-231) were acquired and presented in Section 5.2.3

4.5.1. Polystyrene bead trapping experiment

PS beads were used to determine the efficiency of the trapping system and the capacity of the Raman spectrometer to identify particles within a microchannel prior to the loading of human cancer cells.

4.5.1.1. Experimental Parameters for the Capillary Platform

Solutions of varying concentrations (40:1, 20:1, 10:1; Section 4.1.1) were injected into the fused silica capillary and underwent optical trapping forces. Experiments consisted of identifying the ideal combination of microspheres per minute circulating in the examination area and the power needed to trap them.

A syringe pump was used for injecting the PS bead solutions into the capillary at flow rates ranging from 0.01 to 0.6 μL/min.

A glass syringe was selected in order to undergo the pressure generated from the reduced diameter of the system. The syringe of volume 1000 μL was mounted on the syringe pump

and connected to the capillary via 1/16th-inch (OD) 0.25 mm (ID) PEEK tubing (VICI Valco Instruments).

Initial decision-making regarding adequate flow rate was based on finding beads as regularly as possible in the examination area of the capillary while maintaining a reasonable distance between them.

Optical fiber connected to a diode laser operating at 1064 nm was introduced for the trapping of particles. Once a constant flow rate of the PS beads-PBS solution was achieved, a CLD was used to modulate the trapping current and power.

The optical traps were activated when a sphere was detected approaching the examination area. When the laser was in operation, the beads inside the capillary were subject to optical forces to slow down or stop their motion through the capillary. The movement of the microspheres along the capillary was tracked by confocal microscopy, while the fiber trap was manually operated via the CLD interface.

The optical power emerging from each fiber was studied and adjusted to ensure the trapping using the lowest effective power. Once trapped, the bead is ready to be analyzed by a Raman laser, orthogonal to the optical trapping beams.

PBS solution was injected at a constant injection rate of 15 μL/min to purge the system between different PS bead concentrations while deionized water was injected at a constant injection rate of 15 μL/min in order to reuse the system for future experiments.

Once identified the appropriate concentration of spheres and the minimum necessary force exerted by the optical traps to hold them in place, entrapment tests were carried out on the microchip-based system.

4.5.1.2. Experimental Parameters for the Microfluidic chip platform

After finding the appropriate concentration of beads in solution, this information was used as the starting point for the experiments carried out later on in the microchip.

The central channel became the subject of tests to determine its ability to host biological experiments. Millipore water was injected at increasing flow rates to determine the maximum pressure that the chip structure could withhold while maintaining functionality. A proper bonding technique is crucial to prevent leakage of biological material and maintain control of the microchip conditions; therefore, ensuring the perfect assembly of the components of the chip is fundamental.

A syringe pump with a 1000 μL glass syringe was mounted and connected to the system via a 1/16-inch (OD) 0.75 mm (ID) polymer tubing for the injection of solutions into the chip.

Once knowing the information pertinent to the concentration and flow rate in which the beads can be adequately visualized, they became subjected to optical trapping at varying optical power to find the lowest power in which the PS beads become trapped.

Optical fibers connected to a diode laser operating at 1064 nm were introduced for the trapping of particles. The optical power emerging from each fiber was studied and adjusted. Once trapped, the bead is ready to be analyzed by a Raman laser, orthogonal to the optical trapping beams. Once the platforms and their ability to trap and analyze beads had been tested, the spheres were replaced by two cancer cell lines to study the devices further.

4.5.2. Experimental parameters for the cell experiment

The capillary system underwent a second round of biological studies following the initial validation studies concerning the injection of poly beads to determine an appropriate flow

rate and trapping force ratio before their interrogation with Raman scattering. The new studies involved the injection into the system of two different cancer cell lines: MCF-7 and MDA-MB-231. The cell lines endured similar tests to those performed with PS bead, yet new challenges were inherent to the cell lines involved.

Similar to the tests performed in section 4.5.1, background spectra of the device setup were taken before every set of experiments to avoid variations due to substrate contamination.

After harvesting, described in Section 4.1.2, the cells of both cell lines were placed in a cooler and used within 4-6 hours of collection.

4.5.2.1. Cell Experiments with the Capillary-based platform

Cell solutions of different concentrations were brought to a 1 mL suspension and injected into the fused silica capillary to find the optimum combination of cells per minute and the power needed to trap them. Detailed sample preparation is described in Section 4.1.2.

A syringe pump was used to inject the PS bead solutions into the capillary at flow rates between 0.01 to 0.6 μL/min. A glass syringe of volume 1000 μL was mounted on the syringe pump and connected to the capillary via 1/16th-inch (OD) 0.25 mm (ID) PEEK tubing (VICI Valco Instruments).

The optical traps operating at 1064 nm were activated to stop the flow of cells along the capillary. The optical power emerging from each fiber was studied and adjusted to ensure the trapping using the lowest power possible to minimize optical damage.

Failed attempts to visualize the cancer cells within the capillary were followed by the collection of the waste container at the other end of the capillary. The content was immediately transferred to a centrifuge (Spectrum Laboratories) and was subject to 30

seconds at 120 rpm. The result was a cell pellet which supernatant was replaced by DI water and analyzed using RS at 785 nm on a MgF_2 slide.

4.5.2.2. Cell Experiments with the Microfluidic chip platform

After demonstrating the ability to trap spherical polystyrene beads and using Raman spectroscopy for examination inside the MgF_2-PDMS chip, the platform was tested to observe and detect cells in its flow channel.

Cell media was introduced into the channel prior to the injection of cell solution in the microfluidic device. Solutions containing varying cell concentrations were prepared according to the protocol described in section 4.1.2. Solutions were kept in an ice cooler and periodically mixed to avoid sedimentations.

The stock cells were brought to a 1 mL suspension for the chip experiment. Aliquots de 50 µL were injected directly into the inlet hole of the microchip using a micropipette, and the cells were analyzed by RS.

Following cell identification, the samples were injected into the chip to find the optimum combination of cells per minute and the power needed to trap them. A syringe pump with a 1000 µL glass syringe was mounted and connected to the system for injecting cell solutions at controlled flow rates. The tubing used was a 1/16-inch (OD) 0.75 mm (ID) polymer tubing.

The optical trap was activated when a cell was detected approaching the examination area. The movement of the cells along the capillary was tracked by confocal microscopy, while the fiber trap was manually operated via the CLD interface.

The optical power emerging from each fiber was studied and adjusted to ensure the trapping using the lowest power possible to minimize optical damage. Once trapped, the cell was ready to be analyzed by the Raman laser.

Raman spectra of both cancer cell lines were collected within the spectral acquisition window of 474 cm^{-1} to 1819 cm^{-1}.

After each cell line experiment the chip was placed in 70% alcohol for disinfection. The MgF_2 was recovered, and a new chip was used to avoid cross-contamination between cell lines.

4.6. Raman spectra processing

The spectra acquisition and processing depend on the intended data usage. However, the spectral processing of intensity vs. relative wavenumber followed a general line of processing involving cosmic ray removal, smoothing/denoising, background removal, and normalization.

Spectra collection followed by the identification and manual removal of spurious signals. The spectra showing saturation of the detector by cosmic rays, which are sharp spikes in the spectra not related to the sample (generated by artificial light, a vibration of the instruments, or unavoidable high energy particles coming from out of space hitting the detector), were corrected or discarded for further analysis.

Smoothing was performed to eliminate irrelevant, random, and systematic variations in the data, e.g., signal intensity variations linked to laser intensity. As the noise is random, it changes with a higher frequency than the Raman signals. As the band shape of the spectra is important, a moving polynomial (Savitsky-Golay) of small order (2nd derivate) was fitted through 7 data points (smoothing window size). The size window was selected

following the data processing protocol introduced in a previous work from our research group.[67]

The spectra were subsequently processed for background removal. The use of a Savitsky-Golay filter preserves the Raman band's shape better than other methods, and the different smoothing window sizes determine the resultant width of the bands as they increase relative to the data points in the window. A first-order polynomial is fitted in 7 points size moving window, which means the creation of a new data point value is the polynomial derivate on that point. Possible background sources include biological fluorescence from the sample and instrument-specific background such as the objective lens.

Before each experiment, background spectra were obtained from different points in the microchannel; this data was used to determine the contributions from the background and remove the source of variability. If a suitable background spectrum of the platform's substrate was available, this was subtracted from the sample's spectral signal before the Savitsky-Golay filter treatment. When necessary, a peak alignment was performed to correct an offset from the Si calibration wavenumber.

Data normalization was performed with respect to the total area under the baseline following background correction. This method takes into account the differences in absolute peak intensity among spectra from fluctuations in the laser output power and eliminates systematic differences among measurements, such as focusing depth and sample volume.

The software used for data processing includes Renishaw's WiRE software version 4.3, Origin lab 2021b, and Excel (Microsoft).

5. Results and discussion

5.1. Capillary-based Microfluidic Platform

Prior to each experiment, an alignment protocol was performed to achieve the proper alignment of the optical fiber cores starting with the manual adjustment of the mechanical component of the stage that holds the fibers in place. Once the fibers appear aligned (Figure 5.1c), the alignment is tested using a commercial infrared viewer (IR viewer) for validating the alignment visually.

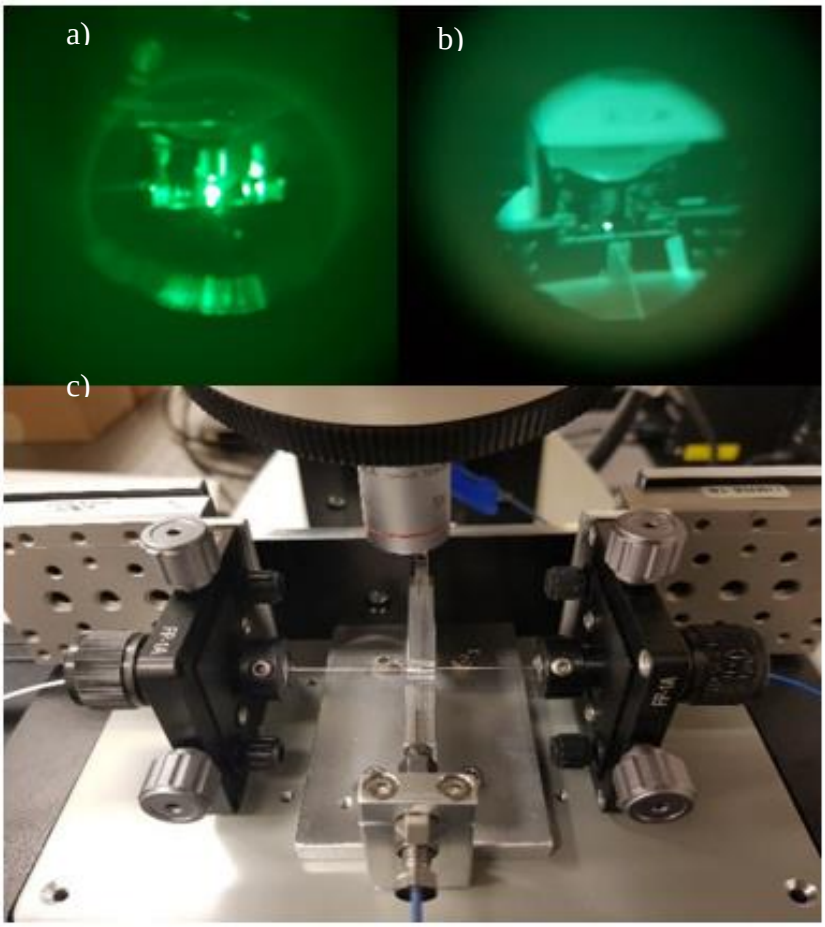

Figure 5.1 Top: Activated Optical fibers viewed through the lens of an IR-viewer showing misaligned (a) and adequately aligned fiber cores (b). Bottom: Top view of the capillary system with perpendicular optical fibers in alignment with each other.

IR-viewers help to observe direct and indirect radiation of IR lasers, light-emitting diodes (LEDs), dyes, and other IR sources. The viewer detects randomly scattered light from the laser beam and creates a visible image of the beam. Figure 5.1 shows photographs taken through the ocular lens (eyepiece) of a commercial IR viewer.

The laser used for optical trapping operating at 1064 nm produces a beam invisible to the naked eye; therefore, the IR viewer allows to follow the beam path and check the beam position.

Figure 5.1a shows light coming from the fiber-capillary cross-section, reflected by the setup materials in all directions, which means a misalignment of the fiber cores that results in loss of light from the system and produces a corrupted trapping effect while creating a potential health hazard. On the other hand, Figure 5.1b shows a proper fiber core alignment where light concentrates between the fibers within the capillary.

A PS bead was additionally used for calibration and alignment of the trapping system. An adequately aligned dual-beam trap should exert a balanced force that directs the beads to the capillary center; therefore, an off-centre bead flow means a power imbalance between fibers. These steps represented the basis of the calibration process that informed the fibers' alignment conditions and problems concerning the fluidic component to discard any possible leakage or obstruction.

Only after the trap resembled Figure 5.1b, an IR viewer was used to guarantee core alignment and the microfluidic spheres were pushed into a single stream at the center of the capillary could the experiments continue.

5.1.1. Capillary-Based Platform calibration

The capillary-based microfluidic device was mounted on the microscope as shown in Figure 5.2 in the configuration described in Section 4.3.2.

Background spectra of the capillary were taken before and after the PBS solution or cell media injection in the capillary channel. Figure 5.2a allows distinguishing the interior of the capillary with a diameter of 50x50 µm.

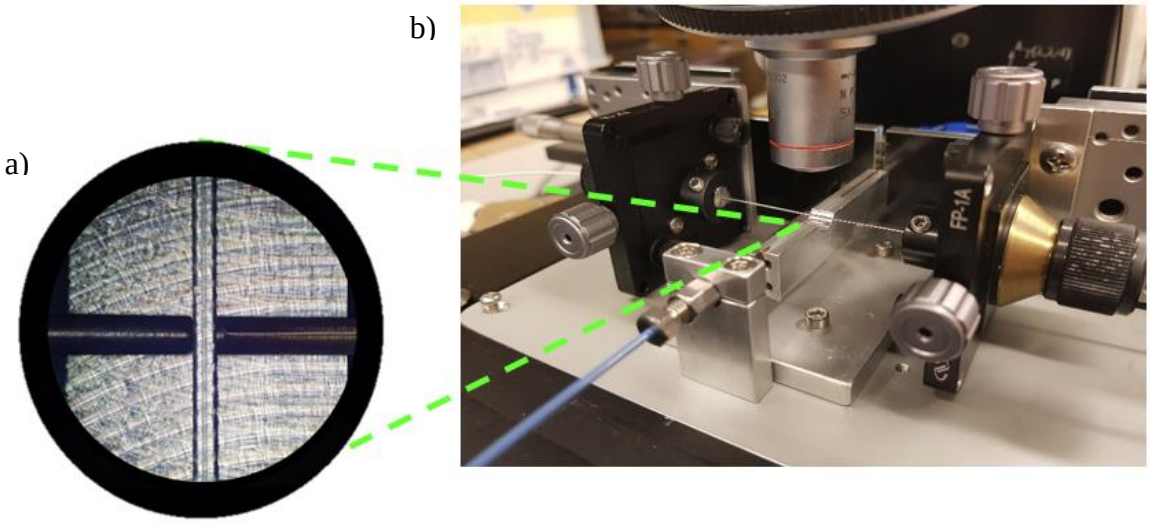

Figure 5.2 Microfluidic system in microscope stage. 10x view of the examination area in the cross-section formed by the optical fiber holders and the capillary.

The laser beam was focused on the center of the channel Figure 5.3. Each spectrum was collected at different depths and points of the examination area in the capillary 30 seconds per point in static mode, covering a spectral range of 380 to 2589 cm^{-1} with a Renishaw detector in a 600 $^{l}/_{mm}$ configuration. Both 50x and 100x objectives were used for platform validation. The measurements were averaged based on three accumulations under the same conditions.

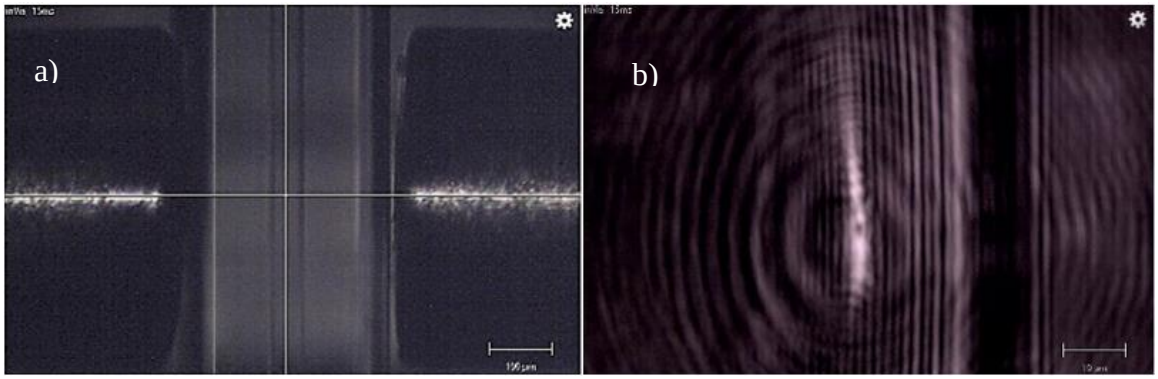

Figure 5.3 a) 50x view of inner channel of the capillary placed between two optical fiber ends (examination area) b) Raman beam spot focused in inner channel 100x view.

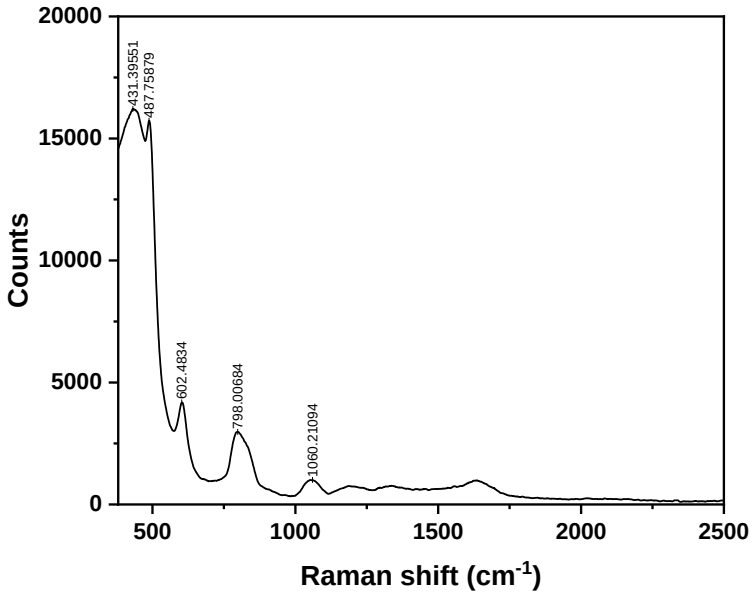

Figure 5.4. Raman spectrum of fused silica from the interior of the capillary channel measured using a 100x objective with a beam spot focused at 100% laser power for 30s and 3 accumulations.

Fused quartz manifests broad peaks determined mainly by SiO_2 vibrations (Figure 5.4). The most pronounced band at 445 cm^{-1} originates from oxygen atom vibrations with identical distortions of neighboring Si-O bonds, i.e., symmetric stretching vibrations. The peaks at 485 cm^{-1} and 600 cm^{-1} are associated with the breathing modes from defects in the silica lattice, the formation of 4-membered (4 oxygen atoms), and 3-membered (3 oxygen) rings, respectively[165].

5.1.2. Polystyrene beads trapping in the capillary-based platform

Polystyrene spheres were released at different concentrations and different flow rates. Figure 5.5 shows two of the concentrations used of PBS buffer – Poly beads solution mixture corresponding to 10:1 and 20:1. During testing 40:1 concentration was proven to be the adequate concentration and the one used for all experiments involving polystyrene beads. The decision was based on finding the ideal number of beads that would not obstruct the capillary entrance and allow a proper distance to catch a sphere individually without multiple spheres agglomerating in the optical trap simultaneously. The capillary holder provided high contrast for effectively visualizing the flowing beads in the system.

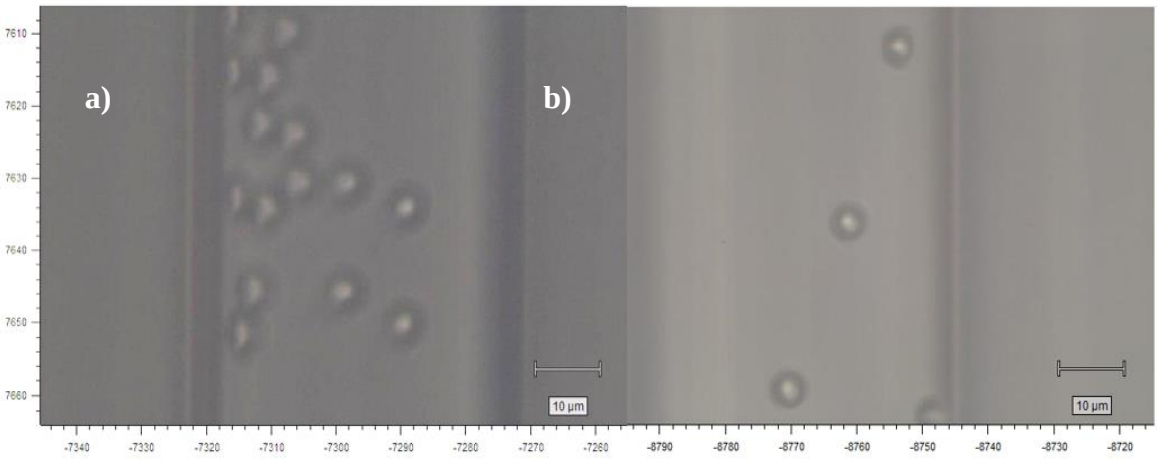

Figure 5.5 PBS buffer and Polystyrene bead solution at a mixture of (a) 10:1 and (b) 20:1 flowing in a fused silica capillary.

Different flow rates were tested to find a velocity that would place a sphere within the examination area constantly every 30 - 60 seconds and that the kinetic force present in the sphere would not offer enough opposition to the forces generated by the optical trap, which would cause the sphere to escape the trap without stopping.

To test the fiber based optical traps, the fibers were positioned on both sides of the examination area and were manually activated upon detection of a sphere entering the examination zone.

As depicted in Figure 5.6, the light beam from the fiber optics passes from one transparent medium to another before reaching the polystyrene sphere, causing it to change its direction due to refraction. Therefore, an ABCD matrix was used to calculate an accurate laser beam geometry. The formulas consider the refractive index of the fused silica capillary and bead fluid media to determine the rate of change of the laser beam direction. The calculations serve as a double purpose of verifying that the divergent beam spot is large enough and that contains enough force to stably trap large objects without reduced power densities due to distortion.

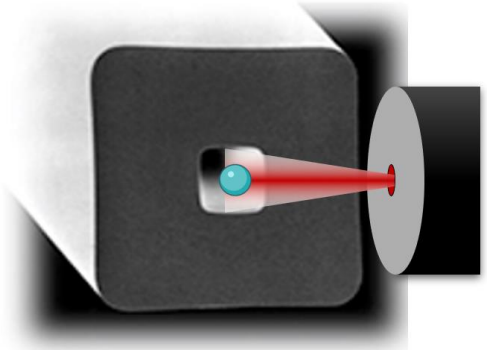

Figure 5.6 Diagram of a fused silica capillary cross-section. A laser beam exiting an optical fiber end face strikes a polystyrene bead traveling in the interior of the capillary. The laser light must pass through layers of air, fused quartz, and a liquid medium before exerting forces on the micron size bead.

ABCD matrices were used to calculate beam divergence (detailed calculations shown in Appendix A) under two conditions: i) optical fibers pressed against the capillary walls for a trap of 18 μm in diameter; and ii) optical fibers positioned at 20um μm away from the

capillary wall, yielding a 39.94 μm, which represents an increase in the beam spot size of ≈53.38%.

The optical fibers traps were tested at different power outputs to determine the minimum power needed to trap PS beads optically. The intensity of the laser emanating from each single-mode fiber was set to values from 20 mW to 90 mW

Table 5-1 shows the power settings available in the cLDD and the resulting output measured from each fiber arm. The output power showed a fluctuation of ±4 mW measured in increments of 10, while a power imbalance between fiber arms was limited to ±3 mW.

Table 5-1 Relation between power setting in cLDD and the magnitude of the beam output emanating from each fiber

Power settings	Fiber output (mW)	Current (mA)
20	-	-
30	150±4	584
40	200±4	720
50	250±4	907
60	300±4	1071
70	350±4	1237
80	400±4	1292
90	-	-

The ability of the trap to serially stop beads was tested by flowing PS bead solution in the capillary using an automated syringe pump. Initial decision-making regarding adequate flow rate was based on finding beads as regularly as possible in the examination area of the capillary.

The flow rates selected range between 0.01 to 0.59 μL/min, which allows maintaining a reasonable distance between beads and presents a reasonable settling time, referring to the

time elapsed between the initial velocity after injection to the time it reaches the proper flow value.

Polystyrene solution was flown in the capillary at increasing intervals of 0.2 µL/min against the trapping forces of the beams at a power range from 30 to 80mW. Any power setting below or above this range generated a system error on the cLDD.

Table 5-2 shows the results of the trapping experiment. The minimum power required for stopping a PS bead at a determined flow rate was marked with a plus (+) symbol while the failure of stopping a bead was noted with a minus (-) symbol. Considering these results, the flow rates that allowed the sphere to stop or slow its motion when the fiber optic was activated were used to establish a speed range.

Table 5-2 Dynamic flow of polystyrene beads in the central capillary channel subject to different cLDD power settings (mW).

Flow rate (µL/min)	30	40	50	60	70	80
0.01	+	+	+	+	+	+
0.09	+	+	+	+	+	+
0.27	-	+	+	+	+	+
0.35	-	-	+	+	+	+
0.41	-	-	-	+	+	+
0.49	-	-	-	-	+	+
0.59	-	-	-	-	-	+

In order to properly determine the fiber laser's lowest power output capable of successfully trapping a flowing PS bead, the experiment was performed in triplicate using a new fused silica capillary at each trial to rule out any contribution from the system or the fiber alignment process.

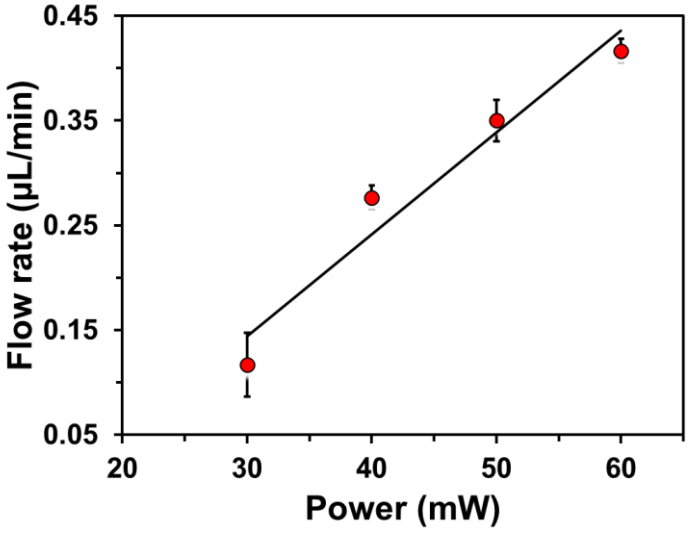

Figure 5.7 Plot indicating the trapping velocity tresholds as a function of laser power setting. Accuracy of the capilary system for the trapping of 5µm polystyryne beads.

Figure 5.7, shows the results of the trapping experiment to determine the lowest power output capable to perform successful trapping at desirable flow rates. The selected flow rate was 0.25µl/min and the laser power 50 mW.

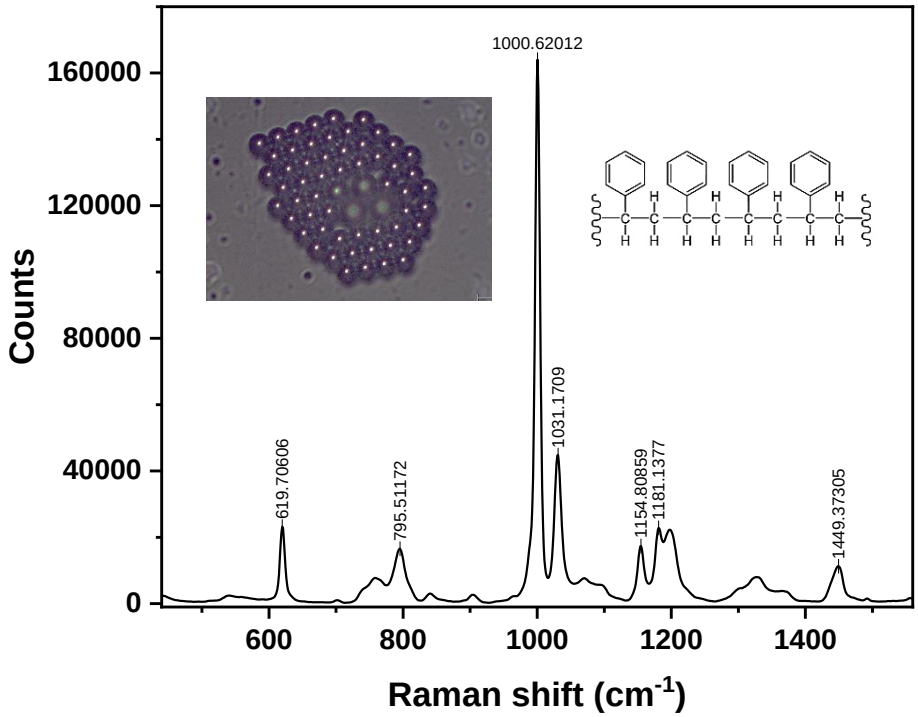

Figure 5.8 Polystyrene spectrum. PS bead solution was spread on a MgF_2 disk, and spectra were collected for a total of 30s in static mode centered at 1000 cm^{-1} and 3 accumulations.

The finding of a desirable sample concentration and an adequate flow rate was followed by Raman examination. Figure 5.8 shows a Raman spectrum used to identify the PS beads flowing through the capillary. In the polystyrene spectrum we see the high-frequency carbon-hydrogen (C-H) vibrations in two bands, at approximately 2900 cm^{-1} and 3050 cm^{-1}, corresponding to aliphatic and aromatic components of the molecule, and the vibrations of two carbon atoms linked by strong double bonds (C=C) at around 1600 cm^{-1}. However, the principal identifier is the breathing mode from the aromatic carbon ring that appears at 1000 cm^{-1} in polystyrene. The low-frequency carbon-carbon (C-C) vibrations are at around 800cm^{-1}.

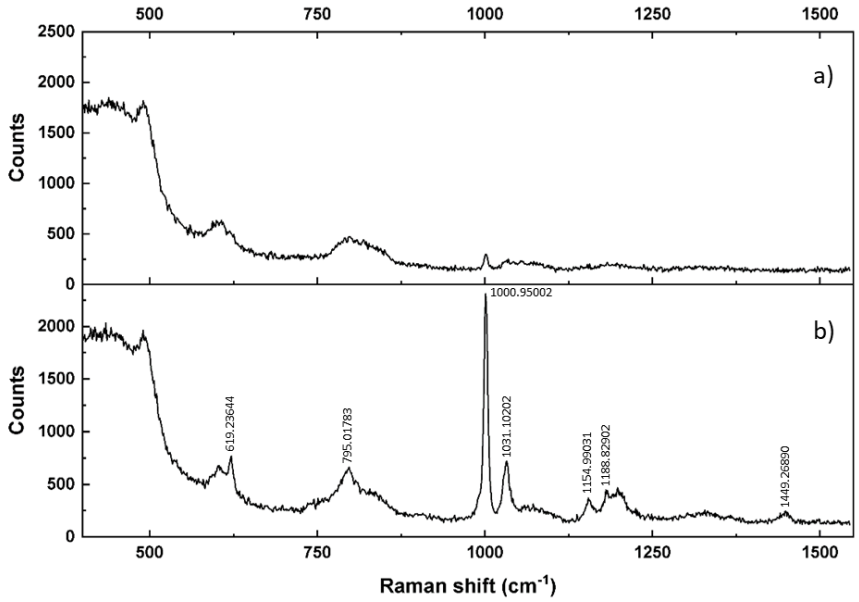

Figure 5.9 (a) Raw spectrum of flowing polystyrene bead acquired using Live video mode with a 100x objective, 100% power, 1s and 1 accumulation. (b) Raw spectrum of trapped polystyrene bead acquired using Static mode with a 100x objective, 100% power, 1s and 1 accumulation.

The intensity of the 1000 cm^{-1} benzene ring breathing mode was monitored as the bead was scanned under two different conditions to demonstrate the necessity of a trapping component in the system. A Bead solution was injected into the capillary without enabling

the 1064 nm laser diode; thus, the beads were analyzed without stopping; a 100x objective focused on the center of the channel at 100% power was employed in a Live mode that acquires a continuous snapshot of the sample every 1 second. On the other hand, a bead was stopped using a 1064 nm laser trap and its spectra analyzed in a Static mode configuration (Figure 5.11).

The spectra shown in Figure 5.9 contains fused silica background (Figure 5.4) and exhibits the 1001 cm^{-1} highly representative band of polystyrene. However, the spectra show an evident quality discrepancy between (a) and (b) regarding noise and signal intensity. Even though the Live mode function of the spectrometer can successfully identify the presence of beads crossing the Raman beam spot, the signal does not compare to the quality obtained using an external sample holder, and it is not sufficient to be used in this type of studies involving cells which spectrum is considerably more complicated.

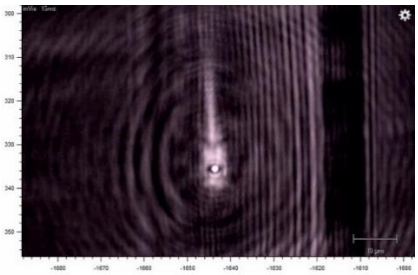

Figure 5.10 A 5 µm polystyrene sphere trapped by light force traps within the Raman beam spot.

Further acquisition of Raman spectra of 5 µm polystyrene spheres took place while the trapping lasers were enabled. (Figure 5.10). Spectra was collected with a 100x objective perpendicular to the fiber trap in static mode at a laser excitation power of 100% at 785nm, and an acquisition time of 10 s, and 3 accumulations. A representative result from these conditions is presented in Figure 5.11.

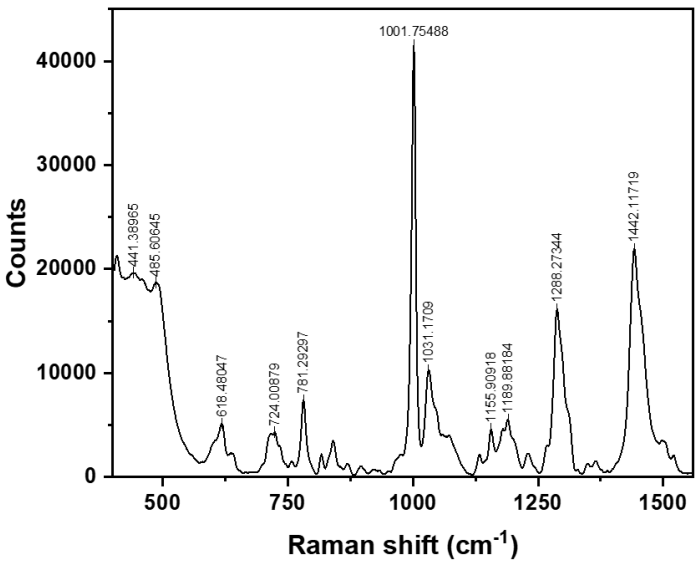

Figure 5.11 Raman spectrum of a single PS bead optically trapped in the fused silica capillary setup measured (100x objective, 10s, 3acc, and 100% laser power).

5.1.3. MCF-7 and MDA-MB-231 cancer cells trapping in the Capillary-based platform

Different cell samples were prepared following the procedure in Section 4.1.2 and introduced into the capillary using a syringe pump system. However, their visualization within the capillary proved to be challenging.

After allowing a few minutes for the system to settle, it was possible to sporadically visualize fast moving shadows along the capillary. Assuming they were cells traveling through the capillary, we attempted to detect cellular presence by Raman spectroscopy.

To verify the presence of cells in the capillary, spectra collection was carried out in live mode for an acquisition time of 1s from 900 cm^{-1} to 1200 cm^{-1} while focusing the laser beam on the center of the channel. Raman spectra were obtained with and without the enabling of the cLDD. The spectrometer recorded no evidence of cellular presence; therefore, we proceeded to recover the liquid sample collected in the waste vial connected to the other end of the capillary (outlet). The sample was subjected to 1500 rpm of

centrifuge force for 5 minutes. Subsequently, a pellet was collected, placed on a MgF_2 slide, and examined by RS, which revealed the presence of cells.

The speed at which the cells were injected into the capillary proved challenging to control. It is possible that cell conglomeration at the inlet of the internal reducing union produced the increase of system pressure that accelerated the cells. In addition, the use of polymer syringes may have caused the entry of air into the system, which was proven correct after the syringes were replaced by glass syringes, which drastically reduced the presence of air bubbles.

After a few minutes to allow the system to stabilize (5-10min), it was possible to visualize groups of cells attached to the capillary walls. The attachment was mainly observed when air bubbles stopped at the Raman examination area and caused the cells to be pushed towards the internal walls of the capillary

Figure 5.12 and Raman was obtained from the samples as shown in Figure 5.13. The Raman spectrum shows broad bands and little discernable features that could be directly assigned to the unique contributions from the cells.

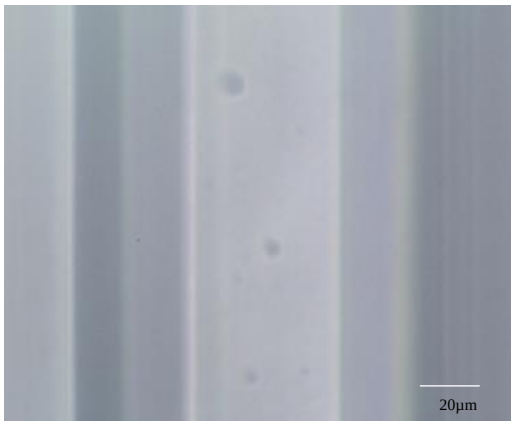

Figure 5.12 MCF-7 cell conglomerates attached to the internal wall (top) of a fused silica capillary (50x view)

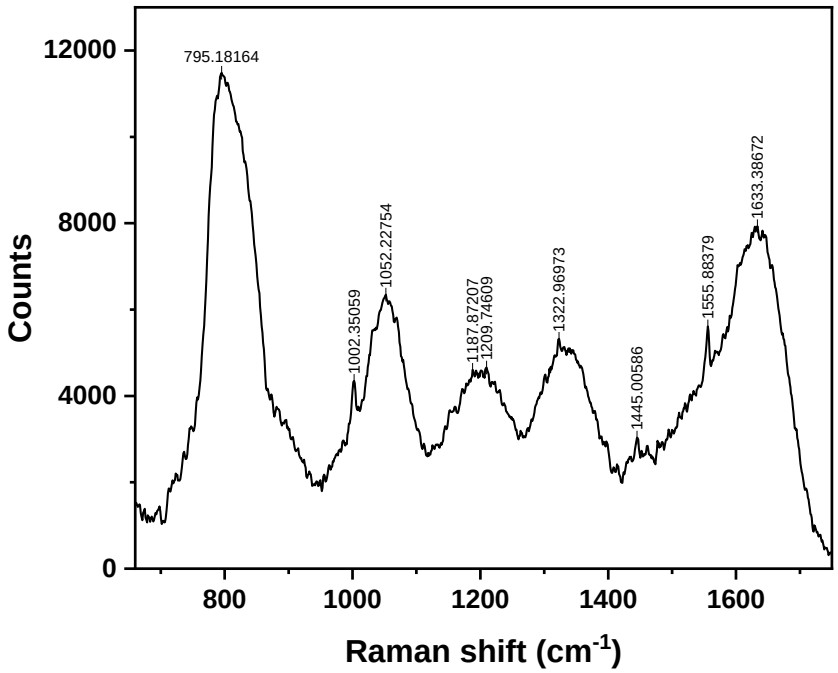

Figure 5.13 Raman spectrum of a an MCF-7 cell attached to the internal wall (top) of a fused silica capillary (100x objective, 10s, 3acc, and 100% laser power).

Although the cells were correctly introduced into the capillary, the similarity in refractive indices between the capillary (n=1.45) and MCF-7 cells (n=1.40) proved to hinder the visualization of cells in the capillary configuration.

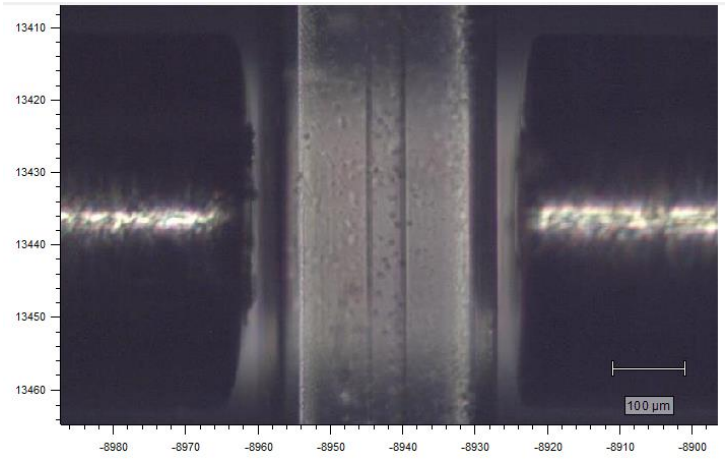

Figure 5.14 Post experimental conditions of the fused silica capillary with cell clusters visible along the internal capillary channel. This image has been subject to contrast increase to aid cell visualization.

Although fused silica is a common substrate used in microfluidics that provides an acceptable transparency for many spectroscopic applications, the presence of strong bands within the biological window of interest hides cellular information and, for this configuration, the similarity in refractive indices between the capillary (n=1.45) and MCF-7 cells (n=1.40) proved to hinder the visualization of cells inside the capillary. In order to continue the cell studies involving this capillary setup, it would be necessary to increase the contrast of the system.

A fused silica capillary, being a rigid structure, does not offer much flexibility to add functionalities or have greater control over the sample flow, which is one of the main reasons microfluidics is such a desirable technique to work with volumes of this nature.

5.2. Microfluidic chip platform

5.2.1. Details of the microfabrication protocol

Microfluidic chips, produced following the fabrication steps presented in section 3.2.5, were subjected to characterization studies.

5.2.1.1. Sealing

A microchip prototype was fabricated to test the sealing method showcased in Figure 3.15. This process involved the fabrication of several devices, each composed of 22 x 22 mm glass slides (1 mm thickness) used as the window and base of the chip and a PDMS mid-layer used to form the walls of the microchannels with a crossection configuration (Figure 3.13). The chips were subject to varying pressures generated from a syringe

pump. These tests consisted of injecting water into the system at different flow rates to determine the maximum pressure that the system could withstand.

The average maximum flow rate at which all the systems kept their structure intact and functional was 0.7µL/min. Above this flow value, the principal damage caused to the system was the rupture of the PDMS walls that separate the main flow channel and the lateral fiber channels. The rupture caused the release of the liquid on the chip, which prohibited the pressure tests from continuing (Figure 5.15).

The flow rate that the system can accommodate falls within the speed range used during the testing of the capillary system, showing that a microchip with the present configuration appears suitable for undergoing cell experiments without the risk of spilling biological material.

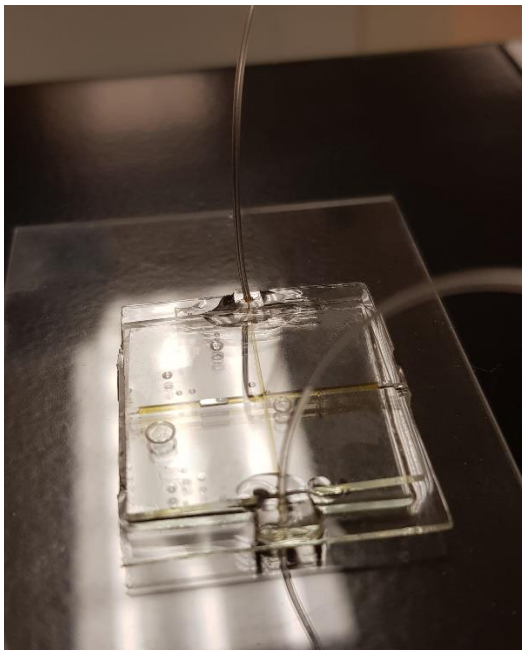

Figure 5.15 A glass-based microfluidic device for the testing of the sealing process. Orange died water is visible in the flow and fiber channels after rupturing of the channel separation walls due to flow rate pressure.

In addition, this experiment was repeated with MgF_2 windows and demonstrated the successful sealing created between the MgF_2 window and the PDMS chip structure that did not require special lasers to produce inlets outlets in the window.

Moreover, the sealing method does not represent a limitation in the manufacturing process of the chip. However, it was discovered that the fundamental limitation is the thickness of the walls that protect the optical fiber from the fluid.

5.2.1.2. Testing the detection of Raman scattering background from PDMS

Further studies were performed to identify the presence of PDMS background signal that could hinder the detection of biological originated bands. The findings from the microscopy and spectroscopy tests revealed the presence of PDMS in two presentations: i) the signal contributions arising from the PDMS walls within proximity of the Raman beam spot, and ii) a thin PDMS layer on the surface of the MgF_2 window (Figure 5.16).

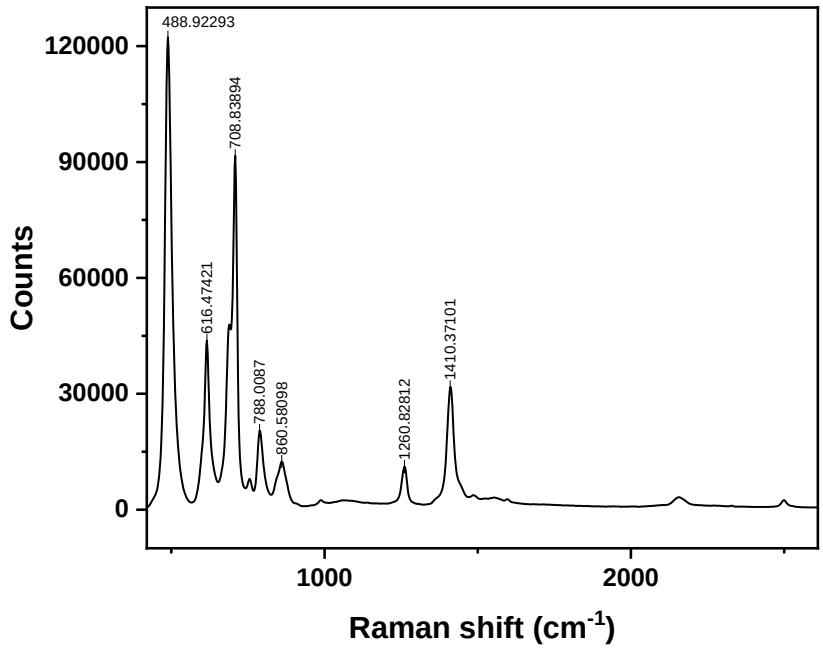

Figure 5.16 Raman spectrum obtained from the examination area of a MgF_2 microfluidic chip. The spectrum denotes the presence of characteristic Polydimethylsiloxane (PDMS) peaks.

Therefore, new microfluidic devices were created, and modifications to the microchip manufacturing process were implemented to reduce and potentially eliminate such contributions.

An open microfluidic device was fabricated to test the spectral wall influence based on channel width and establish the minimum flow channel dimensions to avoid or minimize excessive PDMS spectral contributions that could hinder the cell information.

The device consisted of a PDMS layer containing a variety of channel sizes. An SU-8 casting mold showed in Figure 5.17 was created by photolithography following the Ultrathick Fabrication Process and the PDMS layer following the steps depicted in Figure 3.14a and Figure 3.14b.

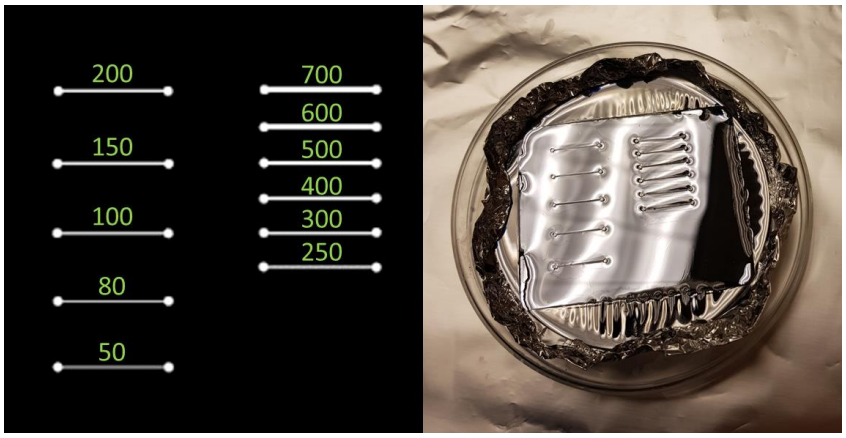

Figure 5.17 (Left) CAD photomask created for the testing of different channel width (50 -700 µm). (Right) Resultant open microfluidic chip created by soft lithography.

The cured PDMS was peeled off the mold and subsequently adhered to a MgF_2 slide and a selected channel was covered with a MgF_2 window before the acquisition of Raman spectra.

Consecutively, Raman spectra were acquired within each channel, using a 100x dry objective with a laser power of 100x and an acquisition time of 10s and 3 accumulations

which revealed critical information for selecting the appropriate channel width. The spectrum was taken at three different points of the channel. The three points were taken in the same X-plane and at the same focal point with respect to the bottom of the channel (mid-channel). The difference among the data acquisition points was their proximity to the PDMS wall. Figure 5.18 shows the channel segmentation highlighted in different colors. The sampling occurred at the midpoint of each segment.

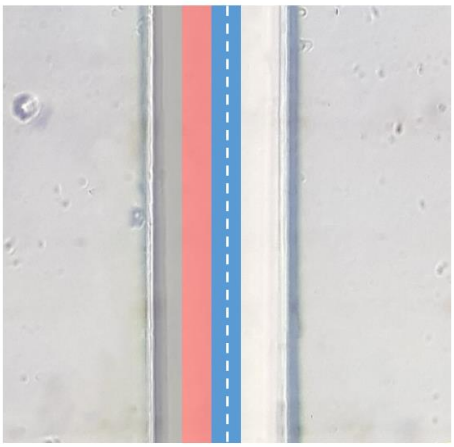

Figure 5.18 50x view of PDMS channel. Imaginary segmentation of a flow channel for the detection of substrate contributions; far left (grey), left (red), and middle (blue); white segmented line represents the center of the channel.

Figure 5.19 demonstrates the influence of PDMS walls in a 100 µm wide channel. As expected, the intensity of the PDMS contribution was inversely proportional to the distance of the focal point with respect to the channel wall. The blue line in the spectrum shows the Raman profile obtained at the center of the channel that shows a significant less intensity compared to the data obtained the closest to the wall.

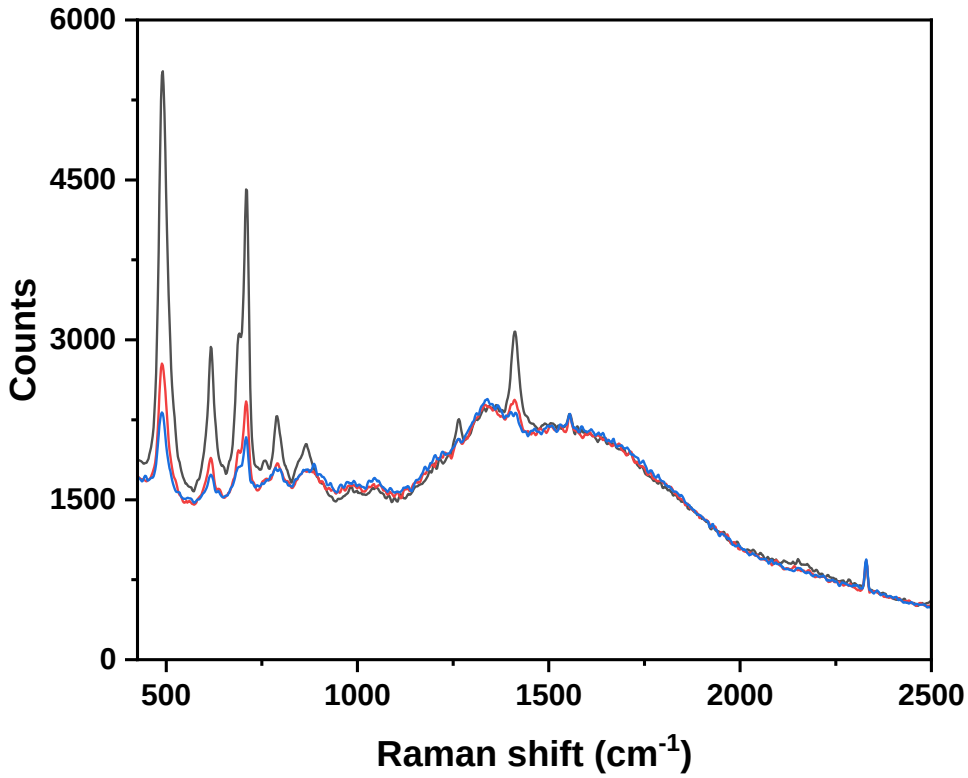

Figure 5.19 Raman spectra collected from a 100 µm flow channel at 3 different distances with respect to the center of the channel: far left (black), left (red), and middle (blue).

Figure 5.20 compares the spectrum of a MgF_2 window and the spectrum from the center point of a 200 µm channel with PDMS walls. The spectra were obtained using a 50x objective with a laser power of 50% and an acquisition time of 10 s and 3 accumulations. The channel spectrum (blue) contains characteristic PDMS peaks contributions. Regardless, the polymer contributions are minimal when using a 50x objective and are absent when using a 100x lens used for cell experiments. Therefore, the spectral analysis of the measurements performed in different channel widths determined that a 200 µm width channel is the minimum size necessary to avoid structural PDMS contributions.

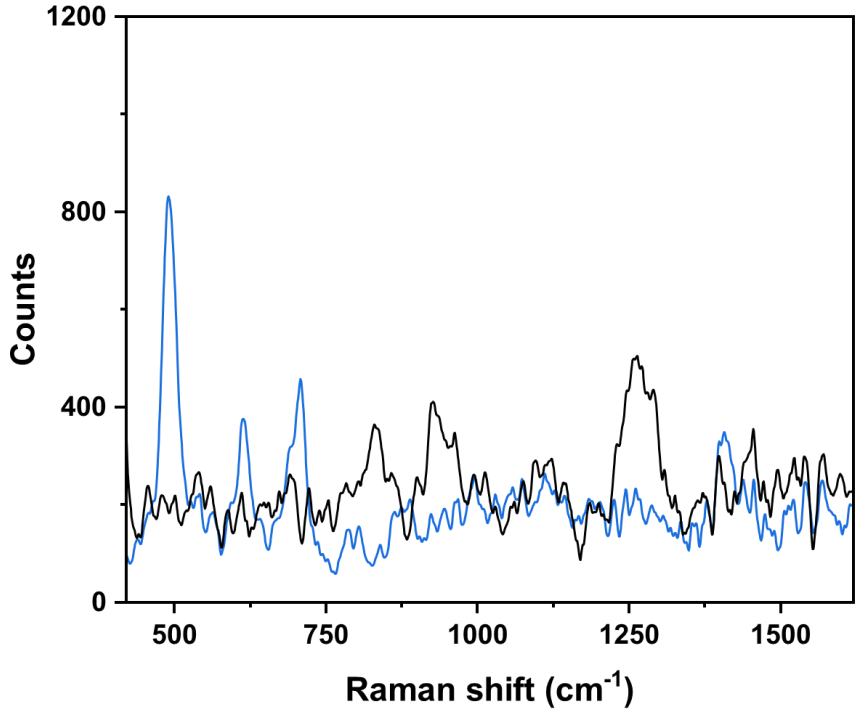

Figure 5.20 Comparison Raman spectra of a 200 µm flow channel obtained at the channel's center (blue) and a MgF_2 window (black) under the same acquisition conditions (50x, 50%, 10s and 3acc).

On the other hand, Figure 5.21 shows the contributions of the same 200 µm channel at three different spots of the channel compared to cured PDMS from the same platform and the spectrum of a MgF_2 window under the same spectral conditions. Showing the difference in relative Raman intensity arising from the three substrates.

Additionally, besides channel width, another major contributor to the chip's dimensions is the maximum separation allowed between optical fibers to perform successful trapping of particles. In the literature, there are examples of trapping systems employing a fiber separation gap between 85 and 330 µm mentioned in Section 1.4**.** Considering a 200 µm channel dimension, the area between the flow channel and the fiber channels that protects the ends of the fibers from the sample solution needs to be modified.

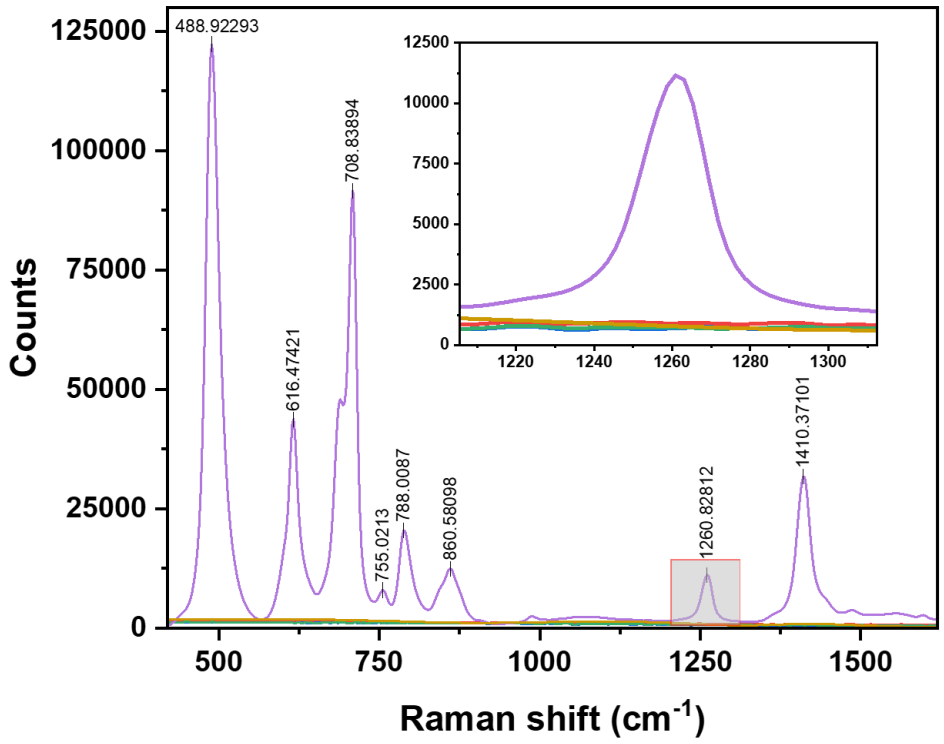

Figure 5.21 Raman spectra collected from a 200 µm flow channel at 3 different distances with respect to the center of the channel, far left (black), left (red), and middle (blue); compared to PDMS (purple) and MgF_2 (black) spectra obtained under the same acquisition conditions (100x, 100%, 10s and 3acc). Zoom in (inset) image of spectral contributions centered at 1260cm^{-1}.

A series of chips with different flow-to-fiber channel separations (50, 80, 100 µm) were manufactured to study the effect of fiber-to-fiber distance on the optical trap. These chips required the modification of the SU-8 molds by changing the width of the gap between the main flow channel and fiber channels. Flow channels created with soft lithography must be designed according to acceptable aspect ratios; otherwise, the channels may collapse after fabrication. Experimentally we determined a 15:1 (height: width) as the maximum feasible working dimension while producing an ultra-high SU-8 mold.

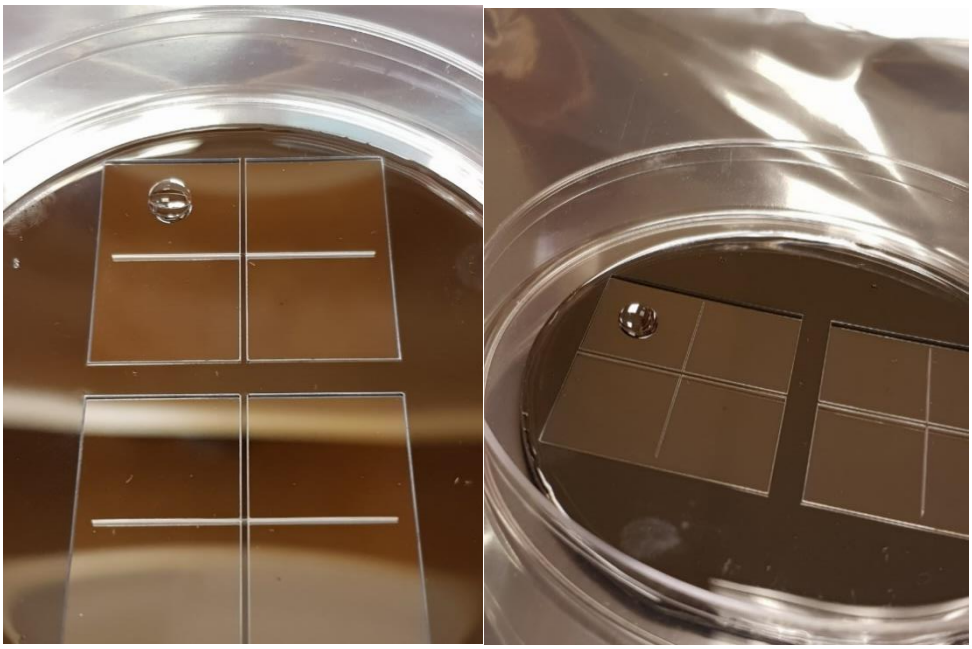

Figure 5.22 SU-8 mold after silanization treatment to increase substrate hydrophobicity.

Fiber gaps of 50 µm were readily discarded due to the fabrication difficulties, including the collapsing of the flow channel between the fiber channels or the wrinkling of the channels during photo development due to an incomplete, hard-baking process. In addition, some molds produced successfully served as single-use casting mold due to the channel detaching despite the silanization of the mold (Figure 5.22).

The creation of a new photomask (Figure 5.23) alleviated the fabrication problems. The new template consisted of a continuous fiber channel shared by the two possible chip devices photolithographed on each wafer. The new design avoided the presence of a SU-8 strip between each chip mold in the wafer. This SU-8 area was prone to wrinkling and lifting, causing the adjacent fiber channels from each chip to be pushed into and impact their respective flow channels.

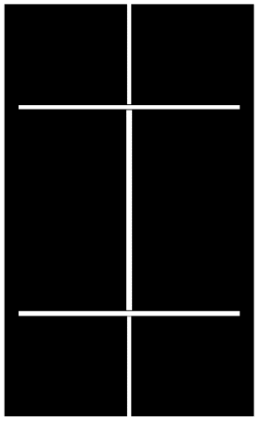

Figure 5.23 optimized CAD photomask created for chip fabrication.

PDMS was also observed when performing spectroscopic studies on sealed chips, which presence was detected at the bottom of the central flow channel (Figure 5.24). After pouring PDMS into the mold and placing the MgF_2 window on top of the examination area of the chip, uncured PDMS overflowed the walls of the mold and spread over the window.

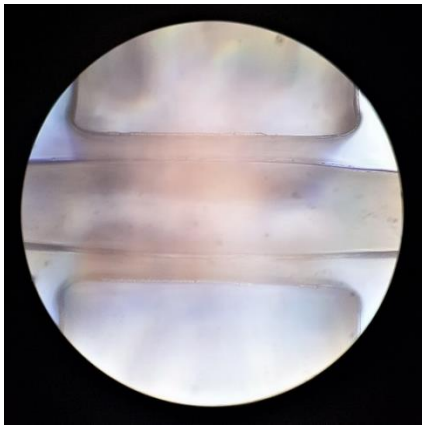

Figure 5.24 Microscope view of the examination area of a PDMS – MgF_2 chip. The presence of a polymer is visibly identified in both fiber and flow channels.

The elimination of PDMS was carried out through two approaches, post- and pre- chip sealing. Polygone™, a silicone sealant depolymerizer / emulsifier used for removing cured silicone and other sealants, was injected into the sealed chip for 5 minutes and then flushed with water. Figure 5.25 shows the center channel before and after solvent use.

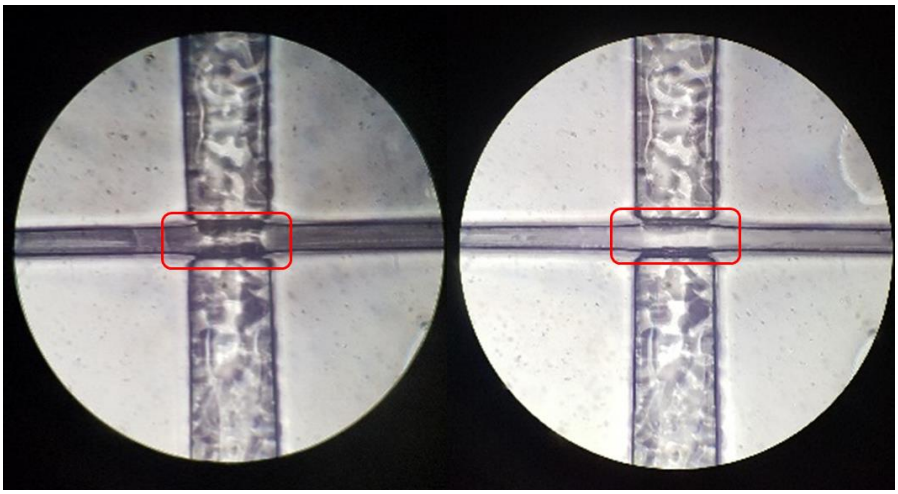

Figure 5.25 Examination area of a microfluidic chip before and after using a polymer solvent for the removal of PDMS at the bottom of the flowing channel.

The most suitable approach was to perform a soft-bake of 20 - 30 min at 60°C after pouring the PDMS into the mold. After this time, the window can be confidently placed over the examination area and returned to the oven for 2 h at 80 °C. This minor change stopped the spreading of PDMS under the window and allowed the creation of well-defined channels (Figure 5.26).

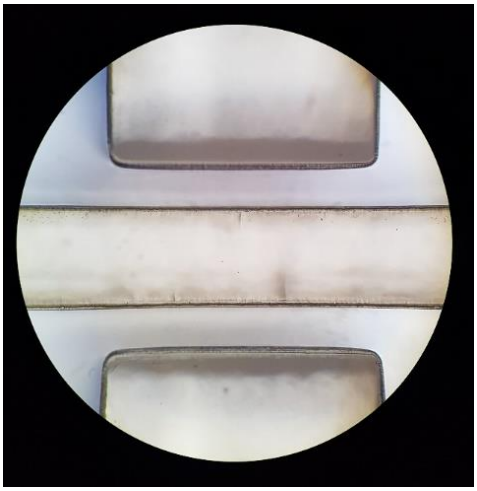

Figure 5.26 Microscope view of microchips examination area without the presence of PDMS at the flow channel's bottom.

After implementing the chip modifications detailed above, the last step for the chip creation consisted of sealing the devices with a MgF_2 window, following the process previously illustrated in Figure 3.15.

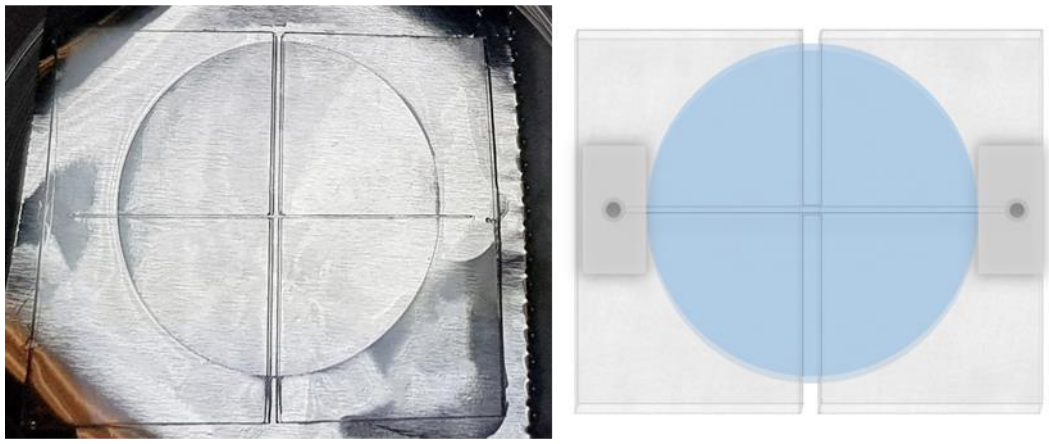

Figure 5.27 (a) Picture of a square PDMS layer attached to a MgF_2 circular coverslip. (b) Top-view diagram of a complete microfluidic chip. Figure shows the real dimensions of a microchip (length x width x height): PDMS layer, 40 x 40 x 0.7 mm (L x W x H); flow channel, 35 x 0.2 mm (L x W); PDMS cubes, 10 x 10 x 10 mm (L x W x H); MgF_2 base/window, 25 × 0.17 mm (L×W); fiber channel, 19.8 x 0.6 mm (L x W).

After peeling off the microchip's PDMS middle layer from the mold, we obtained a square casted PDMS piece of 40 x 40 mm and approximately 650 µm high attached to a MgF_2 coverslip that serves as the microchip's transparent base (Figure 5.27a). For the device's sealing, a second MgF_2 coverslip (window) was placed on top of the PDMS surface, directly above the base coverslip. Posteriorly, two PDMS cubes were punched into to create $^1/_{16}$" holes (inlet/outlet). The cubes were plasma bonded to the PDMS surface to cover the remaining exposed flow channel with the inlets aligned to the channel ends. Uncured PDMS was used as glue to maintain the cubes' edges from lifting and followed a short baking process.

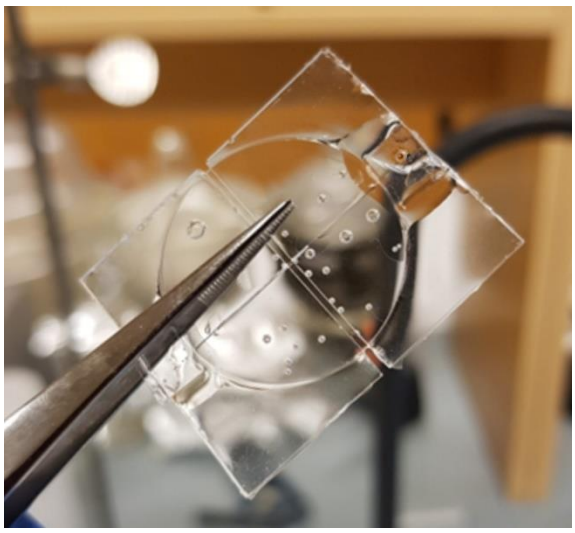

Figure 5.28 Picture of a completed microfluidic device

Figure 5.28, show a terminated microfluidic chip composed by two MgF_2 windows. The chip was connected to a syringe pump by directly fitting the tubing into the PDMS inlet/outlet.

5.2.1.3. Calibration of the microfluidic chip platform

The chip's background spectra were collected before and after the injection of samples to prevent spectral contributions from impurities within the microchannel, such as PDMS presence, contamination on the surface of the optical window, or of the sample media.

The chip was positioned under the microscope, as seen in Figure 5.29, using an acrylic holder to assist with spectra acquisition; the holder provided free space under the central part of the chip to avoid background contributions.

The spectrum of MgF_2 was collected using an 100x objective (NA=0.85) to focus a 785 nm Raman laser spot at the bottom of the chip's channel for a 30 second collection time with three accumulations and a 1200 l/mm grating configuration, as shown Figure 5.30.

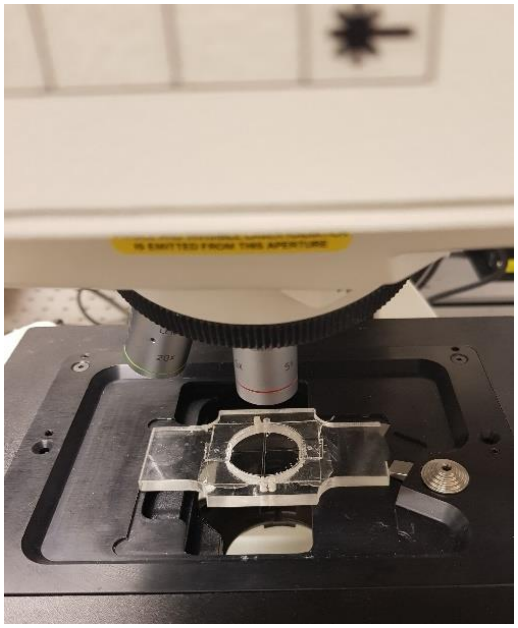

Figure 5.29 Microfluidic chip on microscope stage prepared to undergo Raman spectroscopy studies.

The MgF_2 displays an almost flat profile with low-intensity contributions except for a broad band around 1400 cm^{-1} and a single Raman peak below 400cm^{-1}.

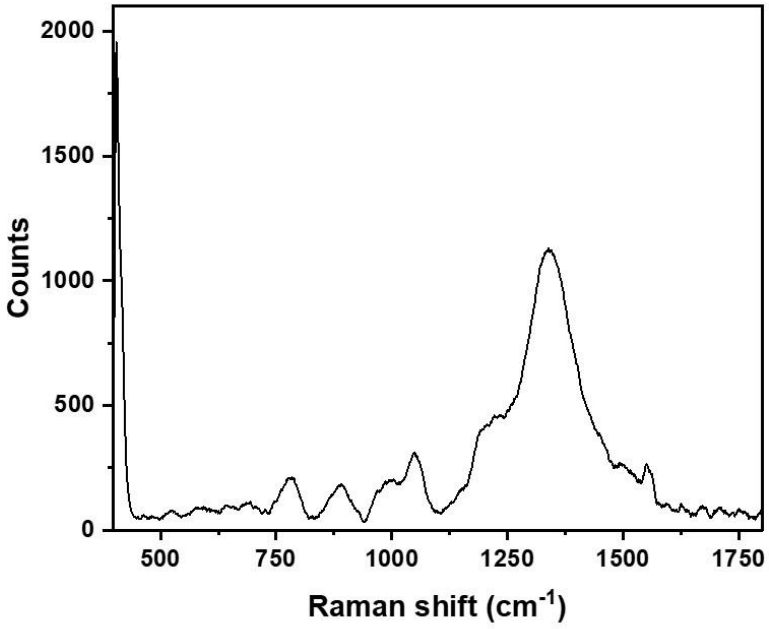

Figure 5.30 Raman spectrum of MgF_2 at 785 nm wavelength (100x,100%,30s,3acc).

Additionally, the spectra shown in Figure 5.31 compares the spectrum of MgF_2 to the spectrum of fused silica capillary used for the first microfluidic platform introduced in this thesis. Spectra were obtained with a 785nm Raman laser spot focused at the bottom of the chip's channel for a 30 seconds acquisition time, three accumulations, and a 1200 l/mm grating configuration using a 100x objective for signal collection.

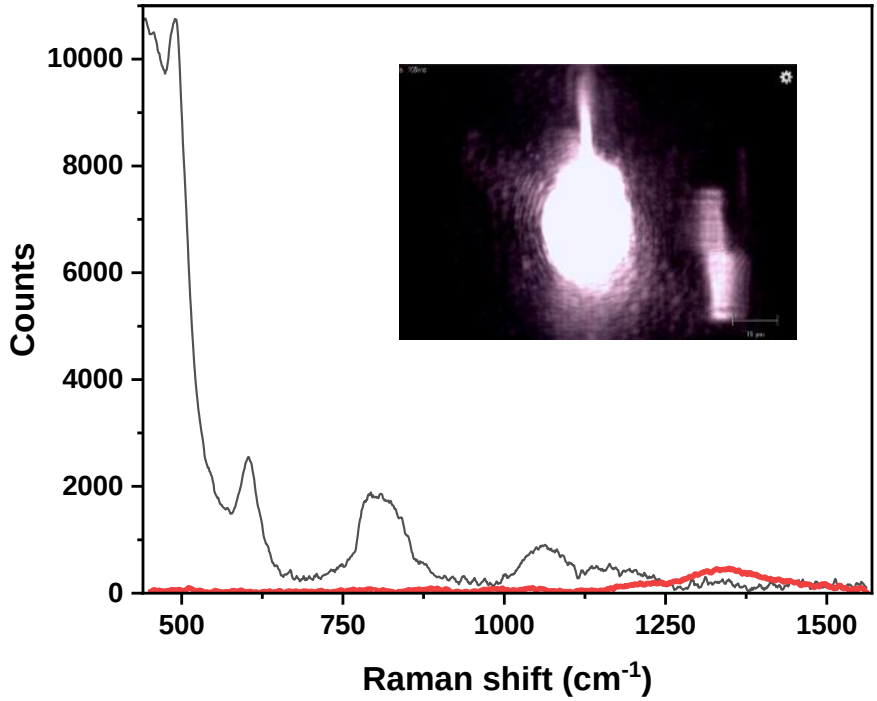

Figure 5.31 Background Raman spectrum of a MgF_2 – PDMS microchip (red). The illustration shows the Raman beam spot focused on the MgF_2 coverslip placed at the bottom of the device (microchip base). A fused silica spectrum (black) collected under the same spectrograph parameters is displayed for comparison of their Raman signal intensities.

After the spectral characterization of the device, and prior to each experiment, an alignment protocol, as described in Section 5.1, was performed by adjusting the mechanical components of the stage that holds the fibers in place and assessing the appearance of the optical trap by using an IR viewer

An example of a proper fiber core alignment is depicted in Figure 5.32, which shows a point of light within the microchip. Light concentrates at a single spot between the fibers within the interrogation area.

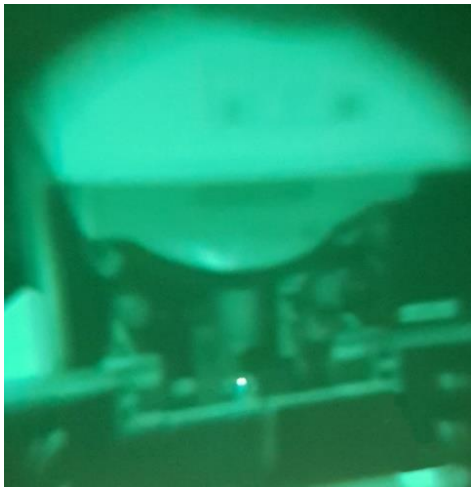

Figure 5.32 Infrared view of a fiber-based optical trap. Two optical fibers acting as waveguides were introduced into the microchip's fiber channels for core alignment.

5.2.2. Polystyrene beads trapping in microfluidic chip platform

Once again polystyrene beads were use for testing the trapping power capabilities of our dual beam optical trap. PS beads were injected into the system at known concentrations to determine a suitable system flow rate that places a sphere within the examination area constantly every 30 - 60 seconds to allow the capture of particles for spectrographic analysis. Based on the results presented in Section 5.1.2. during the capillary system characterization, the most adequate bead concentration proved to be a 1:40 mixture of PS bead solution and PBS.

The microfluidic chip was placed on the platform holder, in the configuration shown in Figure 4.4. Optical fibers connected to a laser diode operating at 1064 nm were introduced

into the chip fiber channels perpendicular to the examination area. The optical power emerging from each fiber was studied and adjusted.

The tested flow rates varied between 0.01 and 0.35 µL, using as limiting value the breaking point of the PDMS wall between the flow channel and the fiber channel occurring at 0.7 µL/min (Section 5.2.1).

The trap with a diameter of ≈42.5 µm (calculation available in Appendix A3) was manually activated upon detection of a sphere entering the examination zone. The polystyrene solution was flown at increasing intervals of 0.2 µL/min against the trapping output powers of the beams of 30 to 60 mW.

Table 5-3 Dynamic flow of polystyrene beads in central microchip channel subject to different cLDD power settings (mW).

Flow rate (µL/min)	30	40	50	60
0.01	+	+	+	+
0.05	+	+	+	+
0.19	-	+	+	+
0.31	-	-	+	+
0.37	-	-	-	+

The results shown in Table 5-3 provide the maximum flow rate at which that specific power output performed a successful trapping of individual beads. A successful trapping of the PS bead was marked with a plus (+) symbol while the failure of stopping a bead was noted with a minus (-) symbol. These results were used to test the accuracy of the in-chip trapping and establish an adequate flow rate/power trap combination.

Figure 5.33 shows the trapping results using three different microfluidic chips. The experiment performed in triplicate intended to rule out any change in values related to chip

construction or the fiber alignment process. The most effective configuration was 0.21 µL/min combined with a cLDD power setting of 50 mW. The chosen values allow both the visualization and the entrapment of PS beads, and the flow rate value stays below the speed at which the chip walls break.

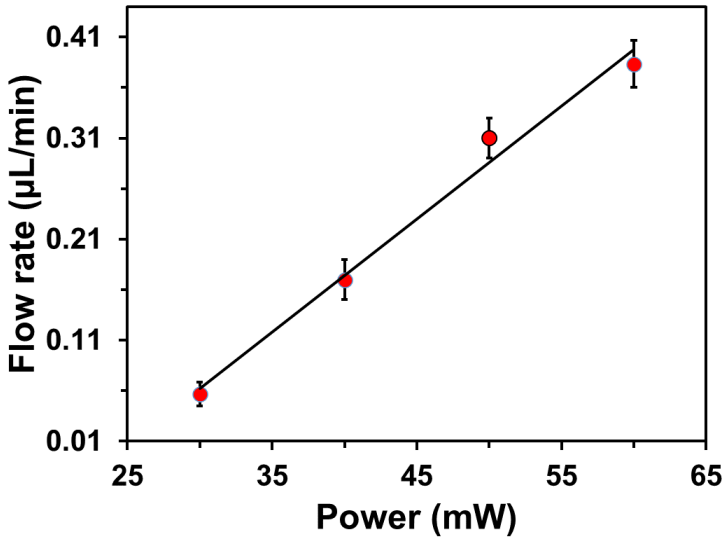

Figure 5.33 Plot indicating the trapping velocity tresholds as a function of laser power setting. Efficiency of the system trapping 5µm polystyryne beads.

The finding of a desirable sample concentration and an adequate flow rate was followed by Raman examination. Once trapped, the beads were ready to be analyzed by the Raman laser, orthogonally positioned to the examination area. The laser beam was focused on the bead at the position where the trapping happened within the microchannel. Each spectrum was collected for 10s in static mode from 474 cm^{-1} to 1620 cm^{-1} using a 1200 l/mm grating. The intensity of the 1000 cm^{-1} benzene ring breathing mode in the polymer was monitored. As soon as the Raman acquisition spectra of the 5 µm polystyrene spheres was completed,

the optical trap was deactivated, and the particles resumed their way down the channel, Figure 5.34.

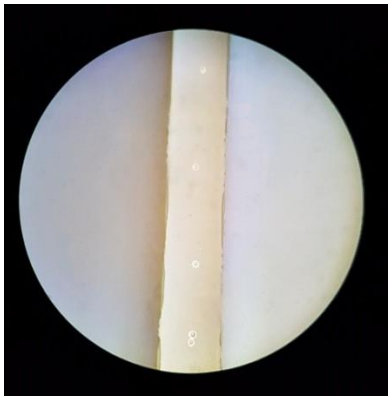

Figure 5.34 Polystyrene spheres in microflow channel 50x objective

The observed bands in Figure 5.35 effectively correspond to the polystyrene spectrum. Therefore, the main goal of the microchip of integrating optical traps to hold smalls transparent objects for Raman spectroscopy analysis was accomplished.

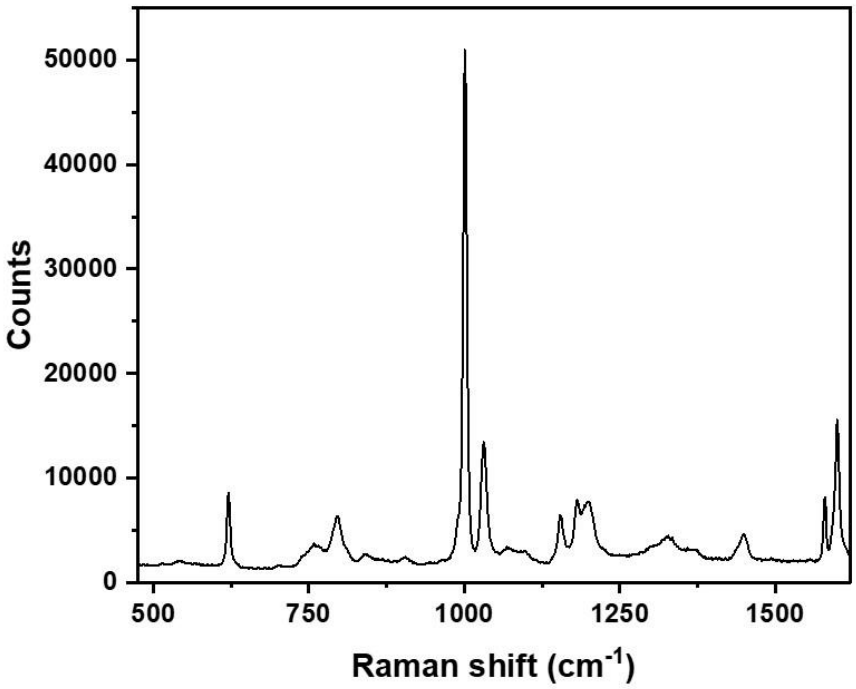

Figure 5.35 Raman spectrum of a trapped PS beads in a MgF_2/PDMS chip

However, during the experiment, a considerable number of challenges occurred that questioned the feasibility of using the optical fibers with the current chip configuration.

The optical fibers were placed inside holders. The holders consist of syringe needles (26 gauge) with the sharp end flattened and a diameter of 450 µm. The tube diameter was used as a reference to create microchip channels large enough to house said holders and allow extra space for the adjustment of the fibers and their positioning relative to each other for core alignment, resulting in the creation of channels 500 micrometers tall. This magnitude of channel height is unusual for microfluidic devices and reduces the likelihood of a sphere passing through the entrapment area.

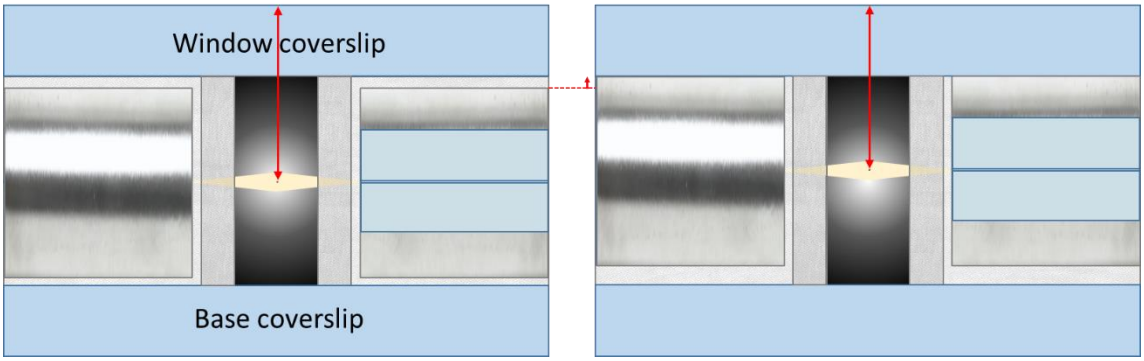

Figure 5.36 Partial crossection side view of microfluidic device in scale. a) shows two aligned optical fibers (left: fiber is within guiding metal tubing; right: crossection view of tubing, cladding and fiber core) with counterpropagating fiber laser beams separated by a flow channel (center: flow channel is separated from the fibers by PDMS walls). A 5µm bead is trapped by light forces midwater in the flow channel at a depth of 247 µm. b) shows the highest position within the channel that the fiber cores can be adjusted. A trapped bead is held approximately at 224 µm from the window or 270 µm from the base coverslip.

A centered optical trap (with respect to the flow channel y-axis), as seen in Figure 5.36a, with a dimension of 42 µm translates in approximately 229 µm below and above the optical trap that allows for flowing beads to avoid the forces coming from the counterpropagating

fibers. It was not unusual to see spheres being pushed towards the bottom or top of the channel without being stopped.

The conditions of this experiment made it possible to obtain the spectrum of spheres due to the low contribution of PDMS from the device walls, the low contribution of MgF_2, and the easily identifiable characteristic peak at 1000 cm^{-1} of polystyrene. Height, however, seems to forecast a significant limitation when moving on from a simple spectrum to working with human cancer cells.

5.2.3. Cell trapping in microfluidic chip platform

The microfluidic chip was tested to prove its capacity to trap and analyze two cancer cell lines: MCF-7 and MDA-MB-231.

In the previous experiment involving MCF-7 cells (Section 5.1.3), visualization within the capillary system was impossible. Therefore, the first step for running cellular assays within the microchip platform was to verify their visibility.

A few drops of cell stock solution (Section 4.1.2) were deposited directly on the microchip inlet using a micropipette for the liquid to get into the channel by capillarity forces.

Initially, the visualization of the cells was not evident to the naked eye; therefore, minor modifications to the system and the apparatus were done. A practical solution was to place an aluminum sheet below the chip and down the hole of the metal microchip holder. Furthermore, the settings of the monitor, connected to the spectrograph, were adjusted to increase the contrast, sharpness, and brightness.

The use of aluminum foil under the examination area of the chip was an easy and inexpensive way to increase contrast with the background without affecting the spectra. Al

foil produces low and almost featureless background spectra, which enables the acquisition of high-quality IR and Raman spectra without substrate interference or sacrificing important fingerprint biochemical information from the specimens.[166] Figure 5.37 shows the presence of MCF-7 cells in the interior of the microchip channel, observable after the changes made to the system.

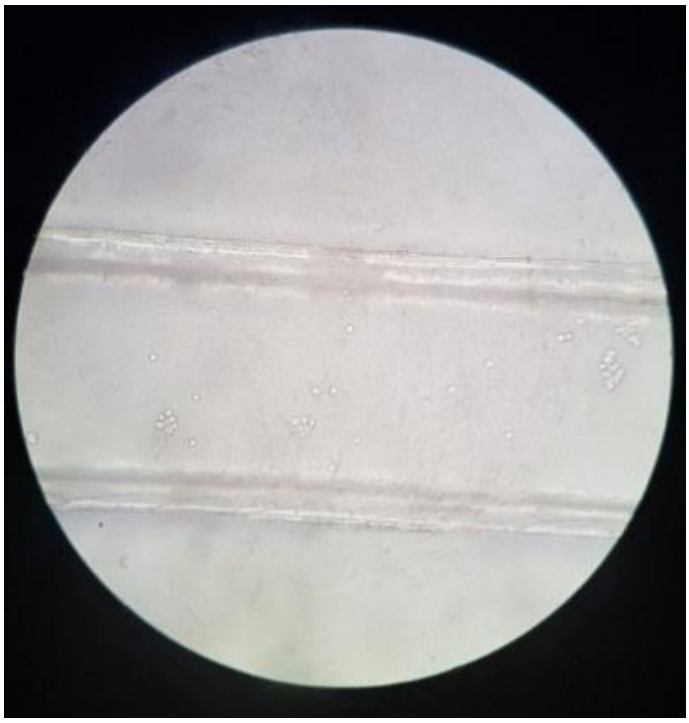

Figure 5.37 MCF-7 cells within the flow channel

The microchip was a one-session device, meaning that only one cell line was introduced into the system during the experimental sessions that lasted approximately 4-6 hours each to avoid cross-contamination between cell lines. After finalizing the experiment, the chip was placed into 70% alcohol for disinfection, followed by a polymer remover bath to recover the MgF_2 substrate. The MgF_2 coverslips were reused for the creation of new microchips.

5.2.3.1. MCF-7 Cell Results

The cell samples (Section 4.1.2) were injected into the chip to find the optimum combination of cells per minute and the power needed to trap them.

The flow rate was programmed to run at 0.01 to 0.35 µL per minute at increments of 0.02 µL through the 3.5 mm long chip channel ($3.5mm^3$) and tested against the trapping force of the fibers. Results are shown in Table 5-4, where successful trapping performed at a selected power setting against a flow rate was marked with a plus (+) symbol, while the failure of stopping or slowing down the motion of a cell was noted with a minus (-) symbol.

Table 5-4 Dynamic flow of MCF-7 in the central flow channel subject to different cLDD power settings (mW).

Flow rate (µL/min)	30	40	50	60	70	80
0.01	-	+	+	+	+	+
0.09	-	+	+	+	+	+
0.17	-	-	+	+	+	+
0.27	-	-	-	+	+	+
0.31	-	-	-	-	+	+
0.35	-	-	-	-	-	+

Figure 5.38 illustrates how the optical trap was activated when a cell was detected approaching the examination area. The movement of the cells along the capillary was tracked by confocal microscopy, while the fiber trap was manually operated via the CLD interface.

The trapping experiment was carried out in triplicate. Each study was conducted using a different chip to rule out any change in values related to chip construction or the fiber alignment process. Figure 5.39 shows the accuracy of the trapping, and the plot of flow rate vs. power setting was used for selecting adequate system values for the subsequent

Raman examination studies. Finally, a flow rate of 0.15 µL/min and an optical power setting of 60mW became the selected parameters for cell entrapment.

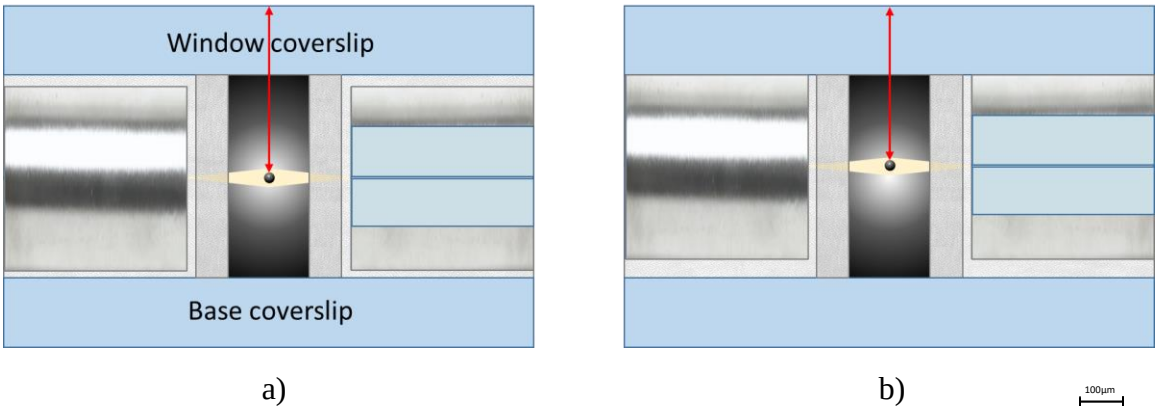

Figure 5.38 Partial crossection side view of microfluidic device in scale. a) shows two aligned optical fibers (left: withing guiding metal tubing; right: crossection view of tubing, cladding and fiber core) with counterpropagating fiber laser beams. A 30µm MCF-7 cell is trapped by light forces midwater at a depth of 235 µm. b) Shows the highest position within the channel that the fiber cores can be adjusted. A trapped bead is held approximately at 210 µm from the window or 260 µm from the base coverslip.

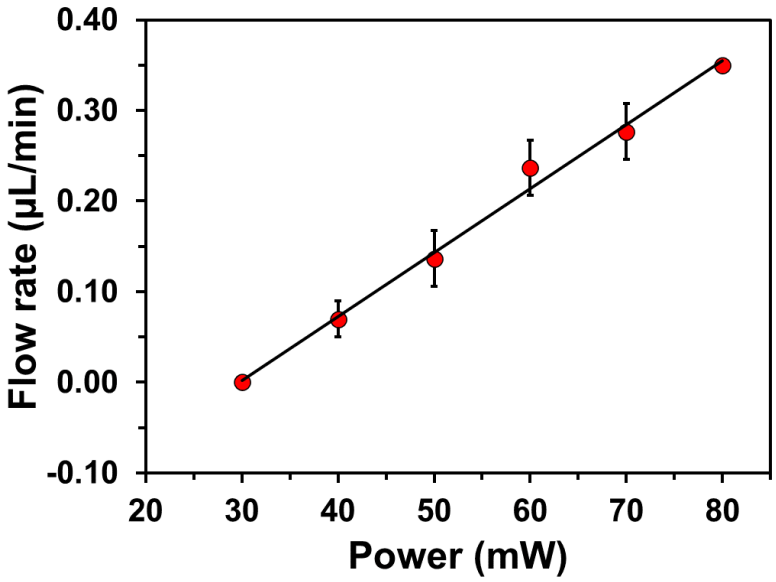

Figure 5.39 Accurracy of the chip system for the trapping of MCF-7 cells. Plot indicates the trapping velocity thresholds as a function of laser power setting.

Raman spectra of the cancer cells were collected for 10 s in static mode and a collection area of 500 cm^{-1} to 1560 cm^{-1} with a 100x objective with an excitation power of 100% focused on the center of the cell trapped in the middle of the channel.

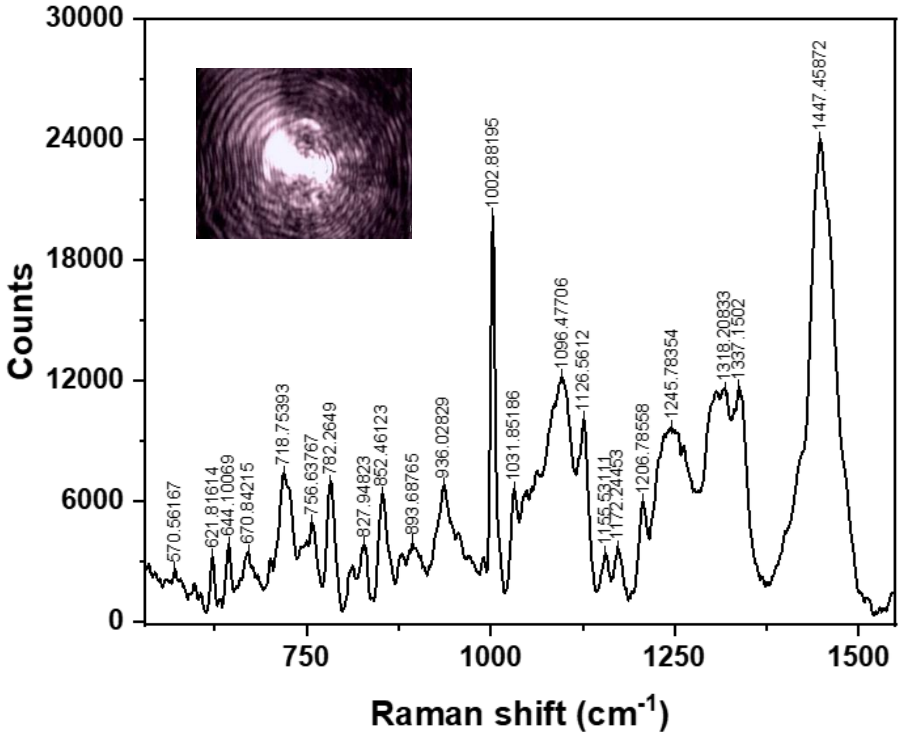

Figure 5.40 MCF-7 spectrum collected with a 100x objective for 10s, 3acc, 100% in a 1200 l/mm grating configuration.

After the acquisition of Raman spectra was completed, the optical trap got deactivated, and the particles resumed their way down the channel.

Figure 5.40 shows the collected spectrum of a trapped MCF-7 cell trapped after background removal. The spectrum shows several characteristic peaks of breast cancer cells, including lipids, proteins, amides, nucleic acids, and amino acids.

Table 5-5 summarizes the main cell peaks obtained experimentally and compares them with those contributions associated with cancerous breast tissue presented by Lazaro-Pacheco.[167] Very small differences can be observed in the frequencies of spectral peak

assignments that occur due to the biological/chemical changes during sample handling and variations in analytical instrumentation. Nevertheless, the position of the peaks obtained experimentally is consistent with those from the literature.

Table 5-5 Raman spectral assignments for MCF-7 breast tissue.[a]

Wavenumber/ cm^{-1}		Peak assignment
Lit.[b]	Exp.[b]	
1446	1447	CH_2 bending mode of proteins. CH_2 overlapping asymmetric CH_3 bending & CH_2 scissoring (associated with elastin, collagen, and phospholipids)
1443	1447	CH_2 deformation (lipids and proteins)
1336	1337	Polynucleotide chain (DNA-purine bases)
1335-1345	1335-1345	CH_3CH_2 wagging mode of collagen
1313	1318	CH_3CH_2 twisting mode of collagen/lipids
1304	1300	CH_2 deformation (lipid)/adenine, cytosine
1300	1300	C-H (CH_2) bend. Lipids
1265-1240	1265-1240	Amide III (C-N stretching mode of proteins, indicating mainly α-helix conformation)
1264	1260	=C–H in plane bending (lipid)
1260	1260	Amide III: unordered. C-N-H (ν (CN), δ(NH) amide III, α-helix conformation collagen, tryptophan; and $PO2^-$ asymmetric (Phosphate I))
1258	1260	Amide III/adenine/cytosine
1243	1245	Amide III: collagen (CH_2 wag, C-N stretch)/pyrimidine bases (C, T)
1206	1206	Hydroxyproline, tyrosine
1170	1172	C-H in-plane bending mode of tyrosine
1155	1155	C-C (& C-N) stretching of proteins and carotenoids
1123	1126	C-C stretching mode of lipids/protein C-N stretch/glucose
1096	1096	O-P-O (stretching PO_2^- symmetric (Phosphate II) of phosphodiesters
1083	1088	C-N stretching mode of proteins (and lipid mode to lesser degree)
1064	1065	Skeletal C-C stretch lipids
1061-1028	1061-1028	ν_3 (PO_4) Hydroxyapatite- Type II calcification
1031	1031	C-H in-plane bending mode of phenylalanine
1001	1002	Symmetric ring breathing mode of phenylalanine
968	970	C-C stretching lipids
957	956	Hydroxyapatite/carotenoid/cholesterol
935	936	C-C stretching mode of proline and valine and protein backbone (α-helix conformation)/glycogen
880	880	Lipids/carbohydrates/collagen
853	852	Ring breathing mode of tyrosine and C-C stretch of proline ring

826	827	O-P-O stretch (DNA)
781	782	Cytosine/uracil ring breathing (nucleotide)
780	782	C-C (C-C stretch of proline, hydroxyproline and tyrosine and v_2 PO_2^- stretch of nucleic acids bands)
755	756	Symmetric breathing of tryptophan
717-719	718	C-N (membrane phospholipid head)/adenine
669	670	C-S stretching mode of cystine
643	644	C-C twisting mode of tyrosine
621	621	C-C twisting mode of phenylalanine
573	570	Tryptophan/cytosine, guanine

[a] Adapted from ref **[167]**

[b] Abbreviations— Lit.: literature; Exp.: experimental. Standard notation is used for chemical groups.

Despite initial limitations, the device achieved stable cell entrapment that allowed the acquisition of biological spectra. Raman characterization took place in a device constructed with MgF_2 and PDMS as substrates, which had not been used previously. The elements involved in the elaboration of this system are easy to modify, which results in a highly adaptable platform.

Based on the results obtained in the capillary platform, it was determined that the adequate flow to analyze beads was 0.25µl/min at a power of 50mW. In the case of the chip, this value changed to 0.21 µL/min at 50 mW and changed again for single cells with a flow rate of 0.15 µL/min at 60 mW at a concentration of 1000 cells per milliliter. Potential factors for these changes are increased distance between optical fibers, asphericity of cancer cells, and sample/media refractive index ratio compared to almost perfectly spherical PS beads. Regarding beam divergence, a spot size decrease of 6.4% was produced in the chip compared to the capillary system, which depends on factors such as fiber gap and refractive index of each platform substrates. This size exceeds the average MDA-MB-231 and MCF-7 cell size of 20 µm.

5.2.3.2. MDA-MB-231 Cell Results

MDA-MB-231 cell samples were prepared as previously established in Section 4.1.2. Furthermore, they were injected into the MgF_2-PDMS chip to determine the optimum combination of cells traveling through the chip's examination area per minute and the minimum laser power needed to stop their flow and optically trap them.

The microfluidic chip, with a 3.5 mm long flow channel ($3.5mm^3$), was placed on the platform holder, in the configuration shown in Figure 4.4, while the two optical fibers connected to a laser diode operating at 1064 nm were introduced into the chip fiber channels perpendicular to the examination area. The micropump was programmed to run at a flow rate of 0.15 µL/min as determined by the MCF-7 experiment and tested against the trapping force of the optical fibers.

The optical trap was activated when a cell approached the examination area. The movement of the cells along the capillary was tracked by confocal microscopy, while the fiber trap was manually operated via the CLD interface.

The MDA-MB-231 cells became problematic with no flow rate/power combination providing reproducible trapping of individual cells.

Regardless of the unsuccessful trapping of single MDA cells, Raman spectra of cells that became attached to the MgF_2 window were subjected to data analysis. Spectra were obtained in static mode with a 100x objective focused on the center of the cell, at a collection time of 10 s, excitation power of 100%, and 474 - 25890 cm^{-1} spectral window.

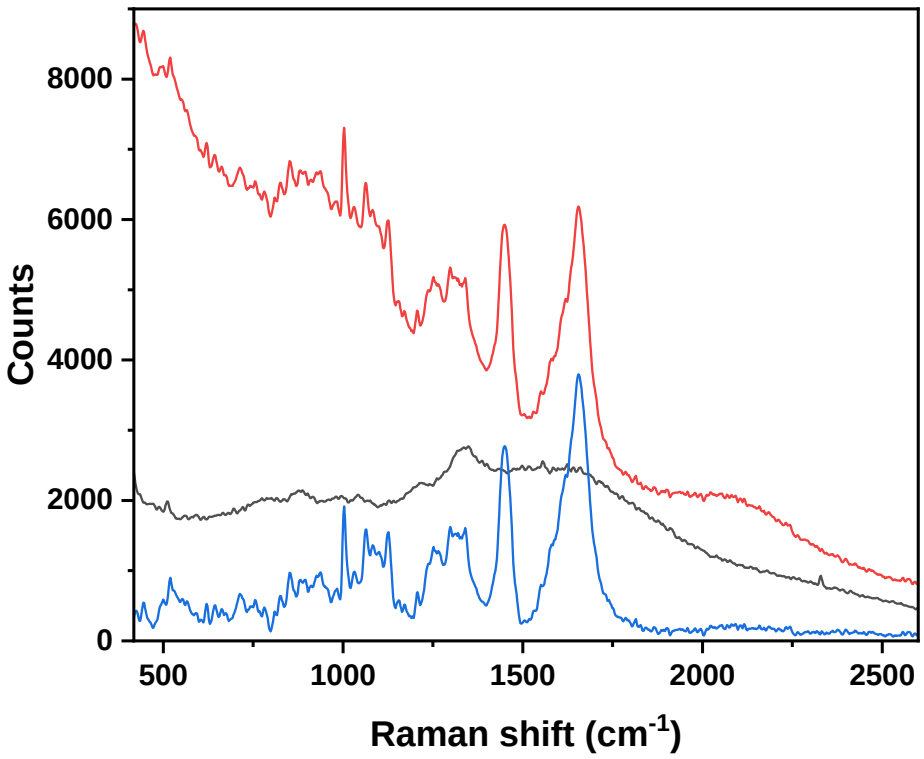

Figure 5.41 MDA spectrum collected with a 100x objective for 10s, 3acc, 100% in a 600 l/mm grating configuration. Raw spectrum (red), objective background (black), and background corrected spectrum (blue)

This second cell line proved complex to visualize within the capillary device, and although that problem was solved in the microchip, the results contrast with those obtained involving the MCF-7 cell line in the MgF_2-PDMS platform.

The trapping of MDA-MB-231 cells resulted in unsuccessful results, and because keeping the subject in a static position is necessary for performing the scanning by RS, it was not possible to obtain spectra from cells positioned away from the contact of the channel walls or windows.

Possible factors that could affect the entrapment of an object are its shape and its refractive index. MDA-MB-231 cells present an endothelial-like morphology, unlike MCF7 with a more spherical shape. In addition, the refractive index values of 1.399 for

MDA-MB-231 and 1.401 for MCF-7 are not virtually different to represent such a trapping hardship.

MDA cells were selected to extrapolate the device's functionality to other cell lines, and despite lacking an ideal cell positioning for RS analysis, the cell detection was performed once the flow stopped, and the cells began to adhere to the MgF_2 window. Regardless, this second cell line served its purpose in showing the optical limitations of the platform presented here.

6. Conclusions

In particular, this thesis detailed the fabrication of two microfluidic platforms, a fused silica capillary system and a hybrid microfluidic chip composed of MgF_2 and PDMS specifically designed to acquire Raman spectra from single cancer cells that aimed to improve a study for the detection of radiation-induced biochemical changes occurring in the cells during radiation treatment.

Efforts were devoted to constantly positioning cancer cells individually under the microscope and incorporating external optical traps generated by a diode laser operating at 1064nm to hold single cells long enough during Raman examination to obtain a proper spectrographic representation of their composition.

The fused silica-based capillary served to conduct preliminary studies on optical trapping, flow rate, and Raman acquisition to build a solid understanding of all-optical functions to be integrated into a single microfluidic chip and the system requirements for flowing, trapping, and examining a sample effectively. Additionally, a manually controlled mechanical platform was constructed to assist the optical fiber alignment.

Optical trapping was performed on PS beads flowing in solution within the capillary at a flow rate of 0.25μl/min. A laser power of 50mW was necessary to trap beads within an optical fiber trap with a 44.0μm diameter.

On the other hand, a microfluidic chip was manufactured following the results from the capillary platform. The fabrication process and its capability of fluidic manipulation for the specified biomedical purpose were tested.

Our chip comprised two transparent MgF_2 windows that enclose a layer of PDMS containing microfluidic channels. Although MgF_2 provides much superior access than

glass to the biological window of interest used in this project (450-1800 cm^{-1}), the material represented limitations for the design and handling of the chip since MgF_2 cannot undergo standard microfabrication processes and cannot be traditionally bonded to other materials.

The microchip fabrication process represents a novel fabrication process with a distinct sealing method while providing a clear window for Raman scattering examination with minimal background fluorescence. The reported maximum flow rate was determined as 0.7 μL/min, proving that the device's sealing can withstand up to 0.01 mbar or wall-sheer stress of 0.03 dyne/cm^2.

The chip successfully trapped PS beads in a laser spot of 42.50μm diameter at a flow rate of 0.22 μL/min with a 50mW trap and the trapping of MCF-7 cancer cells at a flow rate of 0.15 μL/min and requiring a 60mW laser setting. The trap allowed for the successive spectral acquisition of the particles for 10 to 30 seconds (2 cells/min). The Raman examination within the microchip yielded high-quality spectra that showed the distinct Raman signatures of the samples.

In conclusion, the PDMS-MgF_2 that integrates optical trapping and Raman spectroscopy analysis introduced in this work offers a label-free and non-destructive tool for examining tumorous cells. Although not ready to be implemented in the medical field, the system meets the requirements established at the beginning of this document and has the potential to perform the monitoring of radiation-induced response in tumours as a result of radiation exposure.

7. Future directions

The development of a microfluidic chip with the characteristics presented in this thesis represents a step closer to the final goal of providing easy access to a personalized diagnosis for cancer treatment with radiation.

Using an automated Raman-microfluidic system could potentially be used as a tool for patient profiling. Identifying individual patient responses could predict radiation-induced damage, prevent undesirable side effects, identify suitable candidates to undergo radiation while providing an individually tailored therapy, and serve as a monitoring tool during treatment.

This platform can facilitate the sampling of tumour cells, but the device's current status does not yet meet the requirements for clinical implementation. Before that, extensive system modification is required.

The search for the appropriate manufacturing conditions needs to continue, especially concerning room conditions such as room temperature variations. The presented manufacturing process requires the creation of ultra-thick layers of SU-8, which creates a strong tension on the wafer. The contraction or expansion of the silicon wafer used for mold creation contributes to mold fractures and detaching of SU-8 features resulting in only one in three molds completing the photo developing process.

Experimentally, although both microfluidic setups were significantly more complex than placing a cell sample on a MgF_2 disk, the cell spectra obtained were comparable to previous results from fixed cells proving that the procedure can be performed in a microfluidic system. Additionally, photolithography and PDMS make a relatively fast and cheap strategy for microfluidics prototyping that satisfies biocompatibility requirements and

allows relatively high spatial resolution with the potential for incorporating other assay modules to replace additional operations performed in the laboratory, such as tissue dissociation.

Further Raman spectral acquisition is necessary, which requires solving aggregation problems that block the systems during sample injection, making it possible to obtain more reproducible data for qualitative and quantitative analyses.

Multiple system modifications can be performed, such as exploring methods to increase the Raman signal, involving the addition of reflective elements within the main flow channel, studying cell clusters instead of focusing on single-cell experiments, or transitioning to a Raman-on-chip approach, which integrates fibers for trapping, Raman excitation, and signal detection in a single compact unit.

Nevertheless, for the implementation in the clinical setting, it is necessary to study further the feasibility of the novel RS approach for identifying biomarkers for radiation sensitivity determination and develop comprehensive spectral databases and tissue classification to guarantee its translation to microfluidics.

Appendix A

A.1. Optical fibers and beam diameter calculations

An optical fiber is a circular dielectric waveguide composed of a central core with a high refractive index, surrounded by a concentric cladding with a lower refractive index.

Figure A.1 shows that light propagates in an optical fiber by total internal reflection (TIR). This phenomenon is possible if the angle of incidence is bigger than the critical angle, preventing the rays from exiting the core by reflection.

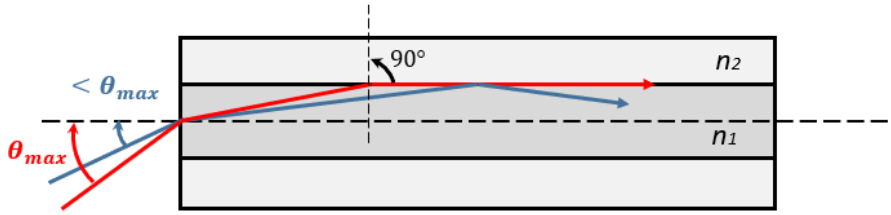

Figure A.1 Transversal view of an optical fiber. Color lines represent two light rays that meet the angular condition $\leq \theta_{max}$r TIR at the core-cladding interface when $n_1 > n_2$.

Rays launched into a fiber give rise to fiber modes, a discrete set of electromagnetic fields that propagate energy along the fiber. The light is said to excite guided modes that transport information and power. The cut-off angle for rays to enter and to couple into a guided mode, is known as the maximum acceptance angle (θ_{max}), which is related to the fiber's numerical aperture (NA)[168]. Single-mode fibers have only one guided mode, which is excited by rays with 0° angles of incidence. However, using the NA to estimate the cone of light emitted from, or that can be coupled into, a single mode fiber results in a non-zero value.

In single-mode fibers, the light does not behave as multiple rays travelling at different angles to the fiber's axis. Instead, the emitted light propagates similarly to a Gaussian beam.

Therefore, it cannot be properly described based on a purely geometrical optics and should be analyzed as an electromagnetic waveguide structure and described using the wave optics model.[169]

Beam divergence of an electromagnetic beam indicates the angular increase in beam diameter or beam radius over a distance from the optical aperture. The divergence can be calculated using the beam parameters illustrated in Figure A.2.

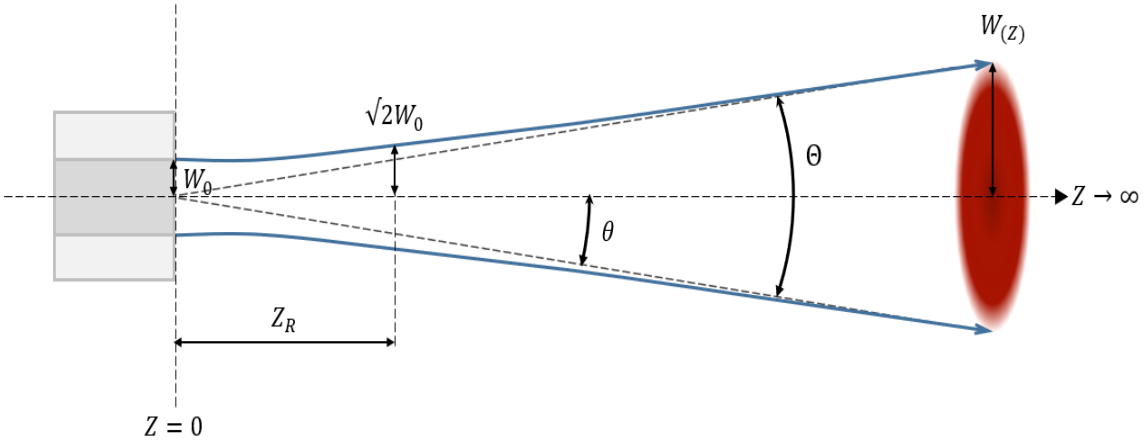

Figure A.2 Beam parameters of a beam exiting a single mode optical fiber; where *Z* is the distance of the medium the beam is traveling from the fiber end, W_0 is the beam waist (radius) at *Z*= 0. θ is beam divergence half angle, while Θ is the total angular spread. The Gaussian beam radius as a function of the distance *Z* is represented as $W_{(z)}$, and Z_R represents the Rayleigh range.

The waist or focus of a laser beam is where the beam radius, *W*, is at its minimum, W_0; specifically, when the beam exits the fiber at $Z = 0$.

As light propagates through a single-mode fiber, the beam maintains a cross-sectional Gaussian profile. As the tails of a Gaussian function never actually reach zero, *w* is defined as the distance from the beam axis to where the optical intensity drops to $1/e^2$ (≈ 13.5%) of the on-axis intensity value. The electric field strength drops to 1/e (≈ 37%) of the maximum

value at this radius. Therefore, we can conclude that a single-mode optical fiber's Mode Field Diameter (MFD) corresponds to twice the beam radius value and encloses ≈86% of the beam's power (Figure A.3**).**

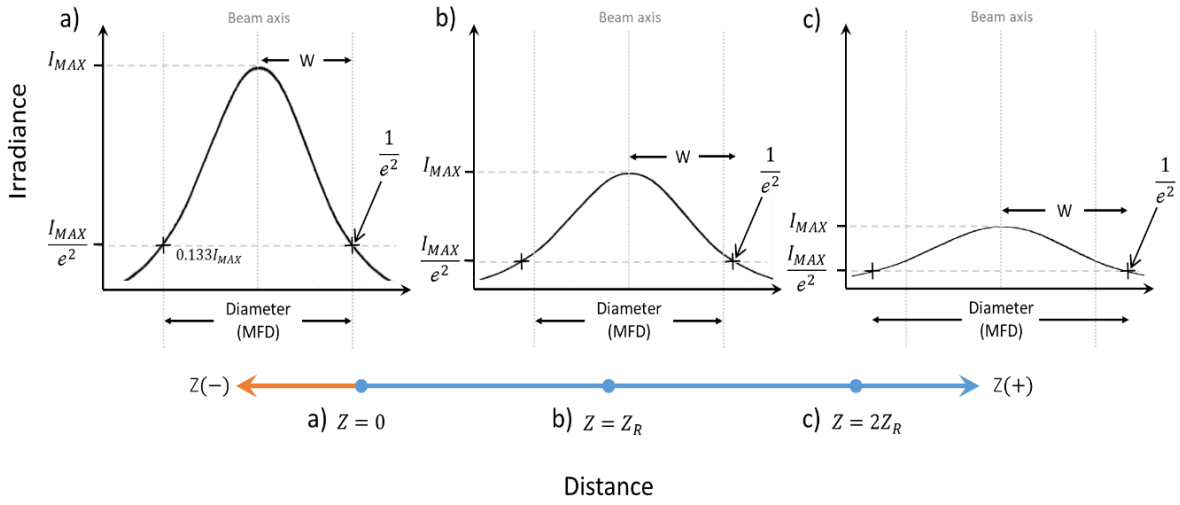

Figure A.3 Propagation effect of a Gaussian profile along a distance *Z*. Gaussian beam (a) exiting face of fiber *Z*=0, (b) at distance Z_R, and (c) at 2 Z_R. The MFD is represented as the distance across the center of the beam for which the irradiance equals *1/e*^{2} of the maximum value *1/e*^{2}=0.0135).

Z_R is known as the Raleigh range and is an indicator of the beam's divergence, as it refers to the distance over which the beam diameter is nearly constant before increasing linearly. The distance between the two points $Z = \pm Z_R$ is called the beam's confocal parameter or depth of focus represented as “b”.

When $Z = Z_R$ we have $W_{(z)} = \sqrt{2}W_0$. At Z_R, the mode radius is $\sqrt{2}$ larger than it is at the focus, which implies that at that point, the on-axis (r = 0) intensity is one-half of the peak intensity at $Z = 0$. That point along the beam is also where the wavefront curvature ($^1/_R$) is greatest.

For $Z >> Z_R$, the beam spot increases linearly with Z to form a cone shape. The angle between that cone of height $W_{(z)}$ and the beam axis is the divergence half-angle of the beam θ (in radians).

Assuming a diffraction-limited Gaussian beam, where the radial beam divergence is close to the minimum value possible, the $1/e^2$ radius is nonlinear for distances $Z < Z_R$, and is approximately linear in the far-field **($Z >> Z_R$),** the approximate value θ is given by

$$\theta = \frac{\lambda}{\pi W_0} \tag{A.1}$$

Where the beam waist W_0 controls θ for a given wavelength λ (in the medium), therefore, the total angular spread of the diverging beam, or apex angle of the above-described cone, is then given by

$$\Theta = 2\theta \tag{A.2}$$

Formulas (A.1) and (A.2) are based on the paraxial approximation, valid only for beams with moderate divergence. The paraxial approximation is used in Gaussian optics and ray tracing of light through an optical system and remains valid if the divergence angle value is under 1 rad, and the beam radius at a beam waist is larger than the wavelength.

If W_0 or the far-field θ are given, comprehensive characterization of a beam cone can be made by using the following equations

$$w_Z = w_0\sqrt{1 + \left(\frac{Z}{Z_R}\right)^2} \tag{A.3}$$

And,

$$Z_R = \frac{\pi W_0^2}{\lambda} \tag{A.4}$$

Where $W_{(z)}$ can be calculated at a known specified distance, Z, from W, while the Rayleigh length Z_R for a Gaussian beam is determined by λ and W_0.

Ray tracing can help to understand the ray behavior and trace the evolution of optical waves to mathematically describe the output properties of a Gaussian beam propagating through optical media. This method uses paraxial restrictions to simplify diffraction by geometric optical propagation. [170]

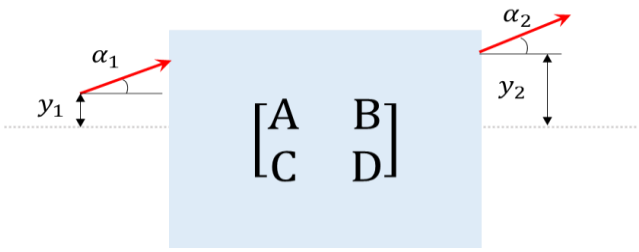

Figure 0.4 Example of an overal ray matrix

The resultant beam can be mathematically calculated by using an ABCD matrix[65,170]

$$\begin{bmatrix} y_2 \\ \theta_2 \end{bmatrix} = \begin{bmatrix} A & B \\ C & D \end{bmatrix} \begin{bmatrix} y_1 \\ \theta_1 \end{bmatrix} \tag{A.5}$$

By applying the matrix operator for dielectric surfaces that considers the different refractive index of the materials the path of light travels after exiting the fiber and reaching a flowing particle as well as the free space operator results in:

$$\begin{bmatrix} y_2 \\ \theta_2 \end{bmatrix} = \left[\begin{bmatrix} 1 & l_3 \\ 0 & 1 \end{bmatrix} \begin{bmatrix} 1 & 0 \\ 0 & \frac{n_2}{n_3} \end{bmatrix} \begin{bmatrix} 1 & l_2 \\ 0 & 1 \end{bmatrix} \begin{bmatrix} 1 & 0 \\ 0 & \frac{n_1}{n_2} \end{bmatrix} \begin{bmatrix} 1 & l_1 \\ 0 & 1 \end{bmatrix} \right] \begin{bmatrix} y_1 \\ \theta_1 \end{bmatrix} \tag{A.6}$$

The light passes through regions of air, fused silica, and liquid medium. Where l is the chosen distance the light travels per material and n is the index of refraction of the medium in which the beam is traveling.

A.2. Calculating beam diameter in capillary-based Microfluidic Platform

Initial calculations were performed to model the beam's divergence emitted from the single-mode fiber's end face in air using the equations (A.3) and (A.4). The given values used to complete the calculations are shown in Figure A.5.

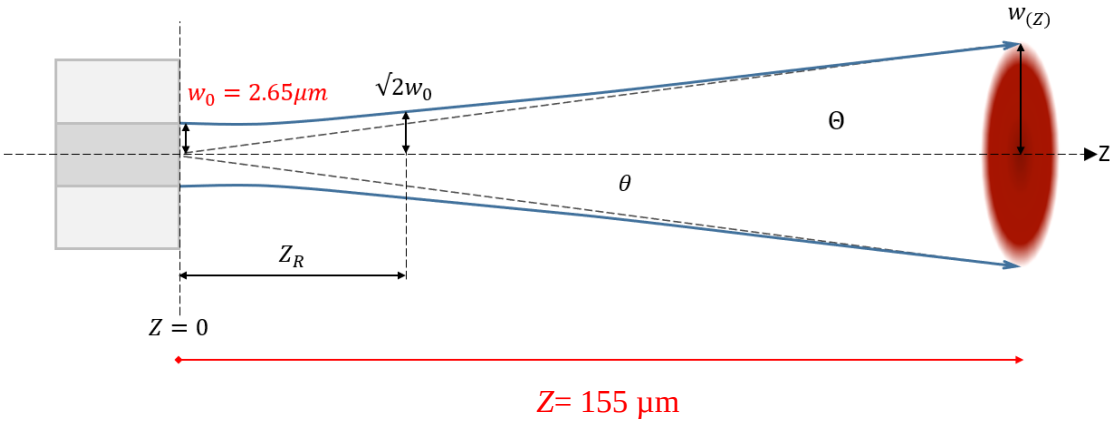

Figure A.5 Diagram of a cone shape beam exiting a single mode optical fiber with the known system values used in the experimental procedures.

Given,

$$Z_R = \frac{\pi 2.65\mu m^2}{1.064\mu m} = 20.73\ \mu m \tag{A.7}$$

$$W_Z = 2.65\ \mu m\sqrt{1 + \left(\frac{155\mu m}{20.73\mu m}\right)^2} = \approx 20\ \mu m \tag{A.8}$$

Where, the values used represent a beam reaching a bead positioned at Z= 155 µm. The value W_0 corresponds to 2.65 µm and the operating wavelength was 1064 nm.

The obtained Rayleigh range was determined to be 20.73 µm and the beam radius at 155 µm equals ≈ 20 µm or ≈ 40 µm MFD.

If the beam divergence is calculated from the slope value of a plot (Figure A.6), the equation of the line yields the following divergence half angle in radians:

$$y = 0.121x + 1.2311 \quad \text{(A.9)}$$

$$\theta = 0.121 \quad \text{or} \quad \measuredangle = 6.93° \quad \text{(A.10)}$$

In contrast, by using the far field approximation formula (A.1), the value θ is:

$$\theta = \frac{1.064}{\pi 2.65} = 0.128 \ \text{ or } \ \measuredangle = 7.33° \quad \text{(A.11)}$$

The values given in A.11 compared to A.10 represent an error of 5.78%. Although this error magnitude can be disregarded in optical setups, it represents a significant error in this specific Raman microfluidic configuration.

Therefore, ABCD matrices were used to calculate a more accurate divergence under two conditions: i) when an optical fiber is pressed against the capillary wall and ii) when an optical fiber is positioned at a distance Z_R from the flat capillary surface.

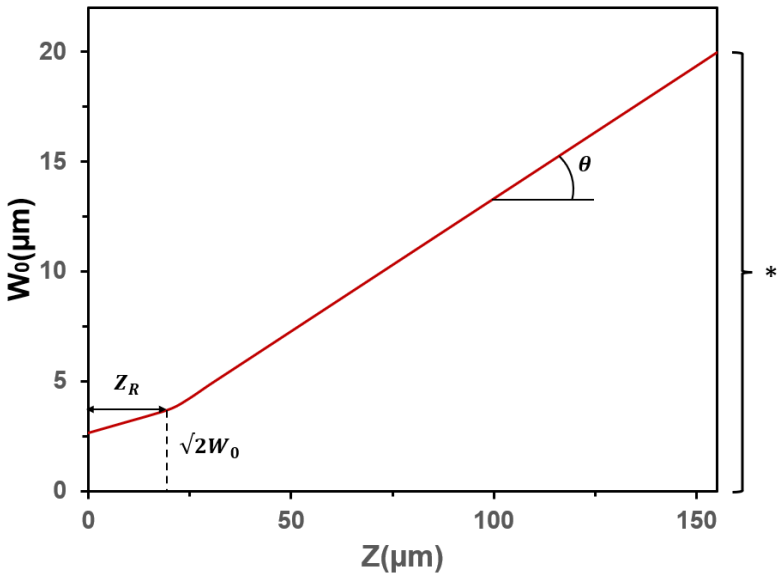

Figure A.6 This plot models a beam from a single mode fiber. The values used for *W*o and *Z* were 2.65 and 155 µm, respectively. The operating wavelength was 1064 nm, and the Rayleigh range was 20.73 µm. The value (*) represents the radius *W*(z).

Solving equation (A.6) for condition (i):

$$\begin{bmatrix} y_2 \\ \theta_2 \end{bmatrix} = \begin{bmatrix} 1 & Z_1 \frac{n_1}{n_2} + Z_3 \frac{n_1}{n_3} \\ 0 & \frac{n_1}{n_3} \end{bmatrix} \begin{bmatrix} y_1 \\ \theta_1 \end{bmatrix} \tag{A.12}$$

Where y_1 and θ_1 represent the height and slope values of the incoming ray while y_2 and θ_2 represent the resultant ray. The values Z_1 and Z_2 correspond to the distance of the medium the beam is traveling from the fiber end (Z_1=single capillary wall; Z_2=PBS buffer from wall to mid channel). The term n is the index of refraction of the medium the beam is traveling (n_1= air, n_2= fused silica, and n_3=PBS).

The incoming ray used for determining the divergence corresponds to a marginal ray, therefore $y_1 = W_0$= 2.65 µm, and θ_1=0.052. The ray travels Z_{cap}=125 µm and Z_{med}=30 µm. The refractive indices of air, glass, and PBS are n_{air}= 1.000, n_{cap}= 1.449, and PBS= 1.335

Resulting in y_2 and θ_2 values of 9.00 µm and 0.039 rad (2.23°) respectively.

While for condition (ii)

$$\begin{bmatrix} y_2 \\ \theta_2 \end{bmatrix} = \begin{bmatrix} 1 & Z_1 + Z_2 \frac{n_1}{n_2} + Z_3 \frac{n_1}{n_3} \\ 0 & \frac{n_1}{n_3} \end{bmatrix} \begin{bmatrix} y_1 \\ \theta_1 \end{bmatrix} \tag{A.13}$$

Where the ray travels $Z_{air} = Z_R$ = 21 µm, Z_{cap}=125 µm and Z_{med}=25 µm. Making $y_1 = W_0$= 2.65 µm, and θ_1=0.1210. The refractive indices of air, glass, and PBS are n_{air}= 1.000, n_{cap}= 1.449, and PBS= 1.335.

Resulting in y_2 and θ_2 values of 19.98 µm and 0.09 rad (5.15°) respectively. Which represents an increase beam spot size of ≈53.38% compared to a beam spot at a Z_{air}=155 µm.

A.3. Calculating beam diameter in Microfluidic Chip Platform

The divergent beam of each of the fibers arm can be calculated using an ABCD matrix presented in formula A.13 that considers the length and the diffraction index of the media that the beam traverses longitudinally before reaching the beads. Where y_1 and θ_1 represent the height and slope values of the incoming ray while y_2 and θ_2 represent the resultant ray. The term Z corresponds to the distance the beam travels through different media from the fiber end (Z_1=air; Z_2=PDMS, and Z_3=media), while n is the index of refraction of the medium the beam is traveling (n_1= air, n_2= fused silica, and n_3=media).

Where, Z_{air}= *21* µm, Z_{PDMS}=80 µm, and Z_{DMEM} =100 µm; n_{PDMS}= 1.383, and n_{DMEM}= 1.335 are the indices of refraction of the chip wall, and the cell media, respectively. W_0=2.65 µm is the initial beam waist (radius), and λ=1064 nm is the laser wavelength.

For a total traveling distance of 201 µm, y_2= 21.269 and θ_2= 0.09 rad (5.15°). While for a configuration where the fiber end sits as close as possible to the PDMS wall y_2= 9.559 and θ_2= 0.038 rad (2.23°). Which produces a beam spot 55% smaller than placing the fiber end ≈20 µm from the wall.

Bibliography

(1) Kim, J. H.; Jenrow, K. A.; Brown, S. L. Novel Biological Strategies to Enhance the Radiation Therapeutic Ratio. *Radiation Oncology Journal* **2018**, *36* (3), 172–181. https://doi.org/10.3857/roj.2018.00332.

(2) Radiation Therapy. In *Encyclopedia of Cancer*; Schwab, M., Ed.; Springer Berlin Heidelberg: Berlin, Heidelberg, 2011; pp 3144–3144. https://doi.org/10.1007/978-3-642-16483-5_4907.

(3) Gaspar, L. E.; Carsten, N. *Decision Tools for Radiation Oncology*, 1st ed.; Medical Radiobiology; Springer, Berlin, Heidelberg, 2014. https://doi.org/10.1007/978-3-642-37102-8.

(4) Barton, M. B.; Jacob, S.; Shafiq, J.; Wong, K.; Thompson, S. R.; Hanna, T. P.; Delaney, G. P. Estimating the Demand for Radiotherapy from the Evidence: A Review of Changes from 2003 to 2012. *Radiotherapy and Oncology* **2014**, *112* (1), 140–144. https://doi.org/10.1016/j.radonc.2014.03.024.

(5) Radiation Therapy (RT) http://www.bccancer.bc.ca/our-services/treatments/radiation-therapy (accessed 2022 -01 -15).

(6) Kaye, G. W. C. Wilhelm Conrad Röntgen: And the Early History of the Roentgen Rays. *Nature* **1934**, *133* (3362), 511–513. https://doi.org/10.1038/133511a0.

(7) Rosenbusch, G.; de Knecht-van Eekelen, A. Born for Business, Raised for Science (1845–1865). In *Wilhelm Conrad Röntgen: The Birth of Radiology*; Rosenbusch, G., de Knecht-van Eekelen, A., Eds.; Springer Biographies; Springer International Publishing: Cham, 2019; pp 1–11. https://doi.org/10.1007/978-3-319-97661-7_1.

(8) Bernier, J.; Hall, E. J.; Giaccia, A. Radiation Oncology: A Century of Achievements. *Nature Reviews Cancer* **2004**, *4* (9), 737–747. https://doi.org/10.1038/nrc1451.

(9) Cosset, J.-M. L'aube de la radiothérapie, entre coups de génie, drames et controverses. *Cancer/Radiothérapie* **2016**, *20* (6–7), 595–600. https://doi.org/10.1016/j.canrad.2016.08.123.

(10) Knight, N.; Wilson, J. F. The Early Years of Radiation Therapy. In *A History of the Radiobiological Sciences*; Reston (VA): Radiology Centennial, 1996.

(11) News of Science. *Science* **1957**, *125* (3236), 18–22. https://doi.org/10.1126/science.125.3236.18.

(12) Williams, J. P.; Newhauser, W. Normal Tissue Damage: Its Importance, History and Challenges for the Future. *Br J Radiol* **2019**, *92*, 20180048. https://doi.org/10.1259/bjr.20180048.

(13) Khan, F. M.; Gibbons, J. P. *Khan's The Physics of Radiation Therapy*, 5th ed.; Lippincott Williams & Wilkins: Philadelphia, PA, 2014.

(14) *Handbook of Evidence-Based Radiation Oncology*, 3rd ed.; Hansen, E. K., Roach III, M., Eds.; Springer International Publishing, 2018.

(15) Fry, D.; Harvie, R.; Mullett, L.; Walkinshaw, W. A Travelling-Wave Linear Accelerator for 4-Mev Electrons. *Nature* **1948**, *162* (4126), 859–861. https://doi.org/10.1038/162859a0.

(16) Lee, S. External radiation therapy https://cancer.ca/en/treatments/treatment-types/radiation-therapy/external-radiation-therapy (accessed 2021 -01 -15).

(17) Tait, D. M.; Nahum, A. E.; Meyer, L. C.; Law, M.; Dearnaley, D. P.; Horwich, A.; Mayles, W. P.; Yarnold, J. R. Acute Toxicity in Pelvic Radiotherapy; a Randomised Trial of Conformal versus Conventional Treatment. *Radiotherapy and Oncology* **1997**, *42* (2), 121–135.

(18) Langen, K. M.; Jones, D. T. L. Organ Motion and Its Management. *Int. J. Radiation Oncology Biol. Phys* **2001**, *50* (1), 265–278. https://doi.org/10.1016/S0360-3016(01)01453-5.

(19) Durante, M.; Paganetti, H.; Pompos, A.; Kry, S. F.; Wu, X.; Grosshans, D. R. Report of a National Cancer Institute Special Panel: Characterization of the Physical Parameters of Particle Beams for Biological Research. *Medical Physics* **2019**, *46* (2), e37–e52. https://doi.org/10.1002/mp.13324.

(20) Nimmagadda, S.; Ford, E. C.; Wong, J. W.; Pomper, M. G. Targeted Molecular Imaging in Oncology: Focus on Radiation Therapy. *Seminars in Radiation Oncology* **2008**, *18* (2), 136–148. https://doi.org/10.1016/j.semradonc.2007.10.009.

(21) Lawrence, T.; Chang, E. Y.; Hahn, T. M.; Hertel, L. W.; Shewach, D. S. Radiosensitization of Pancreatic Cancer Cells by 2',2'-Difluoro-2'-Deoxycytidine. *Int. J. Radiation Oncology Biol. Phys.* **1996**, *34* (4), 867–872.

(22) Zhang, X.-D.; Luo, Z.; Chen, J.; Shen, X.; Song, S.; Sun, Y.; Fan, S.; Fan, F.; Leong, D. T.; Xie, J. Ultrasmall Au $_{10–12}$ (SG) $_{10–12}$ Nanomolecules for High Tumor Specificity and Cancer Radiotherapy. *Adv. Mater.* **2014**, *26* (26), 4565–4568. https://doi.org/10.1002/adma.201400866.

(23) *Cancer Gene Profiling: Methods and Protocols*, Second edition.; Grützmann, R., Pilarsky, C., Eds.; Methods in molecular biology; Humana Press: New York, N.Y, 2016.

(24) Simpson, N. E.; Tryndyak, V. P.; Beland, F. A.; Pogribny, I. P. An in Vitro Investigation of Metabolically Sensitive Biomarkers in Breast Cancer Progression. *Breast Cancer Res Treat* **2012**, *133* (3), 959–968. https://doi.org/10.1007/s10549-011-1871-x.

(25) Zhang, M.; Kleber, S.; Rohrich, M.; Timke, C.; Han, N.; Tuettenberg, J.; Martin-Villalba, A.; Debus, J.; Peschke, P.; Wirkner, U.; Lahn, M.; Huber, P. E. Blockade of TGF- Signaling by the TGF R-I Kinase Inhibitor LY2109761 Enhances Radiation Response and Prolongs Survival in Glioblastoma. *Cancer Research* **2011**, *71* (23), 7155–7167. https://doi.org/10.1158/0008-5472.CAN-11-1212.

(26) Bolla, M.; Collette, L.; Blank, L.; Warde, P.; Dubois, J. B.; Mirimanoff, R.-O.; Storme, G.; Bernier, J.; Kuten, A.; Sternberg, C.; Mattelaer, J.; Torecilla, J. L.; Pfeffer, J. R.; Cutajar, C. L.; Zurlo, A.; Pierart, M. Long-Term Results with Immediate Androgen Suppression and External Irradiation in Patients with Locally Advanced Prostate Cancer (an EORTC Study): A Phase III Randomised Trial. *The Lancet* **2002**, *360* (9327), 103–108.

(27) Messing, E. M.; Manola, J.; Sarosdy, M.; Wilding, G.; Crawford, E. D.; Trump, D. Immediate Hormonal Therapy Compared with Observation after Radical Prostatectomy and Pelvic Lymphadenectomy in Men with Node-Positive Prostate Cancer. *N Engl J Med* **1999**, *341* (24), 1781–1788. https://doi.org/10.1056/NEJM199912093412401.

(28) Chang, D. S.; Lasley, F. D.; Das, I. J.; Mendonca, M. S.; Dynlacht, J. R. *Basic Radiotherapy Physics and Biology*; Springer International Publishing: Cham, 2014. https://doi.org/10.1007/978-3-319-06841-1.

(29) Schwab, Manfred. *Encyclopedia of Cancer*, 3rd ed.; 2011. https://doi.org/10.1007/978-3-662-46875-3.

(30) Bergonie, J.; Tribondeau, L. Interpretation of Some Results from Radiotherapy and an Attempt to Determine a Rational Treatment Technique. *Yale Journal of biology and medicine* **2003**, *76*, 181–182.

(31) Foray, N.; Colin, C.; Bourguignon, M. 100 Years of Individual Radiosensitivity: How We Have Forgotten the Evidence. *Radiology* **2012**, *264* (3), 627–631. https://doi.org/10.1148/radiol.12112560.

(32) Haber, A. H.; Rothstein, B. E. Radiosensitivity and Rate of Cell Division: "Law of Bergonie and Tribondeau." *Science* **1969**, *163* (3873), 1338–1339. https://doi.org/10.1126/science.163.3873.1338.

(33) Vogin, G.; Foray, N. The Law of Bergonié and Tribondeau: A Nice Formula for a First Approximation. *International Journal of Radiation Biology* **2013**, *89* (1), 2–8. https://doi.org/10.3109/09553002.2012.717732.

(34) Withers, H. R. The Four R's of Radiotherapy. *Advances in Radiation Biology* **1975**, *5*, 241–271. https://doi.org/10.1016/B978-0-12-035405-4.50012-8.

(35) Steel, G. G.; McMillan, T. J.; Peacock, J. H. The 5Rs of Radiobiology. *Int. J. Radiat. Biol.* **1989**, *56* (6), 1045–1048.

(36) Italiano, A. Prognostic or Predictive? It's Time to Get Back to Definitions! *JCO* **2011**, *29* (35), 4718–4718. https://doi.org/10.1200/JCO.2011.38.3729.

(37) Houssami, N.; Ciatto, S.; Macaskill, P.; Lord, S. J.; Warren, R. M.; Dixon, J. M.; Irwig, L. Accuracy and Surgical Impact of Magnetic Resonance Imaging in Breast Cancer Staging: Systematic Review and Meta-Analysis in Detection of Multifocal and Multicentric Cancer. *JCO* **2008**, *26* (19), 3248–3258. https://doi.org/10.1200/JCO.2007.15.2108.

(38) Solin, L. J.; Orel, S. G.; Hwang, W.-T.; Harris, E. E.; Schnall, M. D. Relationship of Breast Magnetic Resonance Imaging to Outcome After Breast-Conservation Treatment With Radiation for Women With Early-Stage Invasive Breast Carcinoma or Ductal Carcinoma in Situ. *JCO* **2008**, *26* (3), 386–391. https://doi.org/10.1200/JCO.2006.09.5448.

(39) Mittendorf, E. A.; Clifton, G. T.; Holmes, J. P.; Clive, K. S.; Patil, R.; Benavides, L. C.; Gates, J. D.; Sears, A. K.; Stojadinovic, A.; Ponniah, S.; Peoples, G. E. Clinical Trial Results of the HER-2/ *Neu* (E75) Vaccine to Prevent Breast Cancer Recurrence in High-Risk Patients: From US Military Cancer Institute Clinical Trials Group Study I-01 and I-02. *Cancer* **2012**, *118* (10), 2594–2602. https://doi.org/10.1002/cncr.26574.

(40) Silva, P.; Homer, J. J.; Slevin, N. J.; Musgrove, B. T.; Sloan, P.; Price, P.; West, C. M. L. Clinical and Biological Factors Affecting Response to Radiotherapy in Patients with Head and Neck Cancer: A Review: Radiotherapy Response in Head and Neck Cancer. *Clinical Otolaryngology* **2007**, *32* (5), 337–345. https://doi.org/10.1111/j.1749-4486.2007.01544.x.

(41) Barnett, G. C.; West, C. M. L.; Dunning, A. M.; Elliott, R. M.; Coles, C. E.; Pharoah, P. D. P.; Burnet, N. G. Normal Tissue Reactions to Radiotherapy:

Towards Tailoring Treatment Dose by Genotype. *Nature Reviews Cancer* **2009**, *9* (2), 134–142. https://doi.org/10.1038/nrc2587.

(42) Harder, S. J.; Isabelle, M.; DeVorkin, L.; Smazynski, J.; Beckham, W.; Brolo, A. G.; Lum, J. J.; Jirasek, A. Raman Spectroscopy Identifies Radiation Response in Human Non-Small Cell Lung Cancer Xenografts. *Scientific Reports* **2016**, *6* (1), 21006. https://doi.org/10.1038/srep21006.

(43) Harder, S. J.; Matthews, Q.; Isabelle, M.; Brolo, A. G.; Lum, J. J.; Jirasek, A. A Raman Spectroscopic Study of Cell Response to Clinical Doses of Ionizing Radiation. *Applied Spectroscopy* **2015**, *69* (2), 193–204. https://doi.org/10.1366/14-07561.

(44) Matthews, Q.; Brolo, A. G.; Lum, J.; Duan, X.; Jirasek, A. Raman Spectroscopy of Single Human Tumour Cells Exposed to Ionizing Radiation in Vitro. *Physics in Medicine and Biology* **2011**, *56* (1), 19–38. https://doi.org/10.1088/0031-9155/56/1/002.

(45) Matthews, Q.; Jirasek, A.; Lum, J. J.; Brolo, A. G. Biochemical Signatures of in Vitro Radiation Response in Human Lung, Breast and Prostate Tumour Cells Observed with Raman Spectroscopy. *Physics in Medicine and Biology* **2011**, *56* (21), 6839–6855. https://doi.org/10.1088/0031-9155/56/21/006.

(46) Matthews, Q.; Isabelle, M.; Harder, S. J.; Smazynski, J.; Beckham, W.; Brolo, A. G.; Jirasek, A.; Lum, J. J. Radiation-Induced Glycogen Accumulation Detected by Single Cell Raman Spectroscopy Is Associated with Radioresistance That Can Be Reversed by Metformin. *PLoS ONE* **2015**, *10* (8), 1–15. https://doi.org/10.1371/journal.pone.0135356.

(47) Matthews, Q.; Jirasek, A.; Lum, J. J.; Duan, X.; Brolo, A. G. Variability in Raman Spectra of Single Human Tumor Cells Cultured in Vitro: Correlation with Cell Cycle and Culture Confluency. *Applied Spectroscopy* **2010**, *64* (8), 871–887. https://doi.org/10.1366/000370210792080966.

(48) Sanli, T.; Rashid, A.; Liu, C.; Harding, S.; Bristow, R. G.; Cutz, J.-C.; Singh, G.; Wright, J.; Tsakiridis, T. Ionizing Radiation Activates AMP-Activated Kinase (AMPK): A Target for Radiosensitization of Human Cancer Cells. *Int. J. Radiation Oncology Biol. Phys.* **2010**, *78* (1), 221–229. https://doi.org/10.1016/j.ijrobp.2010.03.005.

(49) Jiang, X.; Perez-Torres, C. J.; Thotala, D.; Engelbach, J. A.; Yuan, L.; Cates, J.; Gao, F.; Drzymala, R. E.; Rich, K. M.; Schmidt, R. E.; Ackerman, J. J. H.; Hallahan, D. E.; Garbow, J. R. A GSK-3β Inhibitor Protects Against Radiation Necrosis in Mouse Brain. *Int. J. Radiation Oncology Biol. Phys.* **2014**, *89* (4), 714–721. https://doi.org/10.1016/j.ijrobp.2014.04.018.

(50) Storozhuk, Y.; Hopmans, S. N.; Sanli, T.; Barron, C.; Tsiani, E.; Cutz, J.-C.; Pond, G.; Wright, J.; Singh, G.; Tsakiridis, T. Metformin Inhibits Growth and Enhances Radiation Response of Non-Small Cell Lung Cancer (NSCLC) through ATM and AMPK. *Br J Cancer* **2013**, *108* (10), 2021–2032. https://doi.org/10.1038/bjc.2013.187.

(51) Meksiarun, P.; Aoki, P. H. B.; Van Nest, S. J.; Sobral-Filho, R. G.; Lum, J. J.; Brolo, A. G.; Jirasek, A. Breast Cancer Subtype Specific Biochemical Responses to Radiation. *The Analyst* **2018**, *143* (16), 3850–3858. https://doi.org/10.1039/C8AN00345A.

(52) Nieva, C.; Marro, M.; Santana-Codina, N.; Rao, S.; Petrov, D.; Sierra, A. The Lipid Phenotype of Breast Cancer Cells Characterized by Raman Microspectroscopy: Towards a Stratification of Malignancy. *PLoS ONE* **2012**, *7* (10), e46456. https://doi.org/10.1371/journal.pone.0046456.

(53) Picot, J.; Guerin, C. L.; Le Van Kim, C.; Boulanger, C. M. Flow Cytometry: Retrospective, Fundamentals and Recent Instrumentation. *Cytotechnology* **2012**, *64* (2), 109–130. https://doi.org/10.1007/s10616-011-9415-0.

(54) Kristensen, N.; Nymann, C.; Konradsen, H. Implementing Research Results in Clinical Practice- the Experiences of Healthcare Professionals. *BMC Health Serv Res* **2015**, *16* (1), 1–10. https://doi.org/10.1186/s12913-016-1292-y.

(55) Gohar, F.; Gohar, A.; Hülskamp, G.; Debus, O. The Translational Medicine Professional: A Bridge Between Bench and Bedside? *Frontiers in Medicine* **2018**, *5*, 294. https://doi.org/10.3389/fmed.2018.00294.

(56) Liberale, C.; Cojoc, G.; Bragheri, F.; Minzioni, P.; Perozziello, G.; La Rocca, R.; Ferrara, L.; Rajamanickam, V.; Di Fabrizio, E.; Cristiani, I. Integrated Microfluidic Device for Single-Cell Trapping and Spectroscopy. *Sci Rep* **2013**, *3* (1), 1258. https://doi.org/10.1038/srep01258.

(57) Redding, B.; Schwab, M.; Pan, Y. Raman Spectroscopy of Optically Trapped Single Biological Micro-Particles. *Sensors* **2015**, *15* (8), 19021–19046. https://doi.org/10.3390/s150819021.

(58) Casabella, S.; Scully, P.; Goddard, N.; Gardner, P. Automated Analysis of Single Cells Using Laser Tweezers Raman Spectroscopy. *Analyst* **2016**, *141* (2), 689–696. https://doi.org/10.1039/C5AN01851J.

(59) Yang, R.-J.; Fu, L.-M.; Hou, H.-H. Review and Perspectives on Microfluidic Flow Cytometers. *Sensors and Actuators B: Chemical* **2018**, *266*, 26–45. https://doi.org/10.1016/j.snb.2018.03.091.

(60) Search: Microfluidics, cells https://www.webofscience.com/wos/woscc/summary/c8b27464-a964-4570-a3ea-425a57de9add-1eefd8c7/relevance/1 (accessed 2022 -01 -15).

(61) Lau, A. Y.; Lee, L. P.; Chan, J. W. An Integrated Optofluidic Platform for Raman-Activated Cell Sorting. *Lab Chip* **2008**, *8* (7), 1116–1120. https://doi.org/10.1039/b803598a.

(62) Lankers, M.; Popp, J.; Kiefer, W. Raman and Fluorescence Spectra of Single Optically Trapped Microdroplets in Emulsions. *Appl Spectrosc* **1994**, *48* (9), 1166–1168. https://doi.org/10.1366/0003702944029569.

(63) Xie, C.; Dinno, M. A.; Li, Y. Near-Infrared Raman Spectroscopy of Single Optically Trapped Biological Cells. *Opt. Lett., OL* **2002**, *27* (4), 249–251. https://doi.org/10.1364/OL.27.000249.

(64) Jess, P. R. T.; Smith, D.; Mazilu, M.; Paterson, L.; Riches, A.; Herrington, S.; Sibbett, W.; Dholakia, K. Dual Beam Fibre Trap for Raman Micro-Spectroscopy of Single Cells. **2006**, *14* (12), 5779–5791.

(65) Lincoln, B.; Schinkinger, S.; Travis, K.; Wottawah, F.; Ebert, S. Reconfigurable Microfluidic Integration of a Dual-Beam Laser Trap with Biomedical Applications. **2007**, 703–710. https://doi.org/10.1007/s10544-007-9079-x.

(66) Dochow, S.; Krafft, C.; Neugebauer, U.; Popp, J. Tumour Cell Identification by Means of Raman Spectroscopy in Combination with Optical Traps and

Microfluidic Environments. *Lab Chip* **2011**, *11* (8), 1484–1490. https://doi.org/10.1039/c0lc00612b.

(67) Van Nest, S. J. Applications of Raman Spectroscopy in Radiation Oncology: Clinical Instrumentation and Radiation Response Signatures in Tissue. PhD thesis, University of Victoria, Victoria, 2018.

(68) Bae, S. C.; Lee, H.; Granick, S.; Lin, Z. Chemical Imaging in a Surface Forces Apparatus: Confocal Raman Spectroscopy of Confined Poly(Dimethylsiloxane). *Langmuir* **2005**, *21*, 5685–5688. https://doi.org/10.1021/la050233+.

(69) Drynda, A.; Seibt, J.; Hassel, T.; Bach, F. W.; Peuster, M. Biocompatibility of Fluoride-Coated Magnesium-Calcium Alloys with Optimized Degradation Kinetics in a Subcutaneous Mouse Model. *J. Biomed. Mater. Res.* **2013**, *101A* (1), 33–43. https://doi.org/10.1002/jbm.a.34300.

(70) van Midwoud, P. M.; Janse, A.; Merema, M. T.; Groothuis, G. M. M.; Verpoorte, E. Comparison of Biocompatibility and Adsorption Properties of Different Plastics for Advanced Microfluidic Cell and Tissue Culture Models. *Anal. Chem.* **2012**, *84* (9), 3938–3944. https://doi.org/10.1021/ac300771z.

(71) Vyawahare, S. Microfluidics Bootcamp 2015. *Microfluidics laboratory Princeton University* **2015**, *1*.

(72) Tang, S.; Whitesides, G. Basic Microfluidic and Soft Lithographic Techniques. *Optofluidics: Fundamentals, Devices, and Applications* **2010**, 7–32. https://doi.org/10.1002/1521-4095(200107)13:14<1053::AID-ADMA1053>3.0.CO;2-7.

(73) Gale, B.; Jafek, A.; Lambert, C.; Goenner, B.; Moghimifam, H.; Nze, U.; Kamarapu, S. A Review of Current Methods in Microfluidic Device Fabrication and Future Commercialization Prospects. *Inventions* **2018**, *3* (3), 60. https://doi.org/10.3390/inventions3030060.

(74) McDonald, J. C.; Duffy, D. C.; Anderson, J. R.; Chiu, D. T.; Wu, H.; Schueller, O. J. A.; Whitesides, G. M. Fabrication of Microfluidic Systems in Poly(Dimethylsiloxane). *Electrophoresis* **2000**, *21* (1), 27–40. https://doi.org/10.1002/(SICI)1522-2683(20000101)21:1<27::AID-ELPS27>3.0.CO;2-C.

(75) Wu, J.; Gu, M. Microfluidic Sensing: State of the Art Fabrication and Detection Techniques. *J. Biomed. Opt.* **2011**, *16* (8), 080901. https://doi.org/10.1117/1.3607430.

(76) van Heeren, H.; Hewkin, P. Design for Microfluidic Device Manufacture Guidelines, 2014.

(77) Rodrigues, R. O.; Lima, R.; Gomes, H. T.; Silva, A. M. T. Polymer Microfluidic Devices: An Overview of Fabrication Methods. *UPjeng* **2015**, *1* (1), 67–79. https://doi.org/10.24840/2183-6493_001.001_0007.

(78) Burns, M. A. An Integrated Nanoliter DNA Analysis Device. *Science* **1998**, *282* (5388), 484–487. https://doi.org/10.1126/science.282.5388.484.

(79) Tatry, M. C.; Laurichesse, E.; Perro, A.; Ravaine, V.; Schmitt, V. Kinetics of Spontaneous Microgels Adsorption and Stabilization of Emulsions Produced Using Microfluidics. *Journal of Colloid and Interface Science* **2019**, *548*, 1–11. https://doi.org/10.1016/j.jcis.2019.04.020.

(80) Bal, V.; Bandyopadhyaya, R. Mechanistic Aspects in the Formation of Nano- and Submicron Particles in a Batch and a Continuous Microfluidic Reactor: Experiment, Modeling and Simulation. *Chemical Engineering Journal* **2019**, *371*, 43–54. https://doi.org/10.1016/j.cej.2019.03.194.

(81) Halldorsson, S.; Lucumi, E.; Gómez-Sjöberg, R.; Fleming, R. M. T. Advantages and Challenges of Microfluidic Cell Culture in Polydimethylsiloxane Devices. *Biosensors and Bioelectronics* **2015**, *63*, 218–231. https://doi.org/10.1016/j.bios.2014.07.029.

(82) Wei-Cheng, T. *Microfluidics for Biological Applications*; Springer, 2008.

(83) Nghe, P.; Boulineau, S.; Gude, S.; Recouvreux, P.; van Zon, J. S.; Tans, S. J. Microfabricated Polyacrylamide Devices for the Controlled Culture of Growing Cells and Developing Organisms. *PLoS ONE* **2013**, *8* (9), 1–11. https://doi.org/10.1371/journal.pone.0075537.

(84) Berson, E. Development of a Microfluidic Platform for Cell Migration Studies along Gradients. Master of Science, Chalmers University of Technology, Gothenburg, Sweden, 2012.

(85) Shiang-Chi, Li. Single Channel Layer, Single Sheath-Flow Inlet Microfluidic Flow Cytometer with Three.Dimentional Hydrodynamic Focusing. *Lab on a Chip* **2012**, *12* (2012), 3135–3141. https://doi.org/10.1039/c2lc40246g.

(86) *Microfluidics and Microfabrication*; Chakraborty, S., Ed.; Springer: London, 2010. https://doi.org/10.1007/978-1-4419-1543-6.

(87) Pandey, C. M.; Augustine, S.; Kumar, S.; Kumar, S.; Nara, S.; Srivastava, S.; Malhotra, B. D. Microfluidics Based Point-of-Care Diagnostics. *Biotechnology Journal* **2018**, *13* (1), 1700047. https://doi.org/10.1002/biot.201700047.

(88) Chattopadhyay, P. K.; Roederer, M. Cytometry: Today's Technology and Tomorrow's Horizons. *Methods* **2012**, *57* (3), 251–258. https://doi.org/10.1016/j.ymeth.2012.02.009.

(89) Yi, C.; Li, C. W.; Ji, S.; Yang, M. Microfluidics Technology for Manipulation and Analysis of Biological Cells. *Analytica Chimica Acta* **2006**, *560* (1–2), 1–23. https://doi.org/10.1016/j.aca.2005.12.037.

(90) Zhou, Y.; Basu, S.; Wohlfahrt, K. J.; Lee, S. F.; Klenerman, D.; Laue, E. D.; Seshia, A. A. A Microfluidic Platform for Trapping, Releasing and Super-Resolution Imaging of Single Cells. *Sensors and Actuators, B: Chemical* **2016**, *232*, 680–691. https://doi.org/10.1016/j.snb.2016.03.131.

(91) Whulanza, Y.; Widyaratih, D. S.; Istiyanto, J.; Kiswanto, G. Realization and Testing of Lab-on-Chip for Human Lung Replication. *ARPN Journal of Engineering and Applied Sciences* **2014**, *9* (11), 2064–2067.

(92) Wang, F.; Burns, M. A. Performance of Nanoliter-Sized Droplet-Based Microfluidic PCR. *Biomed Microdevices* **2009**, *11* (5), 1071–1080. https://doi.org/10.1007/s10544-009-9324-6.

(93) Agresti, J. J.; Antipov, E.; Abate, A. R.; Ahn, K.; Rowat, A. C.; Baret, J.-C.; Marquez, M.; Klibanov, A. M.; Griffiths, A. D.; Weitz, D. A. Ultrahigh-Throughput Screening in Drop-Based Microfluidics for Directed Evolution. *Proceedings of the National Academy of Sciences* **2010**, *107* (9), 4004–4009.

(94) Gawad, S.; Schild, L.; Renaud, Ph. Micromachined Impedance Spectroscopy Flow Cytometer for Cell Analysis and Particle Sizing. *Lab on a Chip* **2001**, *1* (1), 76–82. https://doi.org/10.1039/b103933b.

(95) Caballero, D.; Kaushik, S.; Correlo, V. M.; Oliveira, J. M.; Reis, R. L.; Kundu, S. C. Organ-on-Chip Models of Cancer Metastasis for Future Personalized Medicine: From Chip to the Patient. *Biomaterials* **2017**, *149*, 98–115. https://doi.org/10.1016/j.biomaterials.2017.10.005.

(96) Fan, X.; Jia, C.; Yang, J.; Li, G.; Mao, H.; Jin, Q.; Zhao, J. A Microfluidic Chip Integrated with a High-Density PDMS-Based Microfiltration Membrane for Rapid Isolation and Detection of Circulating Tumor Cells. *Biosensors and Bioelectronics* **2015**, *71*, 380–386. https://doi.org/10.1016/j.bios.2015.04.080.

(97) Shaner, S. W.; Allen, J. K.; Felderman, M.; Pasko, E. T.; Wimer, C. D.; Cosford, N. D. P.; Kassegne, S.; Teriete, P. Design and Production of a Novel Microfluidic Device for the Capture and Isolation of Circulating Tumor Cell Clusters. *AIP Advances* **2019**, *9* (6), 065313. https://doi.org/10.1063/1.5084736.

(98) Psaltis, D.; Quake, S. R.; Yang, C. Developing Optofluidic Technology through the Fusion of Microfluidics and Optics. *Nature* **2006**, *442* (7101), 381–386. https://doi.org/10.1038/nature05060.

(99) Aebisher, D.; Bartusik, D.; Tabarkiewicz, J. Laser Flow Cytometry as a Tool for the Advancement of Clinical Medicine. *Biomedicine & Pharmacotherapy* **2017**, *85*, 434–443. https://doi.org/10.1016/j.biopha.2016.11.048.

(100) Vezenov, D. V.; Mayers, B. T.; Conroy, R. S.; Whitesides, G. M.; Snee, P. T.; Chan, Y.; Nocera, D. G.; Bawendi, M. G. A Low-Threshold, High-Efficiency Microfluidic Waveguide Laser. *J. Am. Chem. Soc.* **2005**, *127* (25), 8952–8953. https://doi.org/10.1021/ja0517421.

(101) Rossetto, N.; Fortunati, I.; Gellini, C.; Feis, A.; Ferrante, C. An Optofluidic Light Detector Based on the Photoacoustic Effect. *Sensors and Actuators B: Chemical* **2016**, *233*, 71–75. https://doi.org/10.1016/j.snb.2016.04.046.

(102) Alvankarian, J.; Majlis, B. Y. Tunable Microfluidic Devices for Hydrodynamic Fractionation of Cells and Beads: A Review. *Sensors (Switzerland)* **2015**, *15* (11), 29685–29701. https://doi.org/10.3390/s151129685.

(103) Liu, C.; Stakenborg, T.; Peeters, S.; Lagae, L. Cell Manipulation with Magnetic Particles toward Microfluidic Cytometry. *Journal of Applied Physics* **2009**, *105* (10), 102014. https://doi.org/10.1063/1.3116091.

(104) Yao, B.; Luo, G.; Feng, X.; Wang, W.; Chen, L.; Wang, Y. A Microfluidic Device Based on Gravity and Electric Force Driving for Flow Cytometry and Fluorescence Activated Cell Sorting. *Lab Chip* **2004**, *4* (6), 603–607. https://doi.org/10.1039/b408422e.

(105) Wang, M. M.; Tu, E.; Raymond, D. E.; Yang, J. M.; Zhang, H.; Hagen, N.; Dees, B.; Mercer, E. M.; Forster, A. H.; Kariv, I.; Marchand, P. J.; Butler, W. F. Microfluidic Sorting of Mammalian Cells by Optical Force Switching. *Nat Biotechnol* **2005**, *23* (1), 83–87. https://doi.org/10.1038/nbt1050.

(106) Xie, C.; Li, Y. Confocal Micro-Raman Spectroscopy of Single Biological Cells Using Optical Trapping and Shifted Excitation Difference Techniques. *Journal of Applied Physics* **2003**, *93* (5), 2982–2986. https://doi.org/10.1063/1.1542654.

(107) Zhang, H.; Liu, K.-K. Optical Tweezers for Single Cells. *Journal of The Royal Society Interface* **2008**, *5* (24), 671–690. https://doi.org/10.1098/rsif.2008.0052.

(108) Chrimes, A. F.; Khoshmanesh, K.; Stoddart, P. R.; Mitchell, A.; Kalantar-zadeh, K. Microfluidics and Raman Microscopy: Current Applications and Future Challenges. *Chem. Soc. Rev.* **2013**, *42* (13), 5880. https://doi.org/10.1039/c3cs35515b.

(109) Peric, O.; Hannebelle, M.; Adams, J. D.; Fantner, G. E. Microfluidic Bacterial Traps for Simultaneous Fluorescence and Atomic Force Microscopy. *Nano Res.* **2017**, *10* (11), 3896–3908. https://doi.org/10.1007/s12274-017-1604-5.

(110) Merkens, S.; Vakili, M.; Sánchez-Iglesias, A.; Litti, L.; Gao, Y.; Gwozdz, P. V.; Sharpnack, L.; Blick, R. H.; Liz-Marzán, L. M.; Grzelczak, M.; Trebbin, M. Time-Resolved Analysis of the Structural Dynamics of Assembling Gold Nanoparticles. *ACS Nano* **2019**, *13* (6), 6596–6604. https://doi.org/10.1021/acsnano.9b00575.

(111) Wang, N.; Tan, F.; Zhao, Y.; Tsoi, C. C.; Fan, X.; Yu, W.; Zhang, X. Optofluidic UV-Vis Spectrophotometer for Online Monitoring of Photocatalytic Reactions. *Sci Rep* **2016**, *6* (1), 1–8. https://doi.org/10.1038/srep28928.

(112) Ebrahimifard, R.; van den Driesche, S.; Breiteneder, H.; Hafner, C.; Vellekoop, M. J. An Infrared Sensor System for the Analysis and Differentiation of Living Mammalian Cells Using D2O Based Microfluidics. *Sensors and Actuators B: Chemical* **2017**, *247*, 981–991. https://doi.org/10.1016/j.snb.2017.03.057.

(113) Ebrahimifard, R.; van den Driesche, S.; Di Salvo, M.; Vellekoop, M. J. Discrimination of Living Biological Cells by Infrared Absorbance Measurements in a Microfluidics Chip. *Procedia Engineering* **2016**, *168*, 1471–1474. https://doi.org/10.1016/j.proeng.2016.11.424.

(114) Inci, F.; Ozen, M. O.; Saylan, Y.; Miansari, M.; Cimen, D.; Dhara, R.; Chinnasamy, T.; Yuksekkaya, M.; Filippini, C.; Kumar, D. K.; Calamak, S.; Yesil, Y.; Durmus, N. G.; Duncan, G.; Klevan, L.; Demirci, U. A Novel On-Chip Method for Differential Extraction of Sperm in Forensic Cases. *Adv. Sci.* **2018**, *5* (9), 1800121. https://doi.org/10.1002/advs.201800121.

(115) Foquet, M.; Korlach, J.; Zipfel, W.; Webb, W. W.; Craighead, H. G. DNA Fragment Sizing by Single Molecule Detection in Submicrometer-Sized Closed Fluidic Channels. *Anal. Chem.* **2002**, *74* (6), 1415–1422. https://doi.org/10.1021/ac011076w.

(116) Harrison, J. P.; Berry, D. Vibrational Spectroscopy for Imaging Single Microbial Cells in Complex Biological Samples. *Front. Microbiol.* **2017**, *8*, 675. https://doi.org/10.3389/fmicb.2017.00675.

(117) Mazutis, L.; Gilbert, J.; Ung, W. L.; Weitz, D. A.; Griffiths, A. D.; Heyman, J. A. Single-Cell Analysis and Sorting Using Droplet-Based Microfluidics. *Nat Protoc* **2013**, *8* (5), 870–891. https://doi.org/10.1038/nprot.2013.046.

(118) Ashkin, A. Acceleration and Trapping of Particles by Radiation Pressure. *Phys. Rev. Lett.* **1970**, *24* (4), 156–159. https://doi.org/10.1103/PhysRevLett.24.156.

(119) The Nobel Prize in Physics 2018 https://www.nobelprize.org/prizes/physics/2018/ashkin/facts/ (accessed 2021 -08 -13).

(120) Ashkin, A.; Dziedzic, J. M. Optical Levitation by Radiation Pressure. *Appl. Phys. Lett.* **1971**, *19* (8), 283–285. https://doi.org/10.1063/1.1653919.

(121) Ashkin, A. Forces of a Single-Beam Gradient Laser Trap on a Dielectric Sphere in the Ray Optics Regime. *Biophysical Journal* **1992**, *61* (2), 569–582. https://doi.org/10.1016/S0006-3495(92)81860-X.

(122) Chu, S.; Bjorkholm, J. E.; Ashkin, A.; Cable, A. Experimental Observation of Optically Trapped Atoms. *Phys. Rev. Lett.* **1986**, *57* (3), 314–317. https://doi.org/10.1103/PhysRevLett.57.314.

(123) Ashkin, A. A.; Dziedzic, J. M. Optical Trapping and Manipulation of Viruses and Bacteria. *American Association for the Advancement of Science* **1987**, *235* (4795), 1517–1520. https://doi.org/10.3102/0162373712440039.

(124) Ashkin, A.; Dziedzic, J. M.; Yamane, T. Optical Trapping and Manipulation of Single Cells Using Infrared Laser Beams. *Nature* **1987**, *330* (6150), 769–771. https://doi.org/10.1038/330769a0.

(125) Constable, A.; Kim, J.; Mervis, J.; Zarinetchi, F.; Prentiss, M. Demonstration of a Fiber-Optical Light-Force Trap. *Opt. Lett., OL* **1993**, *18* (21), 1867–1869. https://doi.org/10.1364/OL.18.001867.

(126) Lyons, E. R.; Sonek, G. J. Confinement and Bistability in a Tapered Hemispherically Lensed Optical Fiber Trap. *Appl. Phys. Lett.* **1995**, *66* (13), 1584–1586. https://doi.org/10.1063/1.113859.

(127) Sidick, E.; Collins, S. D.; Knoesen, A. Trapping Forces in a Multiple-Beam Fiber-Optic Trap. *Appl. Opt., AO* **1997**, *36* (25), 6423–6433. https://doi.org/10.1364/AO.36.006423.

(128) Guck, J.; Ananthakrishnan, R.; Moon, T. J.; Cunningham, C. C.; Käs, J. Optical Deformability of Soft Biological Dielectrics. *Physical Review Letters* **2000**, *84* (23), 5451–5454. https://doi.org/10.1103/PhysRevLett.84.5451.

(129) Guck, J.; Schinkinger, S.; Lincoln, B.; Wottawah, F.; Ebert, S.; Romeyke, M.; Lenz, D.; Erickson, H. M.; Ananthakrishnan, R.; Mitchell, D.; Käs, J.; Ulvick, S.; Bilby, C. Optical Deformability as an Inherent Cell Marker for Testing Malignant Transformation and Metastatic Competence. *Biophysical Journal* **2005**, *88* (5), 3689–3698. https://doi.org/10.1529/biophysj.104.045476.

(130) Ashkin, A. Optical Trapping and Manipulation of Neutral Particles Using Lasers. *Proceedings of the National Academy of Sciences* **1997**, *94* (10), 4853–4860. https://doi.org/10.1364/OPN.10.5.000041.

(131) Fällman, E.; Axner, O. Design for Fully Steerable Dual-Trap Optical Tweezers. *Appl. Opt.* **1997**, *36* (10), 2107–2113. https://doi.org/10.1364/AO.36.002107.

(132) Leitz, G.; Fällman, E.; Tuck, S.; Axner, O. Stress Response in Caenorhabditis Elegans Caused by Optical Tweezers: Wavelength, Power, and Time Dependence. *Biophysical Journal* **2002**, *82* (4), 2224–2231. https://doi.org/10.1016/S0006-3495(02)75568-9.

(133) Pilát, Z.; Ježek, J.; Šerý, M.; Trtílek, M.; Nedbal, L.; Zemánek, P. Optical Trapping of Microalgae at 735–1064nm: Photodamage Assessment. *Journal of Photochemistry and Photobiology B: Biology* **2013**, *121*, 27–31. https://doi.org/10.1016/j.jphotobiol.2013.02.006.

(134) Ramser, K.; Enger, J.; Goksör, M.; Hanstorp, D.; Logg, K.; Käll, M. A Microfluidic System Enabling Raman Measurements of the Oxygenation Cycle

in Single Optically Trapped Red Blood Cells. *Lab Chip* **2005**, *5* (4), 431–436. https://doi.org/10.1039/B416749J.

(135) Galbraith, D. Flow Cytometry and Cell Sorting: The next Generation. *Methods* **2012**, *57* (3), 249–250. https://doi.org/10.1016/j.ymeth.2012.08.010.

(136) Bonner, W. A.; Hulett, H. R.; Sweet, R. G. Fluorescence Activated Cell Sorting. *Review of Scientific Instruments* **1972**, *43* (3), 404–409. https://doi.org/10.1063/1.1685647.

(137) Tung, Y. PDMS-Based Opto-Fluidic Micro Flow Cytometer with Two-Color, Multi-Angle Fluorescence Detection Capability Using PIN Photodiodes. *Sensors and Actuators B: Chemical* **2004**, *98* (2–3), 356–367. https://doi.org/10.1016/j.snb.2003.10.010.

(138) Tsutsui, H.; Ho, C.-M. Cell Separation by Non-Inertial Force Fields in Microfluidic Systems. *Mechanics Research Communications* **2009**, *36* (1), 92–103. https://doi.org/10.1016/j.mechrescom.2008.08.006.

(139) Singh, R. C. V. Raman and the Discovery of the Raman Effect. *Phys. perspect.* **2002**, *4* (4), 399–420. https://doi.org/1422–6944/02/040399–22.

(140) Linic, S.; Christopher, P.; Ingram, D. B. Plasmonic-Metal Nanostructures for Efficient Conversion of Solar to Chemical Energy. *Nature Mater* **2011**, *10* (12), 911–921. https://doi.org/10.1038/nmat3151.

(141) Tonndorf, P.; Schmidt, R.; Dai, R.; Böttger, P.; Zhang, X.; Börner, J.; Khloc, C.; Gordan, O.; R.T. Zahn, D.; de Vasconcellos, S. M.; Bratschitsch, R. Photoluminescence Emission and Raman Response of Monolayer MoS2, MoSe2, and WSe2. *OSA* **2013**, *21* (4), 4908–4916. https://doi.org/10.1364/OE.21.004908.

(142) Xia, F.; Wang, H.; Jia, Y. Rediscovering Black Phosphorus as an Anisotropic Layered Material for Optoelectronics and Electronics. *Nat Commun* **2014**, *5* (1), 1–6. https://doi.org/10.1038/ncomms5458.

(143) Yang, D.; Velamakanni, A.; Bozoklu, G.; Park, S.; Stoller, M.; Piner, R. D.; Stankovich, S.; Jung, I.; Field, D. A.; Ventrice, C. A.; Ruoff, R. S. Chemical Analysis of Graphene Oxide Films after Heat and Chemical Treatments by X-Ray Photoelectron and Micro-Raman Spectroscopy. *Carbon* **2009**, *47* (1), 145–152. https://doi.org/10.1016/j.carbon.2008.09.045.

(144) Coleman, J. N.; Khan, U.; Blau, W. J.; Gun'ko, Y. K. Small but Strong: A Review of the Mechanical Properties of Carbon Nanotube–Polymer Composites. *Carbon* **2006**, *44* (9), 1624–1652. https://doi.org/10.1016/j.carbon.2006.02.038.

(145) Sharma, V. K.; Yngard, R. A.; Lin, Y. Silver Nanoparticles: Green Synthesis and Their Antimicrobial Activities. *Advances in Colloid and Interface Science* **2009**, *145* (1–2), 83–96. https://doi.org/10.1016/j.cis.2008.09.002.

(146) Dreaden, E. C.; Alkilany, A. M.; Huang, X.; Murphy, C. J.; El-Sayed, M. A. The Golden Age: Gold Nanoparticles for Biomedicine. *Chem. Soc. Rev.* **2012**, *41* (7), 2740–2779. https://doi.org/10.1039/C1CS15237H.

(147) Sdobnov, A. Y.; Tuchin, V. V.; Lademann, J.; Darvin, M. E. Confocal Raman Microscopy Supported by Optical Clearing Treatment of the Skin—Influence on Collagen Hydration. *J. Phys. D: Appl. Phys.* **2017**, *50* (28), 285401. https://doi.org/10.1088/1361-6463/aa77c9.

(148) Yu, Q.; Jauregui, L. A.; Wu, W.; Colby, R.; Tian, J.; Su, Z.; Cao, H.; Liu, Z.; Pandey, D.; Wei, D.; Chung, T. F.; Peng, P.; Guisinger, N. P.; Stach, E. A.; Bao, J.; Pei, S.-S.; Chen, Y. P. Control and Characterization of Individual Grains and Grain Boundaries in Graphene Grown by Chemical Vapour Deposition. *Nature Mater* **2011**, *10* (6), 443–449. https://doi.org/10.1038/nmat3010.

(149) Liu, Z.; Tabakman, S.; Welsher, K.; Dai, H. Carbon Nanotubes in Biology and Medicine: In Vitro and in Vivo Detection, Imaging and Drug Delivery. *Nano Res.* **2009**, *2* (2), 85–120. https://doi.org/10.1007/s12274-009-9009-8.

(150) Steuwe, C.; Patel, I. I.; Ul-Hasan, M.; Schreiner, A.; Boren, J.; Brindle, K. M.; Reichelt, S.; Mahajan, S. CARS Based Label-Free Assay for Assessment of Drugs by Monitoring Lipid Droplets in Tumour Cells: CARS Based Label-Free Assay for Assessment of Drugs. *J. Biophoton.* **2014**, *7* (11–12), 906–913. https://doi.org/10.1002/jbio.201300110.

(151) Notingher, I.; Jell, G.; Notingher, P. L.; Bisson, I.; Tsigkou, O.; Polak, J. M.; Stevens, M. M.; Hench, L. L. Multivariate Analysis of Raman Spectra for in Vitro Non-Invasive Studies of Living Cells. *Journal of Molecular Structure* **2005**, *744–747*, 179–185. https://doi.org/10.1016/j.molstruc.2004.12.046.

(152) Nikolaeva, G. Y.; Sagitova, E. A.; Prokhorov, K. A.; Pashinin, P. P.; Nedorezova, P. M.; Klyamkina, A. N.; Guseva, M. A.; Gerasin, V. A. Using Raman Spectroscopy to Determine the Structure of Copolymers and Polymer Blends. *J. Phys.: Conf. Ser.* **2017**, *826* (1), 012002. https://doi.org/10.1088/1742-6596/826/1/012002.

(153) Ricci, M.; Ragonese, F.; Gironi, B.; Paolantoni, M.; Morresi, A.; Latterini, L.; Fioretti, B.; Sassi, P. Glioblastoma Single-Cell MicroRaman Analysis under Stress Treatments. *Sci Rep* **2018**, *8* (1), 1–10. https://doi.org/10.1038/s41598-018-26356-x.

(154) den Hartigh, L. J.; Connolly-Rohrbach, J. E.; Fore, S.; Huser, T. R.; Rutledge, J. C. Fatty Acids from Very Low-Density Lipoprotein Lipolysis Products Induce Lipid Droplet Accumulation in Human Monocytes. *The Journal of Immunology* **2010**, *184* (7), 3927–3936. https://doi.org/10.4049/jimmunol.0903475.

(155) Andrews, D. L.; Allcock, P. *Photonics, Volume 4: Biomedical Photonics, Spectroscopy, and Microscopy*, 1st ed.; John Wiley & Sons: New York, 2015; Vol. 4.

(156) Banday, S.; Wàňi, M. F. Nanomechanical and Nanotribological Characterization of Multilayer Self-lubricating Ti/MoS_2/Si/MoS_2 Nanocoating on Aluminium-silicon Substrate. *Surf Interface Anal* **2019**, *51* (6), 649–660. https://doi.org/10.1002/sia.6631.

(157) Gupta, R.; Bastani, B.; Goddard, N. J.; Grieve, B. Absorption Spectroscopy in Microfluidic Flow Cells Using a Metal Clad Leaky Waveguide Device with a Porous Gel Waveguide Layer. *Analyst* **2013**, *138* (1), 307–314. https://doi.org/10.1039/C2AN35898K.

(158) Magnesium Fluoride (MgF_2) Optical Material https://www.crystran.co.uk/optical-materials/magnesium-fluoride-mgf2 (accessed 2021 -11 -29).

(159) Lake, M. A.; Zartman, J. J.; Hoelzle, D. J. Microfluidic Device Design, Fabrication, and Testing Protocols. *Protocol Exchange* **2015**, 1–26. https://doi.org/10.1038/protex.2015.069.

(160) Liang, X. J.; Liu, A. Q.; Zhang, X. M.; Yap, P. H.; Ayi, T. C.; Yoon, H. S. Determination of Refractive Index for Single Living Cell Using Integrated Biochip. In *The 13th International Conference on Solid-State Sensors, Actuators and Microsystems, 2005. Digest of Technical Papers. TRANSDUCERS '05.*; IEEE: Seoul, Korea, 2005; Vol. 2, pp 1712–1715. https://doi.org/10.1109/SENSOR.2005.1497421.

(161) Rehman, S.; Movasaghi, Z.; Tucker, A. T.; Joel, S. P.; Darr, J. A.; Ruban, A. V.; Rehman, I. U. Raman Spectroscopic Analysis of Breast Cancer Tissues: Identifying Differences between Normal, Invasive Ductal Carcinoma and Ductal Carcinomain Situ of the Breast Tissue. *J. Raman Spectrosc.* **2007**, *38* (10), 1345–1351. https://doi.org/10.1002/jrs.1774.

(162) Chowdary, M. V. P.; Kumar, K. K.; Kurien, J.; Mathew, S.; Krishna, C. M. Discrimination of Normal, Benign, and Malignant Breast Tissues by Raman Spectroscopy. *Biopolymers* **2006**, *83* (5), 556–569. https://doi.org/10.1002/bip.20586.

(163) Liu, C.-H.; Zhou, Y.; Sun, Y.; Li, J. Y.; Zhou, L. X.; Boydston-White, S.; Masilamani, V.; Zhu, K.; Pu, Y.; Alfano, R. R. Resonance Raman and Raman Spectroscopy for Breast Cancer Detection. *Technol Cancer Res Treat* **2013**, *12* (4), 371–382. https://doi.org/10.7785/tcrt.2012.500325.

(164) Krafft, C.; Knetschke, T.; Siegner, A.; Funk, R. H. W.; Salzer, R. Mapping of Single Cells by near Infrared Raman Microspectroscopy. *Vibrational Spectroscopy* **2003**, *32* (1), 75–83. https://doi.org/10.1016/S0924-2031(03)00049-3.

(165) Hernandez-Rueda, J.; Clarijs, J.; van Oosten, D.; Krol, D. M. The Influence of Femtosecond Laser Wavelength on Waveguide Fabrication inside Fused Silica. *Appl. Phys. Lett.* **2017**, *110* (16), 161109. https://doi.org/10.1063/1.4981124.

(166) Cui, L.; Butler, H. J.; Martin-Hirsch, P. L.; Martin, F. L. Aluminium Foil as a Potential Substrate for ATR-FTIR, Transflection FTIR or Raman Spectrochemical Analysis of Biological Specimens. *Anal. Methods* **2016**, *8* (3), 481–487. https://doi.org/10.1039/C5AY02638E.

(167) Lazaro-Pacheco, D.; Shaaban, A. M.; Rehman, S.; Rehman, I. Raman Spectroscopy of Breast Cancer. *Applied Spectroscopy Reviews* **2020**, *55* (6), 439–475. https://doi.org/10.1080/05704928.2019.1601105.

(168) by the Office of the CTO. MKS Instruments Handbook: Principles and Applications in Photonics Technologies, 2019.

(169) Neumann, E.-G. Physical Explanation of Waveguiding by Single-Mode Fibers. In *Single-Mode Fibers: Fundamentals*; Neumann, E.-G., Ed.; Springer Berlin Heidelberg: Berlin, Heidelberg, 1988; pp 9–16. https://doi.org/10.1007/978-3-540-48173-7_2.

(170) Siegman, A. E. *Lasers*; University Science Books, 1986.